Technical Report

TR-04-03

Inspection of copper canisters for spent nuclear fuel by means of ultrasound

NDE of friction stir welds, nonlinear acoustics, ultrasonic imaging

Tadeusz Stepinski (editor), Fredrik Lingvall,
Erik Wennerström, Ping Wu
Uppsala University, Signals and Systems,
Department of Materials Science

January 2004

Svensk Kärnbränslehantering AB
Swedish Nuclear Fuel
and Waste Management Co
Box 5864
SE-102 40 Stockholm Sweden
Tel 08-459 84 00
+46 8 459 84 00
Fax 08-661 57 19
+46 8 661 57 19

Inspection of copper canisters for spent nuclear fuel by means of ultrasound

NDE of friction stir welds, nonlinear acoustics, ultrasonic imaging

Tadeusz Stepinski (editor), Fredrik Lingvall,
Erik Wennerström, Ping Wu
Uppsala University, Signals and Systems,
Department of Materials Science

January 2004

Abstract

This report contains results concerning advanced ultrasound for the inspection of copper canisters for spent nuclear fuel obtained at Signals and Systems, Uppsala University in years 2002/2003.

After a short introduction a review of the NDE techniques that have been applied to the assessment of friction stir welds (FSW) is presented. The review is based on the results reported by the specialists from the USA, mostly from the aerospace industry.

A separate chapter is devoted to the extended experimental and theoretical research concerning potential of nonlinear waves in NDE applications. Further studies concerning nonlinear propagation of acoustic and elastic waves (classical nonlinearity) are reported. Also a preliminary investigation of the nonlinear ultrasonic detection of contacts and interfaces (non-classical nonlinearity) is included. Report on the continuation of previous work concerning computer simulation of nonlinear propagations of ultrasonic beams in water and in immersed solids is also presented.

Finally, results of an investigation concerning a new method of synthetic aperture imaging (SAI) and its comparison to the traditional phased array (PA) imaging and to the synthetic aperture focusing technique (SAFT) are presented. A new spatial-temporal filtering method is presented that is a generalization of the previously proposed filter. Spatial resolution of the proposed method is investigated and compared experimentally to that of classical SAFT and PA imaging. Performance of the proposed method for flat targets is also investigated.

Contents

Chapter 1

Introduction

1.1 Outline of the Report

Reliable detecting and sizing natural defects in EB and friction stir welds that will be used for sealing copper canisters for spent nuclear fuel requires applying advanced ultrasonic imaging techniques. In this report we are presenting our recent results concerning inspection of copper canisters for spent nuclear fuel by means of ultrasound.

Our research activity in this project in year 2002/2003 consisted of three separate main tasks:

- NDE of friction stir welds
- Nonlinear acoustics, and
- Synthetic aperture imaging

The first task, presented in Chapter 2 is an review of the NDE techniques that have been applied to the assessment of friction stir welds (FSW). It includes also a preliminary evaluation of their feasibility for copper canister inspection. The review is based on the results reported by the specialists from the USA working mostly with aerospace applications.

The second task that is a continuation of our experimental and theoretical research concerning the potential of nonlinear waves in NDE applications is reported in Chapter 3. Further studies concerning nonlinear propagation of acoustic and elastic waves (classical nonlinearity) are presented. It includes also a preliminary investigation of nonlinear ultrasonic detection of contacts and interfaces (non-classical nonlinearity). This phenomenon could be applied for the detection of lack of fusion defects that are difficult to find using the classical NDE techniques, for instance, kissing bonds in friction stir welds. Report on the continuation of previous work concerning computer simulation of nonlinear propagations of ultrasonic beams in water and in immersed solids is also presented in this chapter.

The third task is concerned mainly with an investigation of a new method of synthetic aperture imaging (SAI) and its comparison to the traditional phased array (PA) imaging and to the synthetic aperture focusing technique (SAFT). This task is reported in two chapters, Chapter 4 and Chapter 5. A new spatial-temporal filtering method is presented that is a generalization of the previously proposed filter and can be used in a general array imaging case. Spatial resolution of the proposed method is investigated and compared experimentally to that of classical SAFT and PA imaging. Performance of the proposed method for flat targets is also investigated.

The fourth task planned for this period, *Signal processing toolbox* has been completed and a MATLAB® Toolbox containing practical implementation of signal processing algorithms for the needs of SKB's Canister Laboratory in Oskarshamn has been delivered in spring 2003.

Chapter 2

NDE of Friction Stir Welds

by Tadeusz Stepinski

2.1 Introduction

Friction Stir Welding, a process invented and patented by TWI, is a significant advancement in metal welding technology that can produce stronger, lighter, and more efficient welds than any previous process. Friction Stir Welding is currently being used to produce components in the Delta family of rockets, as well as in shipbuilding, rail car manufacturing, construction, and other related industries.

Friction stir welding (FSW) is using pin tools rotating at several hundred RPM and traversing a square butt joint of the same design configuration as that used for fusion welding. A welding tool moves along the area to be joined while rotating at a high speed. A well controlled load is applied by a FSW machine through a spindle on a pin tool. The action between the tool and the metal creates frictional heat, which softens the metal but does not melt it. The plasticized material is then, in essence, consolidated to create one piece of metal where there were originally two. Consolidation of the weldment occurs via an extruding/forging action under the pin tool shoulder as the pin tool is traversed along the length of the weld. The weld is left in a fine-grained, hot worked condition with no entrapped oxides or gas porosity.

The FSW is an surprisingly robust and forgiving process, as far as the tool pin positioning does not fail, especially considering the weld quality it produces [1].

2.2 Flaws occurring in FSW

FSW offers several major benefits over traditional fusion welding processes, including the complete elimination of solidification defects, filler materials, shielding gases and weld distortion. Since traditional heating methods are not employed, the properties of the metal in the joined area are higher than those from any other known welding process and distortion is virtually eliminated.

However, FSW, which is a completely new weld process imposes entirely new inspection requirements for NDE techniques. Although it is known to be free from most fusion weld process defects the increased demands of reliability and safety in the fields where it is applied require proof testing as well as full NDE.

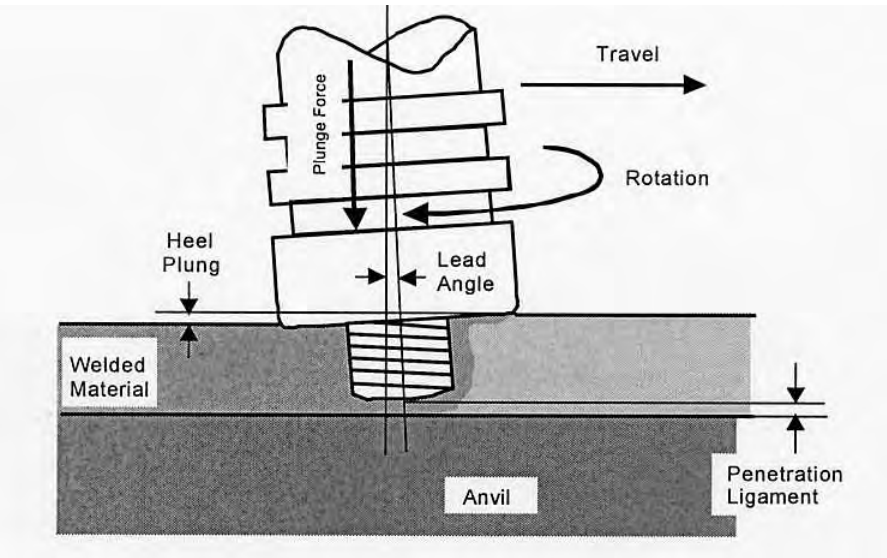

Figure 2.1: Schematic of the FSW process.

Due to the nature of the consolidation process during FSW (cf. Figure 2.1) flaws in principle may occur at any orientation and any angle but in practice the axial and transverse defects seem to be most common. Many types of defects have been observed during in the friction stir welds

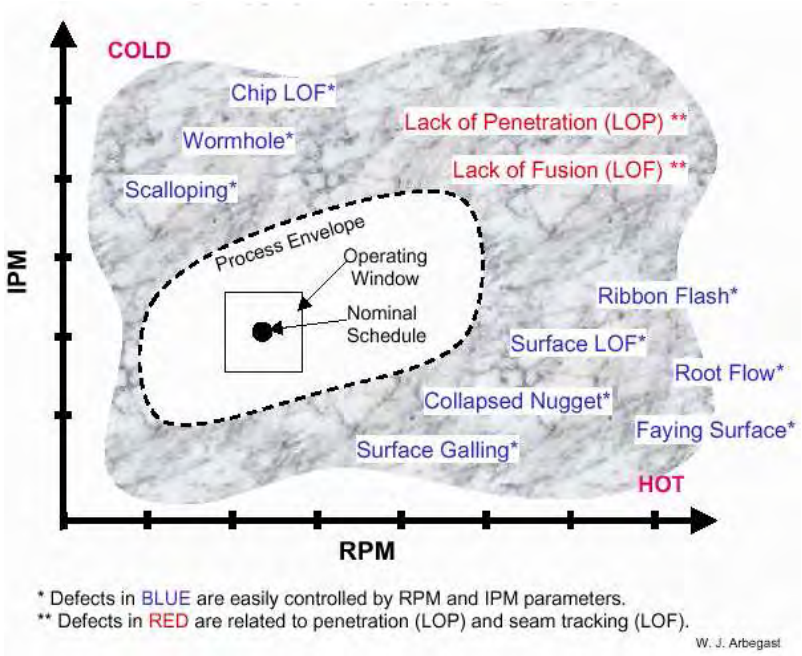

Figure 2.2: Defects occurring in FSW depending on the main process variables (courtesy of W.J. Arbegast).

depending on the process conditions ([2], [3]). Arbegast and coworkers show the correlation between the defect type and two fundamental process variables:

- tool rotation, and
- tool longitudinal speed

Depending on the combination of these two parameters a "cold" or "hot" state in the weld is observed and different types of flaws are likely to occur, see Figure 2.2.

One of the FSW process' main, though very rare, defects is *lack of (or incomplete) penetration* (LOP). LOP is encountered when either plunge depth or material flow in the swirl zone is insufficient beneath the FSW pin (see Figure 2.3a). Due of the extreme load from mechanical welding, the LOP gap literally collapses on itself and laps together, especially when the length of the flaw is more that 0.1 mm.

Kissing bond is a very special type of LOP defect that is very tightly closed, so that it is hard to detect with any NDE method, especially when located deep in the weld.

Primary factors affecting LOP during welding include heat input or material flow and, most importantly, the depth of the FSW pin tool. Figure 2.1 illustrates the FSW process and the associated metallurgical features. The latter include the total depth of LOP, the depth of plastically deformed material, and the tight bond at the LOP interface. The most significant of these with regard to NDE is the degree of "tightness" of the "kissing bond" created at the LOP interface.

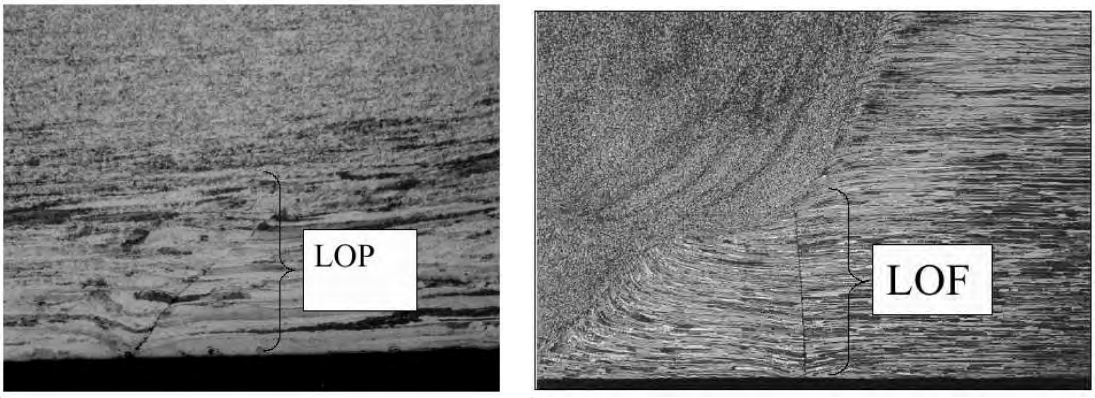

(a) (b)

Figure 2.3: Metallurgical cross section of FSW with (a) LOP and (b) LOF defects (courtesy of W.J. Arbegast).

Similar type of defect is *lack of fusion* (LOF), which is caused by an offset from the centerline condition where the joint is missed (see Figure 2.3b).

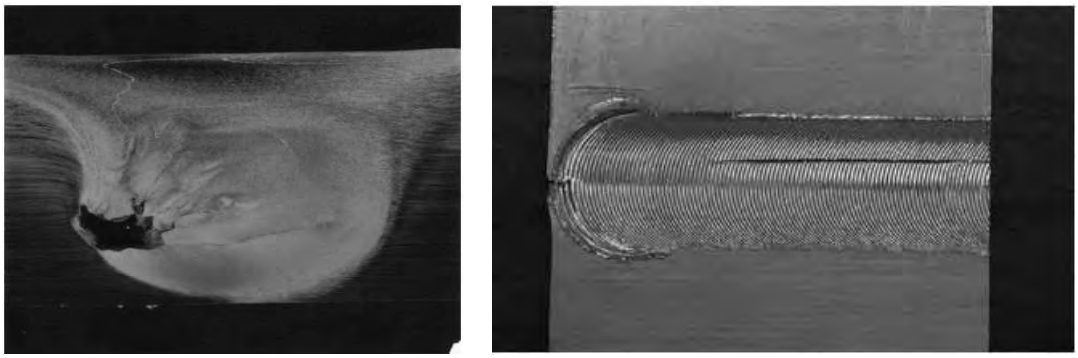

(a) (b)

Figure 2.4: Worm hole (a) and surface lap (b) in FSW (courtesy of W.J. Arbegast).

Worm holes that result form "cold" process parameters show up occasionally near the surface (see Figure 2.4a).

Surface laps result from "hot" conditions when RPM is too high (see Figure 2.4b).

2.3 NDE techniques feasible for FSW inspection

FSW which is relatively new weld process brings new inspection requirements for both visual and NDE techniques. Although most fusion weld process defects are not encountered in FSW, the safety demands in its advanced applications require thorough inspection using both classical and new NDE techniques. The discontinuities observed during FSW development present a challenge requiring a blend of several complementary NDE methods to provide adequate inspection.

Existing NDE methods, such as, radiographic and penetrant inspection will be certainly used for FSW inspection; however, those methods will be supplemented by new, automated NDE.

For each particular application appropriate NDE techniques have to be selected and qualified based on the respective procedures and documentation, process validation, and the requirements of fracture control. Factors that have to be taken into account in evaluating NDE techniques should include critical initial discontinuity size, potential discontinuities detected by a given method, the capability of candidate NDE techniques, and their maturity for production use.

Below we present a review including a wide variety of NDE methods, such as, visual, several liquid penetrant techniques, ultrasonic, radiography, and eddy current.

The review is based on the experience gained at Lockheed Martin Michoud Space Systems in FSW of AL2125, a light-weight, high-strength, aluminum-copper-lithium (Al-Cu-Li) alloy (see [4] for details).

2.3.1 Visual Inspection

Visual inspection, which is the most straightforward and simplest inspection technique can be used for inspecting for surface features including excess flash, shoulder voids, and even weld misalignment. These defects are visible to the naked eye and are assigned to improper welding parameters, such as, excessive travel speed (mm /min), excessive rotational speed (RPM), inadequate plunge force loads, and improper joint tracking.

As mentioned above the principal unacceptable root side condition is LOP that has been commonly considered as the most critical type of defect. Visual examination combined with etching can be used for this purpose. Etching is a chemical treatment performed after welding most often to prepare mechanically worked surfaces prior to penetrant inspection. Kinchen [4] reports that visual examination of the root side of the weld performed after etching operation was capable of detecting LOP discontinuities.

In this case, after the etching process the weld nugget dynamically recrystallized zone (DX) and its surrounding heat-affected zone (HAZ) are clearly pronounced, making the lack of FSW nugget a distinct feature visible to the trained eye. The reason for the successful detection rate is that it is easy to discern the DXZ from the surrounding base metal and HAZ after etching. Therefore, visual inspection may be a feasible technique to confirm suspected LOP conditions. Figure 2.5 shows a 3X magnification view of an LOP defect on the root side of a FSW after etching.

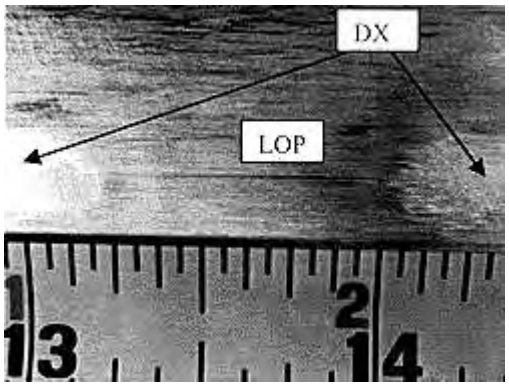

Figure 2.5: LOP in FSW visible after etching of root side.

However, the metallurgical characteristics of an LOP discontinuity that are directly linked to the weld process parameters directly determine the ability of NDE techniques to detect LOP.

Conventional NDE techniques rely heavily on a physical separation – void or air gap – as the means to provide a response from such a defect. The less significant this separation, the more problematic its detection.

2.3.2 Penetrant Inspection

Kinchen reports [4] that penetrant inspection carried out on FSW test panels in the etched condition performed consistently and successfully and was capable of detecting surface breaking root-side LOP discontinuities.

Penetrant inspection of the FSW test panels in the as-welded condition was found to be an unacceptable method due to poor detection and the excessive background noise produced by the surface, which interfered with the inspection.

However, due to different sensitivity of detection for each penetrant solution, the results were dissimilar and depended on the penetrant type. Additionally, double etching, using caustic etchant solution prior to the application of penetrant, enhanced the detection of LOP in comparison to single etching. Test results demonstrated etching that removed a minimum of 0.0004 in. of metal prior to the application of penetrant improved the detectability of LOP.

2.3.3 Ultrasonic Inspection

NDE engineers and technicians from RD/Tech, Automated Inspection Systems, Lockheed Martin, Aerospatiale Matra CCR, and Marshall Space Flight Center (MSFC) performed extensive ultrasonic inspection (UT) on FSW test panels (cf. [3], [4], [5]).

Conventional ultrasonic transducers and multi-element phased arrays were evaluated, generating both L- and S-waves. The results initially revealed the technique(s) that could detect LOP discontinuities at 15 to 20% of the material thickness or greater.

It appeared, however, that the improvement of FSW tooling directly affected metallurgical characteristics of the LOP discontinuity resulting in more tightly closed and thus more difficult to detect discontinuity. Ultimately, certain improvements to RD/Tech's phased-array UT inspection technique resulted in the ability to detect LOP of 25 to 30% of thickness and greater.

The use of phased array enables multiple angled views of the friction stir weld at one time, substantially increasing the likelihood of detecting defects with various orientations.

2.3.4 Radiographic Inspection

Radiographic inspection performed at Lockheed Martin using film and digital methods on FSW test panels demonstrated 90% probability/95%confidence ability to detect LOP discontinuities greater than or equal to 30% of the material thickness [4].

However, serious problems were encountered in the film radiography of dissimilar alloy welds; results showed a limited detectability of LOP discontinuity. The main reason for that was varying chemical composition of copper and lithium in the weldment. Such problems are not likely to occur in the FSW welds performed in homogenous copper.

2.3.5 Eddy Current Inspection

Kinchen [4] reports results of the conventional eddy current (EC) inspection performed at Lockheed Martin on FSW test panels by means of a 1-MHz pencil probe and a 300-kHz differential rotating probe. Initial eddy current results demonstrated reliable detection by both Marshall

Space Flight Center and Lockheed Martin techniques for Al2195/Al2195 friction stir welds containing at least 0.065 in., or deeper, LOP.

However, the extreme difference in EC signals observed across FSW welds in dissimilar-alloy that yielded a significant EC response from virtually all panels, made the discrimination of LOP versus no LOP panels unreliable. Although such problems are unlikely for FSWs in copper the EC inspection has to be performed from the root side, which is not accessible in copper canisters.

2.3.6 Exotic NDE techniques

JENTEK MWM®-Arrays

JENTEK Sensors Inc. developed a new type of eddy current sensor known as meandering winding magnetometers (MWM) and MWM arrays. The MWMs are characterized by simple meandering geometry so, that the magnetic field distribution created by the primary winding and the resulting response of sensing elements can be accurately modelled (see Figure 2.6).

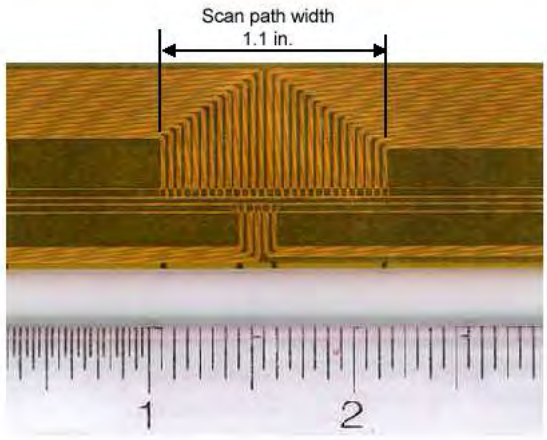

Figure 2.6: Detail view of MWM-Array sensor.

The accurate model of the MWM sensor and its interaction with the test materials enables conversion of the sensor response into the electric and geometrical parameters of the inspected material in various test set-ups. These forward models calculated both for single and multiple layered media have been used by JENTEK Sensors Inc. to create databases of the sensor responses for the range of properties of interest. The databases stored in the measurement system PC real-time mapping of the measured signals into physical properties of interest [6]. The MWM system consists of a PC or laptop computer, Gridstation database, instrumentation module, and MWM probe and sensors.

JENTEK Sensors, Inc. has worked with Lockheed Martin and NASA since 1998 to adapt their technology for ET FSW inspection [7]. JENTEK Sensors Inc. has designed and demonstrated a custom sensor and inspection technique capable of detecting 0.75 mm LOP in A1295 FSW, and respectively, 1.25 mm and deeper LOP in dissimilar FSWs (8.13 mm thick Al2195-to-Al2195 and Al2219-to-Al2195).

The MWM-Array provides the capability to measure absolute electrical conductivity of the material. The electrical conductivity measured on the root side of the panels with FSWs varies across the weld due to microstructural differences introduced by the FSW process. An example of conductivity image (C-scan) obtained from the scanned data acquired on FSW sample with

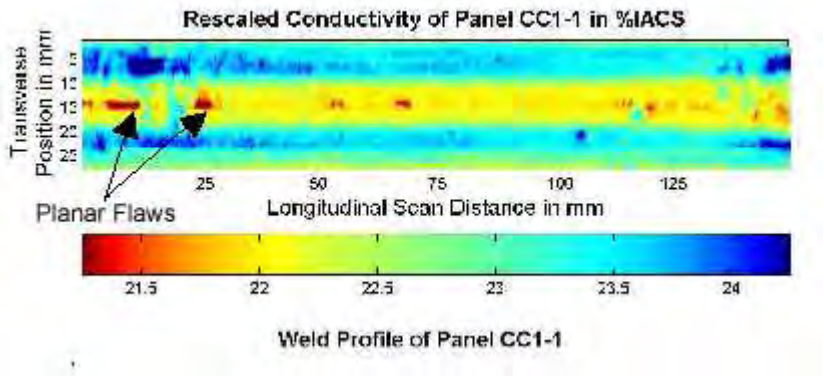

Figure 2.7: C-scan of a FSW weld sensed by the MWM sensor from the root side. Arrows indicate LOP defects.

1.14mm LOP is shown in Figure 2.7.

It has to be noted, however, that due to the limited penetration of the eddy currents detecting LOP using MWM sensors is possible only from the root side.

Nonlinear vibrometry

Classical vibrometry (known also as resonance spectroscopy) that has been used in NDE for many years relies on the measurement of the *linear* mechanical transfer function of a vibrating system. This assumption concerns both the material properties and the geometry. A defect in a component changes its mechanical transfer function, so that it can be detected by comparing the spectra acquired respectively before and after damaging the component. Major disadvantage of this technique is that a nominal spectrum of the specific component has to be known a priori to detect the flowed one.

For many types of defects the assumption of linear behavior under finite mechanical amplitudes may not hold as they may be strongly nonlinear. The nonlinear effects due to a sharp defect may be considerably higher than the intrinsic non-linearity of the bulk material. For sharp defects in metals, damages increase the number of internal boundaries that can behave differently depending on the direction of load:

- Under perpendicular load the stress/strain-diagram is no more symmetrical: The interface can open under tensile stress, thereby reducing the stiffness, while it behaves like bulk material under compression.
- Under tangential load they can rub against each other loosing energy due to friction

The first effect can be detected by the nonlinear vibrometry while the second one using ultrasound lock-in thermography, which will be presented in the next Section.

In the nonlinear vibrometry proposed by G. Busse from University of Stuttgart, [8] a high power source generates sinusoidal wave into the inspected sample and resulting local spectra are measured on the surface by using a scanning laser vibrometer (see Figure 2.9).

Nonlinear vibrometry has been tested on different materials and it was capable of detecting delaminations in fiber reinforced plastic and ceramics, corrosion in aluminum as well as cracks in steel [9]. Example spectra obtained from the delamination in glass fiber reinforced plastic are shown in Figure 2.9.

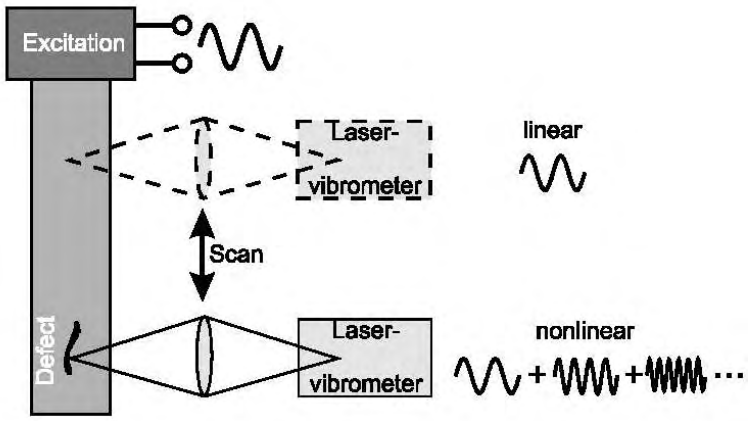

Figure 2.8: Principle of nonlinear vibrometry: an ultrasound excitation generates nonlinear waves in the sample that are sensed by the at the surface by a laser vibrometer (courtesy of G. Busse).

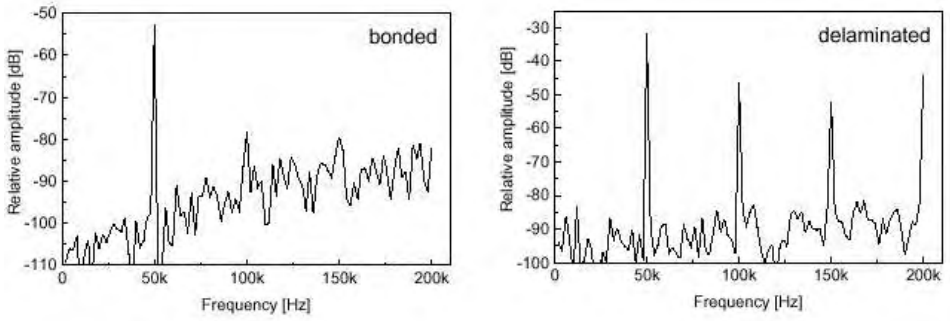

Figure 2.9: Spectra obtained for a delaminated glass fiber reinforced plastic (courtesy of G. Busse).

Although direct application of nonlinear vibrometry for the inspection of FSW has not been reported yet this technique has a certain potential of detecting LOP in FSW.

Ultrasound lock-in thermography

In classical lock-in thermography a coded heat flow is analyzed in relation to the temperature modulation that is induced by a periodical heat deposition: Absorption of modulated optical radiation results in a temperature modulation that propagates as a thermal wave into the inspected material. As the thermal wave is reflected at the boundaries of subsurface features, its superposition to the original thermal wave causes a signal change that depends on the depth of the hidden boundary.

Vibrothermography is a new method capable of visualizing stress concentrations deep in the material. In vibrothermography modulated mechanical load induces temperature changes due to the thermoelastic effect [10]. At higher frequencies, the efficiency of heating is improved. Therefore, the injection of amplitude modulated ultrasound as a source of load provides an efficient periodical heating which makes the defect a thermal wave transmitter acting at the low modulating frequency [11].

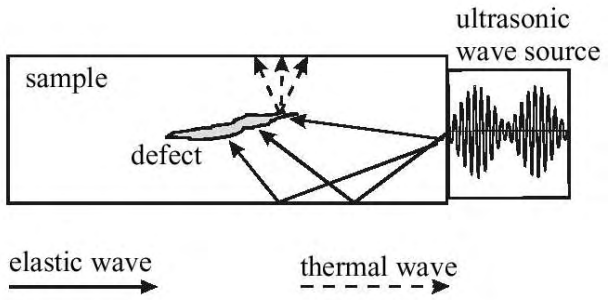

Figure 2.10: ULT principle: Modulated ultrasound excitation generates thermal waves in the defect itself, that are sensed at the surface (courtesy of G. Busse).

In ultrasound lock-in thermography (ULT), a high power ultrasonic transducer clamped to a tested sample generates modulated elastic waves into the sample. The elastic waves propagate until they diminish due to convertion into heat, mostly in the high-loss-angle areas of defects. In this way the defects reveal themselves by the internally generated and emitted thermal waves. These waves are phase sensitively monitored when thay arrive at the sample surface, see Figure 2.10. In this way the defects can be easily detected since only a very low heat is generated in the intact areas of the inspected component. As the phase difference between the modulation and the thermal wave is proportional to the depth where the defect is located, local depth information is obtained.

The setup for the experiment performed by the group of Prof. G. Busse from University of Stuttgart, [11] is displayed in Figure 2.11. The carrier frequency of the elastic waves in this experiment was about 20 kHz while the frequency of amplitude modulation was typically between 0.03 and 0.23 Hz.

Using ultrasound lock-in thermography (at 20 kHz carrier frequency, transducer clamped to inspected component) the locally enhanced loss angle due to friction effects and stress concentration in defects could be monitored [11]. In ductile materials such as steel, only the crack tips are under mechanical load to produce heat due to friction and the crack tips appear as

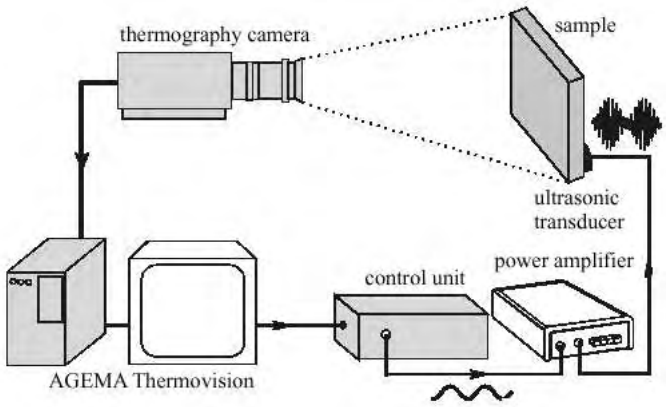

Figure 2.11: Experimental setup for ultrasound lock-in thermography (courtesy of G. Busse).

bright spots in the thermographic amplitude image. The other parts of the crack do not heat up (see [11] for details).

Although a direct application of ULT for detecting LOP in FSW has not been reported yet this technique seems to be have some potential for NDE of FSW.

2.4 Conclusions

A short review of the NDE methods suitable for the inspection of FSW was presented, based on the reported applications mostly in the aerospace industry.

Existing NDE methods, including liquid penetrant, radiography, and phased array ultrasonics have a capacity to detect some defects observed in the FSW.

The LOP defects that seem to the most dangerous and difficult to detect type of discontinuity can be detected in many cases by dye-penetrant testing using double-edge etching or JENTEK MWM®-Arrays applied from the root side.

Nonlinear vibrometry, able to detect delaminations, plastic deformations, porosity and cracks in any orientation in many different materials seems to be an interesting candidate method for detecting LOP in FSW.

Even Ultrasound lock-in thermography may have some potential in the NDE of FSW.

Bibliography

[1] T. Morrison (publisher). Taking off with friction stir welding. *Fabricating & Metalworking, F& M Magazine*, September 2002. Cygnus Business Media, `http://www.ndx.com/industry_news.asp?action=details&article_id=392`.

[2] W.J. Arbegast, E.R. Coletta, and Z. Li. Characterization of friction stir weld defect types. In *TMS 2001 Annual Meeting*, New Orleans, LA, 2001.

[3] A. Lamarre and M. Moles. Ultrasound phased array inspection technology for the evaluation of friction stir welds. In *Proc of the 15th World Conference on Nondestructive Testing*, Roma (Italy), 15–21 October 2000.

[4] D.G. Kinchen and E. Aldahir. NDE of friction stir welds in aerospace applications. *Inspection Trends*, January 2002.

[5] G. Ithurralde, D. Simonet, J. Choffy, and L. Bernard. NDT approach and multi-sensors tools for the inspection of aeronautic welds. In *Proc. of the 15th World Conference on Nondestructive Testing, 2000*, Roma (Italy), 15–21 October 2000.

[6] N.J. Goldfine. Magnetometers for improved materials characterization in aerospace applications. *Materials Evaluation*, 51(3):396–405, March 1993.

[7] N. Goldfine, D. Grundy, and V. Zilberstein. Friction stir weld inspection through conductivity imaging using shaped field MWM–arrays. In *Proc. of the 6th International ASM Trends in Welding Conference*, Callaway Gardens, Pine Mountain, GA, 2003. ASM.

[8] N.Krohn and G. Busse. Nonlinear vibrometry for damage detection. In *Proc. of the 7th International Congress on Sound an Vibration*, volume II, pages 589–596, Garmisch-Patenkirchen, 4–7 July 2000.

[9] N.Krohn, R.Stel, and G. Busse. Nonlinear vibrometry for quality assurance. In *Proc. of the 27th Review of Progress in Quantitative Nondestructive Evaluation (QNDE)*, Ames, Iowa, 16–21 July 2000.

[10] W.Rippel, M.Bauerand, and G.Busse. Lockin vibrothermal inspection of polymer composites. In *Proc. of the Quantitative Infrared Thermography, QIRT 92*, pages 154–159, Paris, 1992. Paris: Editions Europennes Thermique et Industrie.

[11] Th. Zweschper, A. Dillenz, and G. Busse. Ultrasound lock-in thermography - a defect selective NDT method for the inspection of aerospace components. *Insight*, 43:173–179, 2001.

Chapter 3

Nonlinear Acoustics

by Ping Wu

3.1 Introduction

A fast growing interest in the application of nonlinear ultrasonics to nondestructive evaluation (NDE) has been demonstrated in recent years at the international conferences on ultrasonics, nonlinear acoustics and NDE, as well as in international journals devoted to ultrasonics and acoustics like *IEEE UFFC, JASA, Ultrasonics, etc.* An extensive research on nonlinear ultrasonics in materials characterization and defects detection has been conducted including both fundamental and application aspects.

The latest results of this research has been presented in two recent international ultrasonics conferences, *Ultrasonics International'03* (UI'03 in Granada, Spain) and *the 5th World Congress on Ultrasonics* (WCU) in Paris), where special sessions have been organized devoted to nonlinear ultrasonics and its applications in NDE, namely:

"Nonlinear ultrasonics in materials characterization" in UI'03 [1], and

"Nonlinear Ultrasonics of Cracks, Contacts and Interfaces" in WCU [2].

A number of papers presented in these sessions were dedicated to nonlinear ultrasonic detection of cracks, contacts and interfaces [3–11] and a few papers were focused on classical nonlinear ultrasonics (e.g., evaluating nonlinear parameters in solids and third-order elastic constants) [12–16].

Nonlinear ultrasonics and acoustics deal with a broad range of nonlinear phenomena of mechanical vibrations and wave propagation in fluids and solids. The nonlinearities in these phenomena may be classified into two categories: classical and non-classical ones.

The classic nonlinearity in solids has been studied for more than half a century [17–22]. It is related to the the anharmonicity and imperfection of atomic lattices (so called intrinsic physical nonlinearity), and characterized by a distributed property, so that the nonlinear distortion of waves accumulates as they propagate. This type of nonlinearity defined by the third- or higher-order elastic constants, or nonlinearity parameters, is often very small. However, the nonlinearity parameter will be changed when, for instance, a distribution of micro-cracks appears inside material. This feature has recently found new application in the characterization of fatigue and degraded materials [23–26].

Among the non-classical nonlinearity is the nonlinearity resulting from cracks, contacts and interfaces, which show non-symmetric elasticity when ultrasound waves interact with them. The non-symmetric elasticity results in highly nonlinear elastic response to ultrasound waves. This is so-called contact acoustic nonlinearity (CAN) that is often characteristic of local property [27–33].

Recent publications have shown that use of nonlinear waves has extended the potential of existing ultrasonic NDE techniques making possible the detection of defects that are invisible for a linear ultrasound.

Our interest in nonlinear ultrasonics and acoustics started in 2000, from an experimental study of material harmonic imaging of copper canisters with the aim to evaluate the electron-beam (EB) welds in the canisters [34, 35]. Then we have carried out extensive experimental and theoretical studies of nonlinear propagation of ultrasonic waves and tried to apply them to evaluate the copper canister and the EB welds [36, 37]. The nonlinearity that we dealt with in the past three years belongs to the classical category.

In addition to further studies concerning nonlinear propagation of acoustic and elastic waves (classical nonlinearity), recently, we have conducted a preliminary investigation of nonlinear ultrasonic detection of contacts and interfaces (non-classical nonlinearity), in order to detect possible defects, e.g., kissing bonds, in friction stir welds.

The research progress and the results on nonlinear ultrasonics are reported in this chapter

and organized in three parts:

- fundamentals of nonlinear ultrasonics in NDE,
- nonlinear propagation of ultrasonic beams,
- nonlinear ultrasonic detection of contacts and interfaces.

In the first part some fundamentals of nonlinear ultrasonics related to the project are presented in an attempt to interpret the results in the second and the third part, and to obtain a guidance to our nonlinear investigation.

Acoustic radiation and initial acoustic intensity from a transducer is the first issue discussed in this part because they have a direct impact on the nonlinear evolution of ultrasound (harmonics) and on the nonlinear excitation of contacted cracks and interfaces. This discussion should help us to answer the questions type: why should a high frequency transducer (e.g., 5 MHz) be used for the classical nonlinearity whereas a low frequency transducer (e.g., 500 kHz) for the nonclassical nonlinearity, for example, CAN?

Then, the nonlinear propagation and harmonics generation, and the factors, such as, initial acoustic intensity and frequency associated with transducers, nonlinearity parameter, sound velocity, acoustical impedance and attenuation that are related to the propagating media are investigated based on the plane wave case. This can help us to find answers to questions like: why is the level of harmonics generated in copper much lower than that in water?

The second part of this chapter reports the continuation of previous work concerning computer simulation of nonlinear propagations of ultrasonic beams in water and in immersed solids. The work has been extended by additional experiments and computer simulations.

The program that was developed before and enabled simulating nonlinear propagation of ultrasonic beams in water and in immersed solids (without taking into account the harmonics generated in water) now has been extended. The extended program can be used to calculate the total harmonics generated in immersed metal blocks. The simulated harmonics include those generated in water (and transmitted into the immersed solid) as well as those generated in the solid. Thus, a useful tool has been developed that enables a quantitative analysis of the impact of the harmonics generated in water on the total amount of harmonics in the immersed material.

The research result in this part is also helpful in the interpretation of the measurement results presented in the third part dealing with CAN, e.g., to distinguish the harmonics originating from the classical nonlinearity from those due to the nonclassical nonlinearity.

The third part of this chapter includes mainly experiments concerned with CAN and nonlinear ultrasonic detection. The experimental setup for contact measurements has been built, and different sets of copper samples bonded in different ways have been inspected. Many measurements have been made. This research has been finished at a preliminary stage. The theory related to this research has also been investigated based on the recent publications [27–33].

3.2 Fundamentals of nonlinear ultrasonics in NDE

In this section a fundamental study of nonlinear ultrasonics in NDE is conducted that is related to our current research on ultrasonic nonlinear propagation and crack detection.

Nonlinear ultrasonics is concerned with radiation and propagation of finite-amplitude (especially high-power) ultrasound, and its interaction with discontinuities (e.g., cracks, interfaces, voids, etc). Nonlinear propagation of ultrasound is applied for material harmonic imaging, and for nonlinear ultrasonic detection of cracks the nonlinear vibrations of cracks, resulting from the

interaction with high-power ultrasound is used. Ultrasonic transducers used in these two cases are driven by high voltage, but the respective requirements are different. For harmonic imaging one uses high frequency excitations (serval MHz or so in NDE) to achieve faster harmonics growth, whereas for nonlinear detection of contacts a large particle displacement is desired that is able to excite the contacting sides of cracks.

To this purpose, the acoustic radiation from a transducer and initial acoustic intensity are first defined. The nonlinear propagation of ultrasound is then studied using the plane wave case using the Burgers equation that was also implemented previously [36, 37]. Factors that effect nonlinear propagation and harmonics generation are analyzed and discussed.

Wave propagation process resulting from mechanical vibrations generated by a transducer is the fundamental issue discussed in acoustics and ultrasonics. The vibration and propagation processes can be linear or nonlinear, and to describe the processes the following parameters are used:

- particle displacement $\mathbf{u}$ in m, and particle velocity $\mathbf{v} = d\mathbf{u}/dt$ in m/s;
- acoustic pressure p (in fluids)/stress τ (in solids) in Pa;
- sound velocity (or speed) c in m/s, and density ρ in kg/m^3, and attenuation α in Np/m (1 Np = 8.686 dB);
- acoustic intensity I in W/cm^2: in a fluid $I = \langle pv \rangle_t$ (temporal averaging) or in a solid $I = \langle \tau v \rangle_t$, and acoustic power $P_a = AI$ in W, where A is the area on which the acoustic intensity is I;
- acoustic impedance $Z = p/v$ in rayl (= Pa·s/m), and for a plane wave $Z = \rho c$

3.2.1 Acoustic radiation and initial acoustic intensity

Consider a planar transducer that generates a mechanical vibration on its surfaces with a frequency f_0 (or angular frequency $\omega_0 = 2\pi f_0$). The vibration in terms of particle displacement can be expressed as

$$u_0(t) = U_0 sin(\omega_0 t) \tag{3.1}$$

or in terms of particle velocity as

$$v_0(t) = V_0 sin(\omega_0 t) \tag{3.2}$$

where U_0 and V_0 are the amplitudes of particle displacement and particle velocity, respectively. Note that the displacement and velocity used here are in one-dimension so that they are written in scalar form. Supposing that the planar transducer has a radiating area A and is attached to a medium with sound speed c and density ρ, the acoustic power radiated by the transducer is $P_a = AV_0^2\rho c/2$ and correspondingly an initial acoustic intensity is

$$I_0 = \frac{V_0^2}{2}\rho c \tag{3.3}$$

For given I_0, the initial particle velocity can be written as

$$V_0 = \sqrt{\frac{2I_0}{\rho c}} = \sqrt{\frac{2I_0}{Z}} \tag{3.4}$$

which shows that *for a given initial acoustic intensity the larger the acoustic impedance the smaller the initial particle velocity.* For example, in water the sound speed and the density are c_w=1484 m/s and ρ_w=1000 kg/m^3, respectively, and in a copper material c_c=4596 m/s and

ρ_c=8960 kg/m^3, respectively. Accordingly, the acoustic impedances in water and copper are Z_w=1.484 and Z_c=41.180 M Rayleigh, respectively. Significant difference in acoustic impedances results in a large difference in initial particle velocity in water and copper.

For example, for I_0=1.5 W/cm^2, the initial particle velocity in water is V_{0w} = 0.1422 m/s, whereas in copper material V_{0c} = 0.0270 m/s; for I_0=4 W/cm^2, V_{0w}=0.2322 m/s in water, whereas in copper material V_{0c}=0.0441 m/s.

This demonstrates that for a given initial acoustic intensity (or a given radiation power) the initial velocity amplitude is much smaller in copper than in water, specifically, only approx. 19% of that in water, which follows from

$$V_{0c} = \sqrt{Z_w/Z_c} = 0.1898 V_{0w} \tag{3.5}$$

As we can see below, since V_{0c} is much smaller than V_{0w} for a given radiation power, the nonlinearity of propagating waves in copper grows much slower than in water.

Since $\mathbf{v} = d\mathbf{u}/dt$, then

$$V_0 = \omega_0 U_0, \text{ or } U_0 = V_0/\omega_0 \tag{3.6}$$

which shows that for a fixed velocity amplitude V_0 the particle displacement U_0 is directly proportional to the frequency ω_0; a lower frequency yields a larger displacement. In the above presented example, in which the initial particle velocity in a copper material for I_0=4 W/cm^2 is V_{0c}=0.0441 m/s, the corresponding particle displacement is U_{0c}=14.0 nm for 0.5 kHz and 2.8 nm for 2.5 MHz, both of which are about $1.5{\cdot}10^{-6}$ of the longitudinal wave length. In nonlinear ultrasonic detection of cracks, contacts and interfaces, the large particle displacement is required to get contact nonlinearity.

3.2.2 Nonlinear propagation and harmonics generation

Assume that a continuous plane wave (with frequency ω_0) in terms of particle velocity $v(t, z)$ propagates in the z-direction in a medium with sound speed c, density ρ, and acoustic attenuation $\alpha(\omega_0)$ (which is frequency dependent).

Under the assumption that the plane wave is small in amplitude (or the acoustic power radiated from the transducer is small), the propagation can be described in a linear relation as follows

$$v(t, z) = V_0 e^{-\alpha(\omega_0)z} sin[\omega_0(t - z/c)] = V(z) sin[\omega_0(t - z/c)] \tag{3.7}$$

In this case, the plane wave propagating at any position z always has one frequency ω_0.

When a high power ultrasound is used the amplitude of ultrasonic wave is not any longer small, then the wave propagation should be described in a nonlinear relation, e.g., Burgers equation in terms of particle velocity as follows

$$\begin{aligned} V_n(z + \Delta z) = &\left[V_n(z) - \alpha_0 (n f_0)^b V_n(z) \Delta z\right] \\ &+ j\frac{\beta\omega_0}{2c^2}\left[\sum_{m=1}^{n-1} m V_m(z) V_{n-m}(z) + \sum_{m=n+1}^{\infty} n V_m(z) V^*_{m-n}(z)\right]\Delta z \end{aligned} \tag{3.8}$$

The above equation shows an nth harmonic at distance $z + \Delta z$, $V_n(z + \Delta z)$, which is evolved from the propagation of $V_n(z)$ over an elementary interval Δz.

$V_n(z+\Delta z)$ is made up of a linear part (in the first square brackets on the right hand side of the equation) and a nonlinear part (in the second square brackets). The linear part consists of the velocity value of at z and the attenuated part over propagation distance Δz; and the nonlinear term is composed of the accretion of the nth harmonic due to the preceding harmonics (the first

term in the 2nd square brackets, the sum of the first to (n-1)th harmonics), and the depletion due to higher harmonics (the second term, the sum of the (n+1) th to ∞th harmonics) over the incremented distance Δz. In Eq. (3.8) α_0 is the attenuation coefficient in Np/m/MHz^b, where b, for example, is 2 for water and 1.3 for human tissue [38]. The nonlinearity parameter in fluids is related to B/A in a form of $\beta = 1 + B/2A$ where B/A is the ratio of the second-order nonlinear coefficient to the linear coefficient in Taylor series expansion of the equation of state $P = P(\rho)$ in fluid. The coefficient of the nonlinear part,

$$\beta\omega_0/(2c^2) \tag{3.9}$$

is directly proportional to the nonlinearity parameter β and the fundamental frequency ω_0, and inversely proportional to the squared sound speed c^2. The nonlinear part vanishes when β=0. At the initial position z=0 (just on the transducer), only the fundamental exists and its amplitude is equal to the initial particle velocity (i.e., $V_1(0) = V_0$) and all the higher harmonics are zero (i.e., $V_1(0) = 0$ for $n > 1$) because of $z = 0$ and $\Delta z = 0$. When the fundamental propagates its energy will flow to higher harmonics, and the rate of the energy flow depends on the initial velocity value (or initial acoustic intensity), as will be illustrate below. In the linear part we can see that the attenuation α may impact the n th harmonic from z to $z + \Delta z$. Here we are going to study how these parameters (β, α, I_0, ω_0 and ρc) affect the nonlinear propagation of a plane wave as well as the initial acoustic intensity, based on the Burgers equation 3.8.

Since the nonlinear propagation of a wave exhibit the generation of harmonics, the growth of harmonics is used to analyze the nonlinear behavior. Note that in all the calculations the step size used is $\Delta z = 0.5$ mm, and the number of harmonics used is 21.

A. Impact of the nonlinear parameter β

When a plane wave propagates in media having different nonlinear parameter β the nonlinearity (harmonics) growths will be different. This is shown in the calculations in Figure 3.1, which are made by assuming that a plane wave with $I_0 = 10.0$ W/cm^2 (corresponding to V_0=0.3284 m/s)and $f_0 = 5$ MHz propagates in a medium (water) having $c = 1484$ m/s, $\rho = 1000$ kg/m^3, α_0= 0.025 NP/m/MHz^2, and $b = 2$.

Note that only the first to fifth of the 21 harmonics are shown in the figure and in the following four figures as well.

Comparing the cases for different β's in Figure 3.1 we can see that the larger the β, the faster the fundamental decreases and the faster the higher harmonics grow (because the energy of the fundamental flows to the higher harmonics).

B. Impact of the attenuation

Ultrasonic attenuation in a medium results in the decrease of all harmonics that grow as they propagate. The higher order (frequency) the harmonic the more it attenuates. The influence of the attenuation on the nonlinear behavior of wave propagation is presented in Figure 3.2 in which the results are calculated for a plane wave with $I_0 = 10.0$ W/cm^2 and $f_0 = 5$ MHz propagating in a medium (water) having $c = 1484$ m/s, $\rho = 1000$ kg/m^3, b = 2, but β= 3.6 (or B/A=5.2).

The results show that the larger the attenuation coefficient α_0, the more the harmonics attenuate (especially at a larger propagation distance) and the larger the influence it has on the higher harmonics.

C. Impact of the initial acoustic intensity

A larger initial acoustic intensity I_0 corresponds to a faster initial particle velocity. The impact that I_0 has on the harmonics growth is shown in Figure 3.3, for a plane wave with f_0

= 5 MHz but different initial acoustic intensities propagating in a medium (water) having c = 1484 m/s, ρ = 1000 kg/m^3, b = 2, but β= 3.6 (or B/A=5.2).

The results in Figure 3.3 show that the larger the I_0, the larger the initial velocity amplitude and the faster the higher harmonics grow.

D. Impact of the frequency

The influence of the fundamental frequency f_0 on the nonlinear propagation can be easily seen from Eq. 3.9. A higher f_0 yields a larger value of the coefficient of the nonlinear part, and thus leads to a faster harmonics growth.

For a plane wave with = 10.0 W/cm^2 but different fundamental frequencies propagates in a medium (water) having c = 1484 m/s, ρ = 1000 kg/m^3, b = 2, but β= 3.6 (or B/A=5.2), the results for different f_0's are shown in Figure 3.4. The figure shows that the larger the f_0, the faster the higher harmonics grow up. This is similar to the impact of β.

E. Harmonics growths in water and copper

For a given initial acoustic intensity, a plane wave in copper (with c_c = 4596 m/s and ρ_c = 8960 kg/m^3) has a smaller initial particle velocity than in water (with c_w = 1484 m/s and ρ_w = 1000 kg/m^3). The coefficient $\beta\omega_0/(2c^2)$ of the nonlinear part in Eq. 3.8 in copper, meanwhile, is smaller than in water. Thus, the nonlinearity accumulation (harmonics growth) in copper will be much smaller than in water. This is illustrated in Figure 3.5 for a plane wave with I_0 = 10.0 W/cm^2 and f_0 = 5 MHz and a nonlinearity parameter of β=4.54 in copper and β=3.6 in water.

The results presented in Figure 3.5 agree with the above analysis, i.e., the higher harmonics in copper grow up much slower than in water. This conclusion is useful in explaining nonlinear behavior of ultrasonic beams propagating in immersed copper.

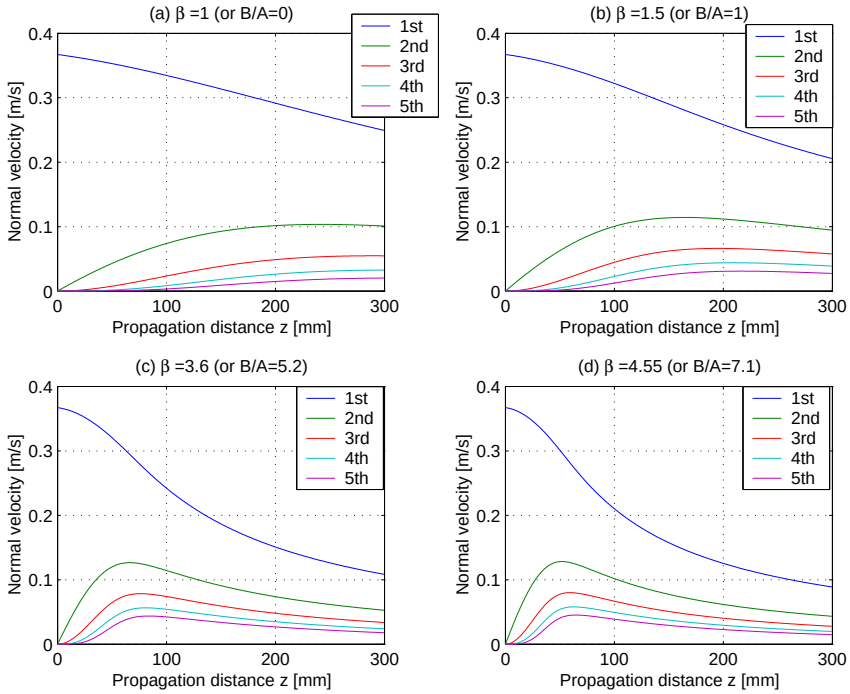

Figure 3.1: Growths of harmonics for different nonlinearity parameters β when I_0 = 10.0 W/cm^2 (or V_0=0.3284 m/s), f_0 = 5 MHz, c = 1484 m/s, ρ = 1000 kg/m^3, α_0= 0.025 NP/m/MHz^2, and b = 2. (a) β=1 (B/A=0), (b) β=1.5 (B/A=1), (c) β=3.6 (B/A=5.2), and (d) β=1.5 (B/A=7.1).

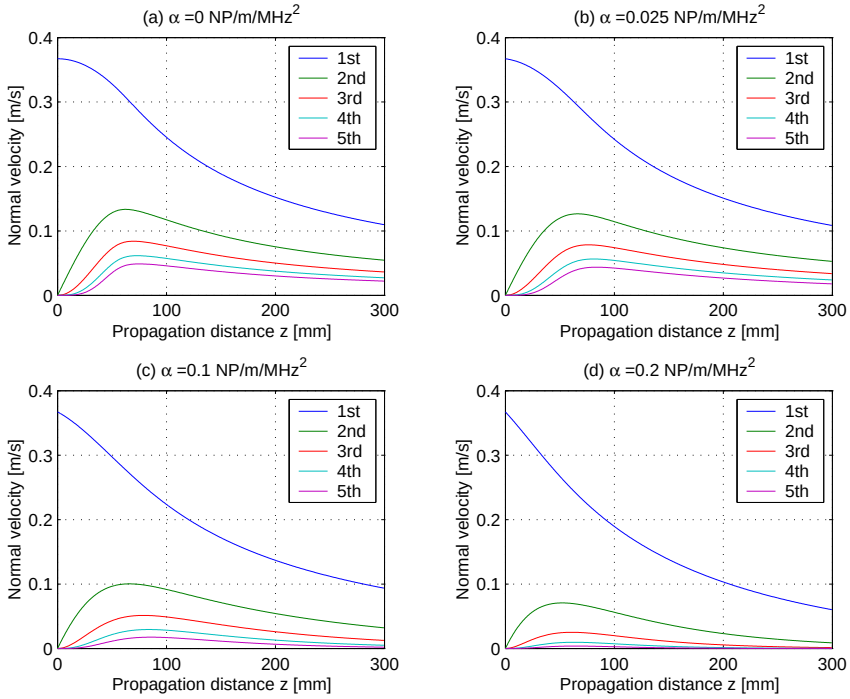

Figure 3.2: Growths of harmonics for different attenuations α when β=3.6 (B/A=5.2), $I_0 = 10.0$ W/cm^2 (or V_0=0.3284 m/s), $f_0 = 5$ MHz, $c = 1484$ m/s, $\rho = 1000$ kg/m^3, and $b = 2$. (a) α=0 Np/m/MHz^2, (b) α=0.025 Np/m/MHz^2, (c) α=1.0 Np/m/MHz^2, and (d) α=2.0 Np/m/MHz^2.

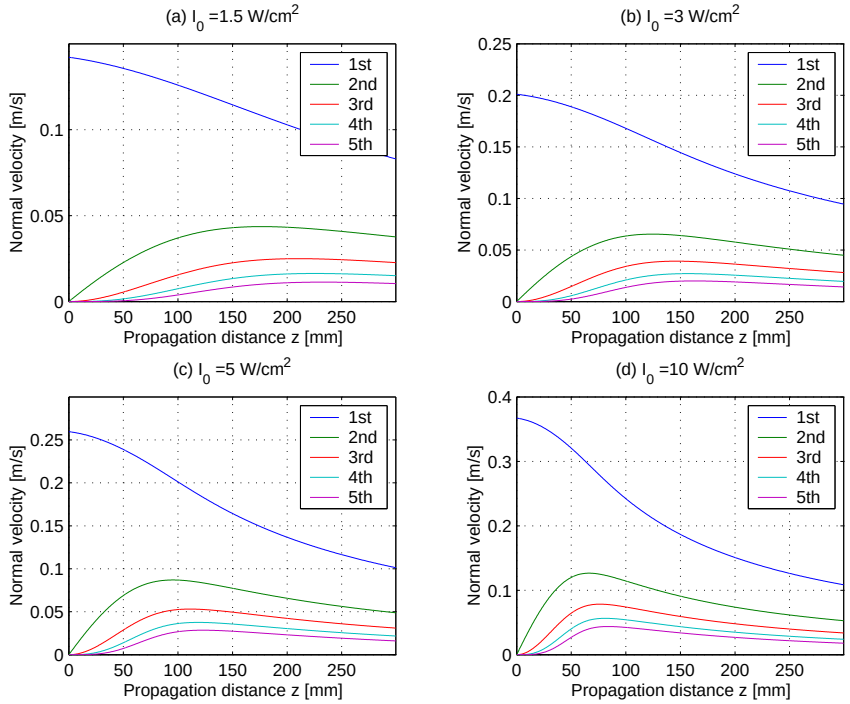

Figure 3.3: Growths of harmonics for different initial acoustic intensities I_0 when β=3.6 (B/A=5.2), $f_0 = 5$ MHz, $c = 1484$ m/s, $\rho = 1000$ kg/m^3, α_0= 0.025 NP/m/MHz^2, and $b = 2$. (a) I_0=1.5 W/cm^2, (b) I_0=5 W/cm^2, (c) I_0=1.5 W/cm^2, and (d) I_0=10 W/cm^2.

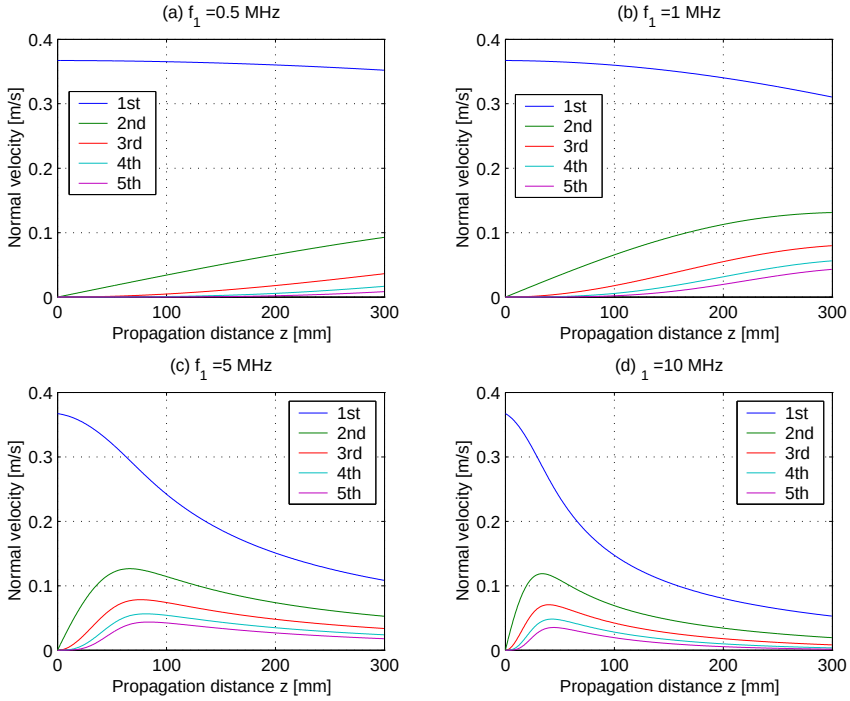

Figure 3.4: Growths of harmonics for different fundamental frequencies f_0 when β=3.6 (B/A=5.2), I_0 = 10.0 W/cm^2, c = 1484 m/s, ρ = 1000 kg/m^3, α_0= 0.025 NP/m/MHz^2, and $b = 2$. (a) f_0=0.5 MHz, (b) f_0=1 MHz, (c) f_0=5 MHz, and (d) f_0=10 MHz.

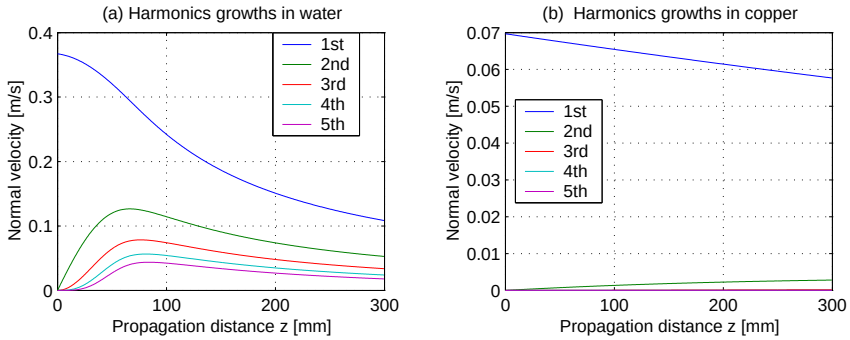

Figure 3.5: Growths of harmonics in (a) water (β=3.6, c = 1484 m/s, ρ = 1000 kg/m^3), and (b) copper material (β=4.54, c = 4596 m/s, ρ = 8960 kg/m^3) when I_0 = 10.0 W/cm^2, f_0=0.5 MHz, α_0= 0.025 NP/m/MHz^2, and $b = 2$.

3.3 Nonlinear propagation of ultrasonic beams

Unlike a plane wave, a finite-amplitude ultrasonic beam from a transducer of a finite aperture shows nonlinear behavior as well as diffractive property in propagation. Thus, simulation of the nonlinear propagation of an ultrasonic beam is much more complicated because of diffractive property. Investigation of this issue is aimed to provide means for analyzing and interpreting measurement results, and for guiding our research (e.g., building an appropriate inspection setup, etc).

In the current case, we consider the ultrasonic beam radiated by an annular transducer, the outer element of the two-element annular array that has been used for harmonic imaging (see [37] for details). The annular transducer has a 2.26-MHz center frequency, an inner radius of a_1 =10 mm an outer radius of a_2 =19 mm, and is spherically focused with a focal length of F = 210 mm.

The transmitter was excited by a toneburst and the nonlinear propagation of ultrasonic beams radiated by the spherically annular transducer have been measured and simulated.

3.3.1 Measurements

Nonlinear acoustic fields radiated by the annular transducer were measured using a hydrophone (made by Precision Acoustics Ltd, UK, with a 0.2-mm diameter and a 0.2-to-30-MHz broad bandwidth, and with a 0.2-mm diameter and a 0.2-to-30-MHz broad bandwidth) and the ALLIN system. The measurement setup is shown in Figure 3.6.

The transducer was driven by a narrow band excitation from the RITEC system, which was a 8-cycle toneburst with a 2.30-MHz frequency and 400 volts peak-to-peak V_{pp}. The parameters used were the same as those used for the harmonic imaging of copper canisters in our previous work [34, 37].

The hydrophone is connected to a preamplifier, whose output goes in one way to the ALLIN's reception, or in another way to a digital oscilloscope (Tektronix TDS-210) and a PC-computer (acquiring data from the oscilloscope). The hydrophone-ALLIN system was used to perform the mechanical scanning, position the hydrophone as well as acquire data (in a form of C-scan or B-scan), and the hydrophone-oscilloscope system was used to acquire waveforms at desired measurement positions (since the oscilloscope is of broader bandwidth we may get a signal with a less distortion).

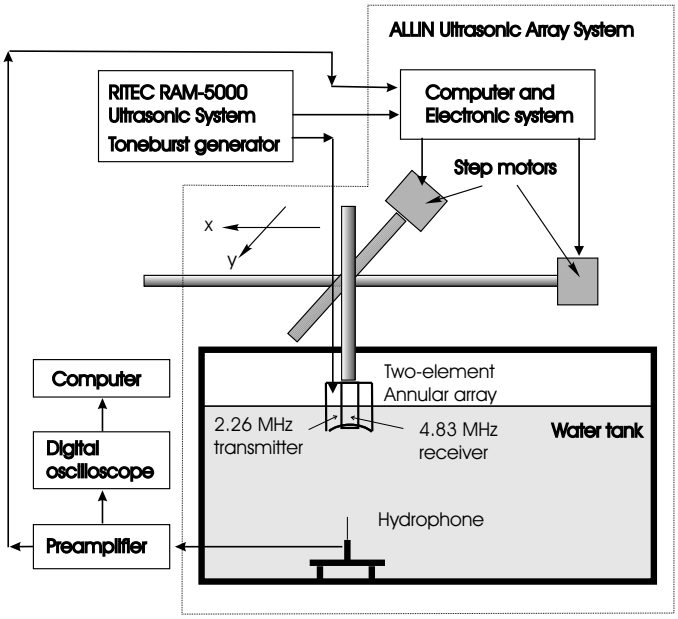

Figure 3.6: Experimental setups.

Using the hydrophone-ALLIN system, measurements of nonlinear acoustic fields were made across the z-axis at three distances z=5, 12, and 31 mm, and are shown in Figures 3.7, 3.8 and 3.9, respectively. In each of the figures, panel (a) shows the cross-axis measurement and panel (b) shows a profile, along the x-axis at $y = 0$ mm in (a). From these measurements, we can see that due to the annular geometry the on-axis fields at z=5 and 12 mm are small and the off-axis ones are large in the geometric range of the annular transducer, e.g., $\sqrt{x^2 + y^2}$=12 to 18 mm for z=5 mm and $\sqrt{x^2 + y^2}$=12 to 17 mm for z=12 mm; but at a little larger distance z=31 mm, the on-axis field becomes a little larger than the maximum off-axis one at $\sqrt{x^2 + y^2}$=13 mm.

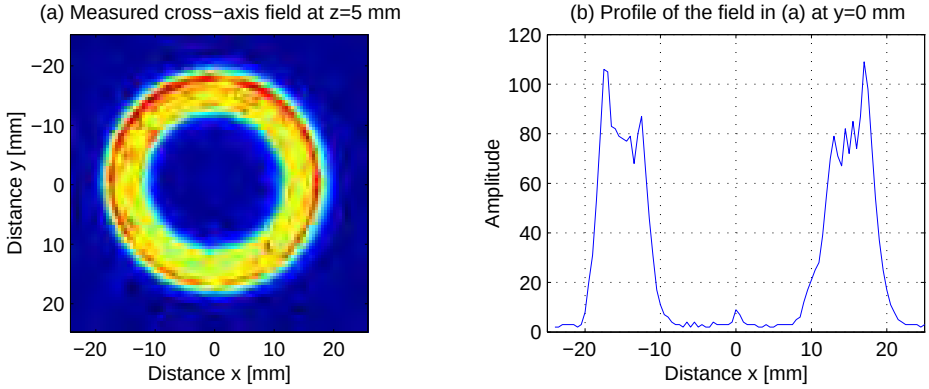

Figure 3.7: (a) Cross-axis measurement of the acoustic field using the hydrophone-ALLIN system (at z=5 mm) and (b) the field profile at y=0 in (a).

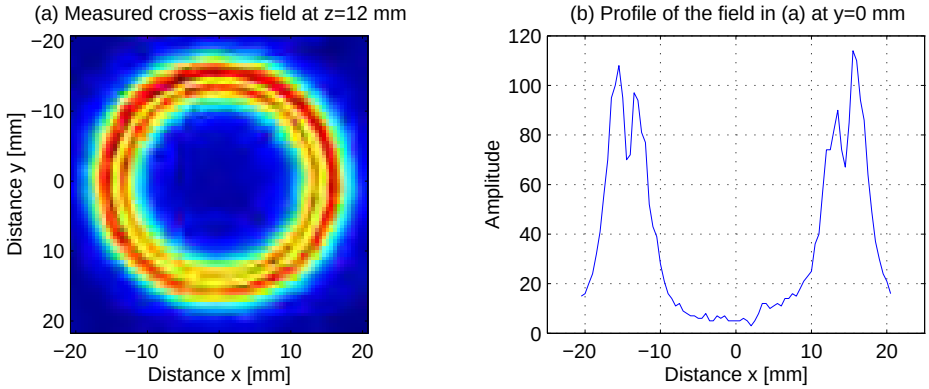

Figure 3.8: (a) Cross-axis measurement of the acoustic field using the hydrophone-ALLIN system (at z=12 mm) and (b) the field profile at y=0 in (a).

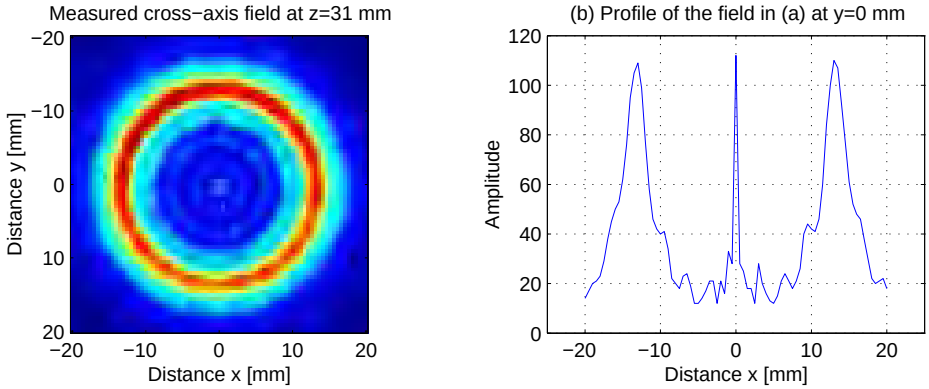

Figure 3.9: (a) Cross-axis measurement of the acoustic field using the hydrophone-ALLIN system (at z=31 mm) and (b) the field profile at y=0 in (a).

After each of the cross-axis measurements (Figures 3.7, 3.8) and 3.9) was made, it was used to position the hydrophone at any desired measurement point (which is a function of the ALLIN system). Then the hydrophone was connected to the oscilloscope (the hydrophone-oscilloscope system) to measure transmitted waveforms (toneburst pulse). The waveforms were measured at four different position, i.e., three off-axis positions, (x,y,z)=(17,0,5), (15.5,0,12) and (13,0,31) mm and one on-axis position (x,y,z)=(0,0,31) mm, at which the signal amplitudes are maxima in the planes across the axis. The measured waveforms and the corresponding spectra are shown in Figures 3.10, 3.11 and 3.12, respectively.

Looking at the spectra of the off-axis waveforms in the figures, i.e., 3.10(a), 3.11(a) and 3.12(d), we can see that the higher (e.g., 2nd and 3nd) harmonics become larger for larger propagation distances.

All these higher harmonics will also travel into the immersed copper so that the nonlinear signals from inside the copper material contain higher harmonics from two contributions: one from water and the other from the copper material.

From the waveforms measured on the axis at z=31 mm and the corresponding spectra (Figure 3.12(a) and (b)) we can see that the 2nd and 3rd harmonics are small (about 37 and 50 dB lower than the fundamental) although the maximum of the waveform amplitude is larger than the off-axis one. The reason is that the larger amplitude is due to the constructive interference occurring in the overlapped part (approx. 23 to 25 μs in Figure 3.12 (a)) of the two waves that are from the inner and outer edges of the annular transducer, respectively), although each of the two waves is smaller. The nonlinearity off the axis at z=31 mm become significantly large, which is shown in the off-axis measurement in Figure 3.12(d) in which the second and third harmonics are clearly seen and much larger than those in the on-axis measurement.

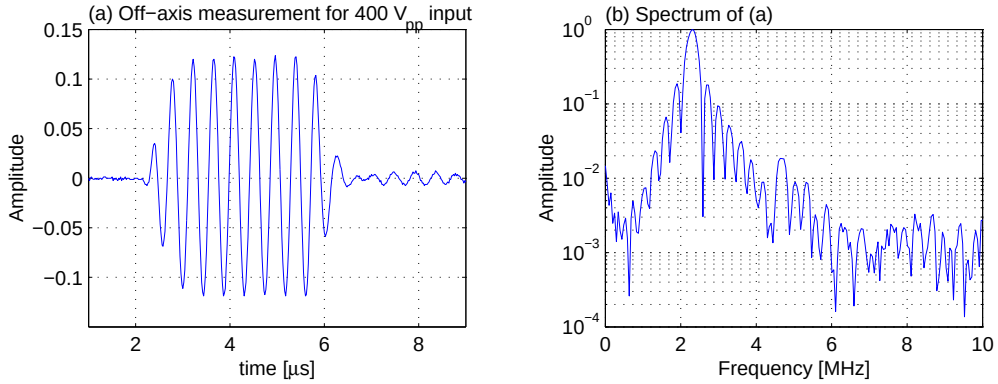

Figure 3.10: Off-axis measurement of nonlinear acoustic fields using the hydrophone-oscilloscope system at (x, y)=(17, 0) mm for z=5 mm. (a) The measured waveform and (b) its spectrum.

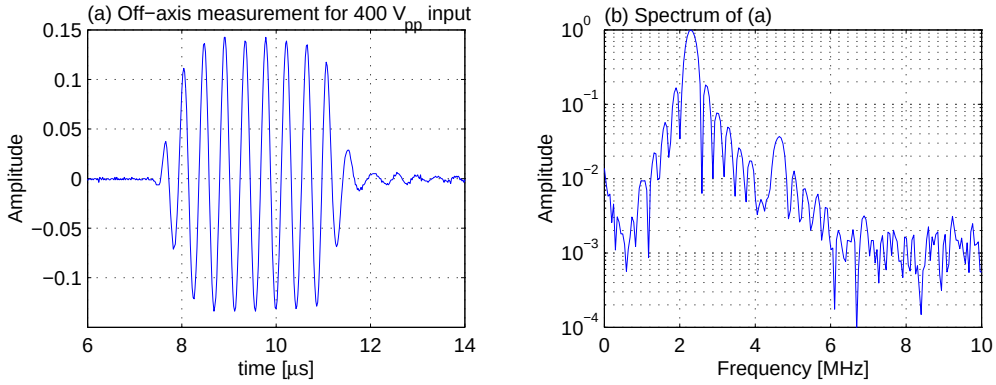

Figure 3.11: Off-axis Measurement of nonlinear acoustic fields using the hydrophone-oscilloscope system at (x, y)=(15.5, 0) mm for z=12 mm. (a) The measured waveform and (b) its spectrum.

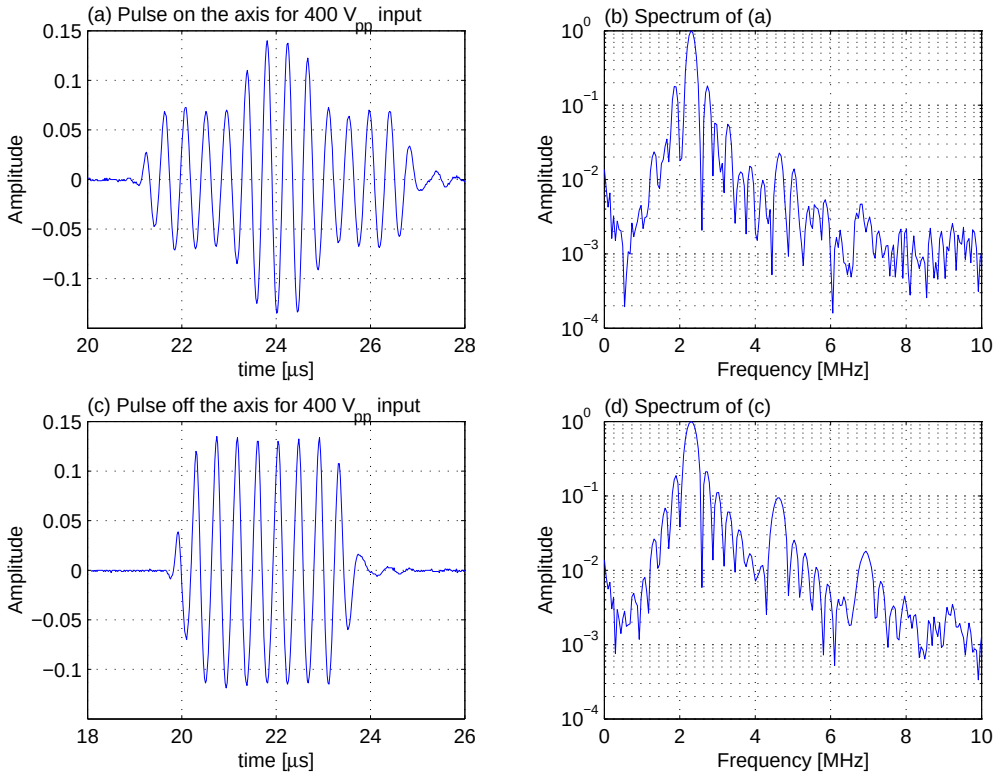

Figure 3.12: On- and off-axis measurements of nonlinear acoustic fields at z=31 mm using the hydrophone-oscilloscope system. (a) The measured waveform on the axis and (b) its spectrum; (c) the measured waveform off the axis at (x, y)=(13, 0) mm (d) its spectrum.

3.3.2 Computer simulations

Computer simulations of nonlinear propagation of ultrasonic beams have been carried out since last year.

The program implemented last year can simulate the nonlinear propagations in fluids and in immersed solids without taking into account the harmonics generated in water [37]. This program has been extended in this year to simulate the nonlinear propagation in immersed solids by taking into account the total harmonics, which include those generated in water (and transmitted into the immersed solid) and those in the immersed solid.

The extended program can provide us with a tool to study, in harmonic imaging an immersed copper material, the impact of the harmonics generated in water on the total harmonics in the immersed material.

The simulations were made for the setup used in the measurements (presented in 3.3.1) so that the simulated results are closer to the ones in the real situation.

The method used to treat the diffractive effect and the nonlinear effect in the simulations is the same as previously, the angular spectrum approach plus Burgers equation, respectively. For the details on the method see our latest SKB report [37].

It should be pointed out that some bugs in the previous program were found that resulted in some errors in the figures (Figures 2.20 and 2.21) in our most recent SKB report [37]. The result in Figure 2.20 should be for the initial intensity 1.5 W/cm^2, and the result in Figure 2.21 for the immersion case should be for the initial acoustic intensity of 74.2 W/cm^2, which was much larger than the correct initial value (1.5 W/cm^2) so that the much stronger harmonics were seen in the immersed copper block. Now these bugs have been fixed, and the results are re-produced.

Besides, a stability problem of the algorithm showed up for a larger initial acoustic intensity (e.g., I_0=4 W/cm^2). Specifically, the algorithm for I_0=4 W/cm^2 and $\Delta z = 0.5$ mm showed to be unstable (i.e., divergent) at a distance just a little further than the near-and-far transit position. Thus, we have looked into the factors (e.g., the step size Δz, the number of retained harmonics, attenuation for a given initial acoustic intensity) that have effects on the algorithm convergence. After serval trials it was found that the algorithm convergence could be guaranteed using small propagation step size Δz, but the cost will be a much longer computation time. Thus, developing efficient algorithms for nonlinear ultrasonic simulation can still be an interesting topic in the future work.

In the simulations, the parameters used are the following

Source parameter: the annular transducer has the inner and outer radii a_1 =10 mm, and a_2 =19 mm, and the radius of curvature F = 210 mm. A sinusoidal continuous wave with a 2.3-MHz frequency is used to excite the transducer, and the initial source intensity 4W/cm^2, which was based on the measurements in water (3.3.1).

Media parameters: the sound speed in water is 1484 m/s, the LW and SW speeds in copper equal to 2260 m/s and 4596 m/s, respectively. The densities of water and copper 1000 kg/m^3 and 8960 kg/m^3, respectively. The attenuation coefficients α in water is 0.217 dB/m/MHz^2 (or 0.025 Np/m/MHz^2) and in copper is 17 dB/m/MHz (or 1.957 Np/m/MHz) ([34], p. 3-23). The nonlinearity parameter β in water is 3.6 (or B/A=5.2) ([39], [40], p. 33 and [38]) and in copper is 4.54, respectively ([19, 22, 40]). In the immersion case, water layer is 31 mm thick.

Numerical calculation parameters: propagation step size Δz=0.1 mm for the water case, and Δz=0.5 mm for the immersed copper case since nonlinearity growth is much slower in the immersed copper block.

The simulations have been made for three cases:

- Nonlinear acoustic field in water for two different initial acoustic intensities, I_0=1.5 and 4 W/cm^2, shown in Figures 3.13 and 3.14, respectively
- Nonlinear acoustic field in immersed copper block without taking into account into the nonlinear distortion in water also for I_0=1.5 and 4 W/cm^2, (see Figures 3.15 and 3.16, respectively)
- Nonlinear acoustic field in water and in immersed copper block with the nonlinear distortion in water taken into account for I_0= 4 W/cm^2 (Figure 3.17).

Note that the logarithmic scales of the spectra in Figures 3.13, 3.14 and 3.17 are from 10^{-4} to 2, very different from those (from 10^{-10} to 2) in Figures 3.15 and 3.16.

Comparing the results for two different initial intensities (Figures 3.13 and 3.15 for I_0=1.5 W/cm^2, and Figures 3.14 and 3.16 for I_0=4 W/cm^2) , we can see that a larger I_0 results in a faster growth of higher harmonics.

The results in Figures 3.14 and 3.16 for I_0=4 W/cm^2 show that the harmonics grow much faster in water with distance than in immersed copper.

In the immersion case, the harmonics generated in water are partly transmitted by the water-copper interface and propagate further in the immersed copper and contribute to amount of harmonics in the immersed copper. The simulated results in this case are shown in Figure 3.17, from which we can see that the harmonics in the immersed copper are much stronger than those as in Figure 3.16.

This demonstrates that the harmonics generated in water may have large contribution to the harmonics in immersed copper material when the water layer is 31 mm.

From this work, we may conclude that

- when using nonlinear propagation effect for harmonic imaging in immersion case, the effect from the water layer is significantly large if the water is not thin enough, and
- when using harmonics to evaluate nonlinear elastic properties (e.g., third-order elastic constants, nonlinearity parameter) of a solid in immersion measurement, the influence of the harmonics generated in an immersing fluid must be taken into account;
- the best way to avoid the effect from water is to use contact test configuration.

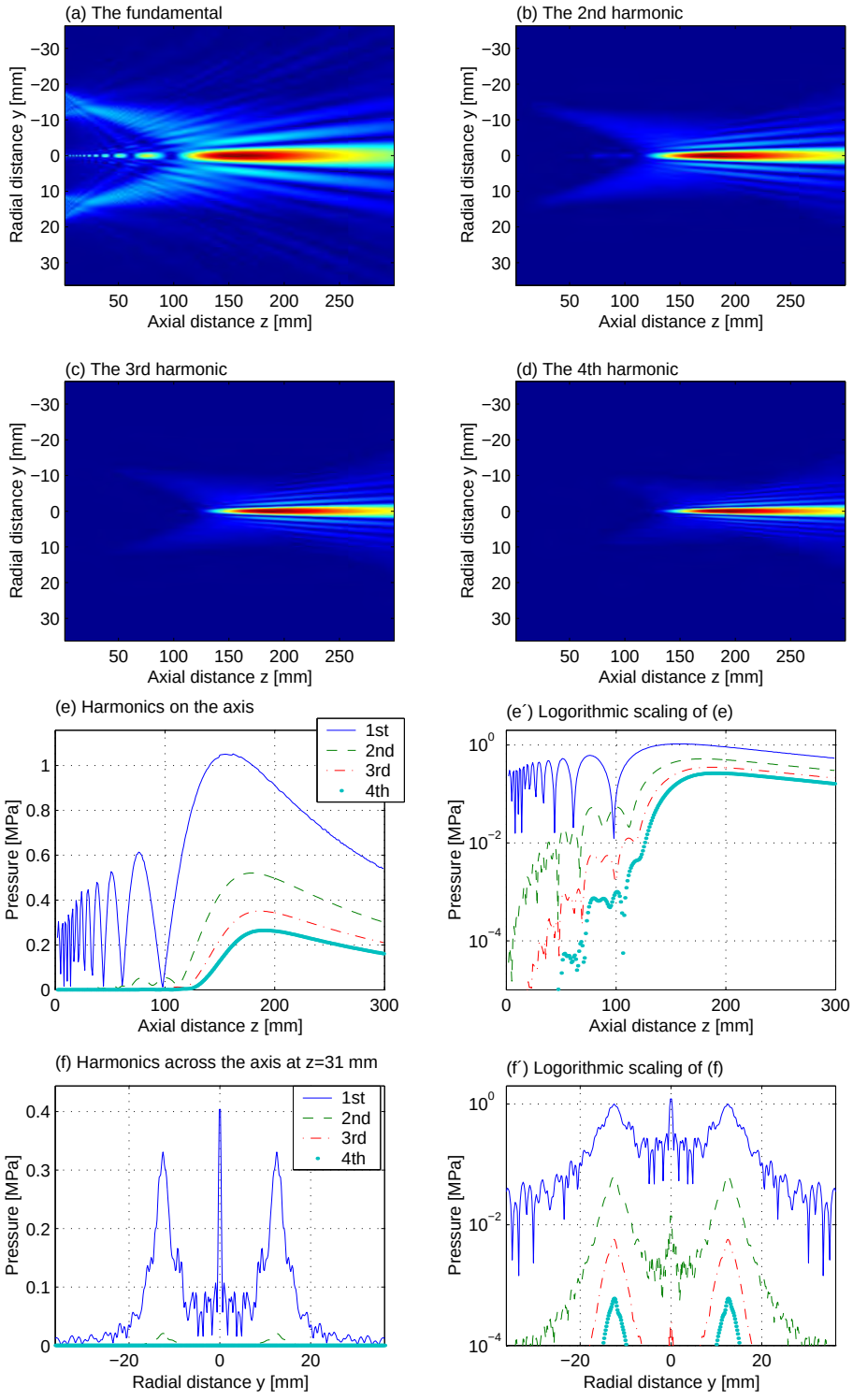

Figure 3.13: Simulated nonlinear acoustic fields in water with an initial acoustic intensity of I=1.5 W/cm^2. (a) the fundamental, (b) the 2nd, (c) the 3rd and (d) the 4th harmonic in the y-z plane.

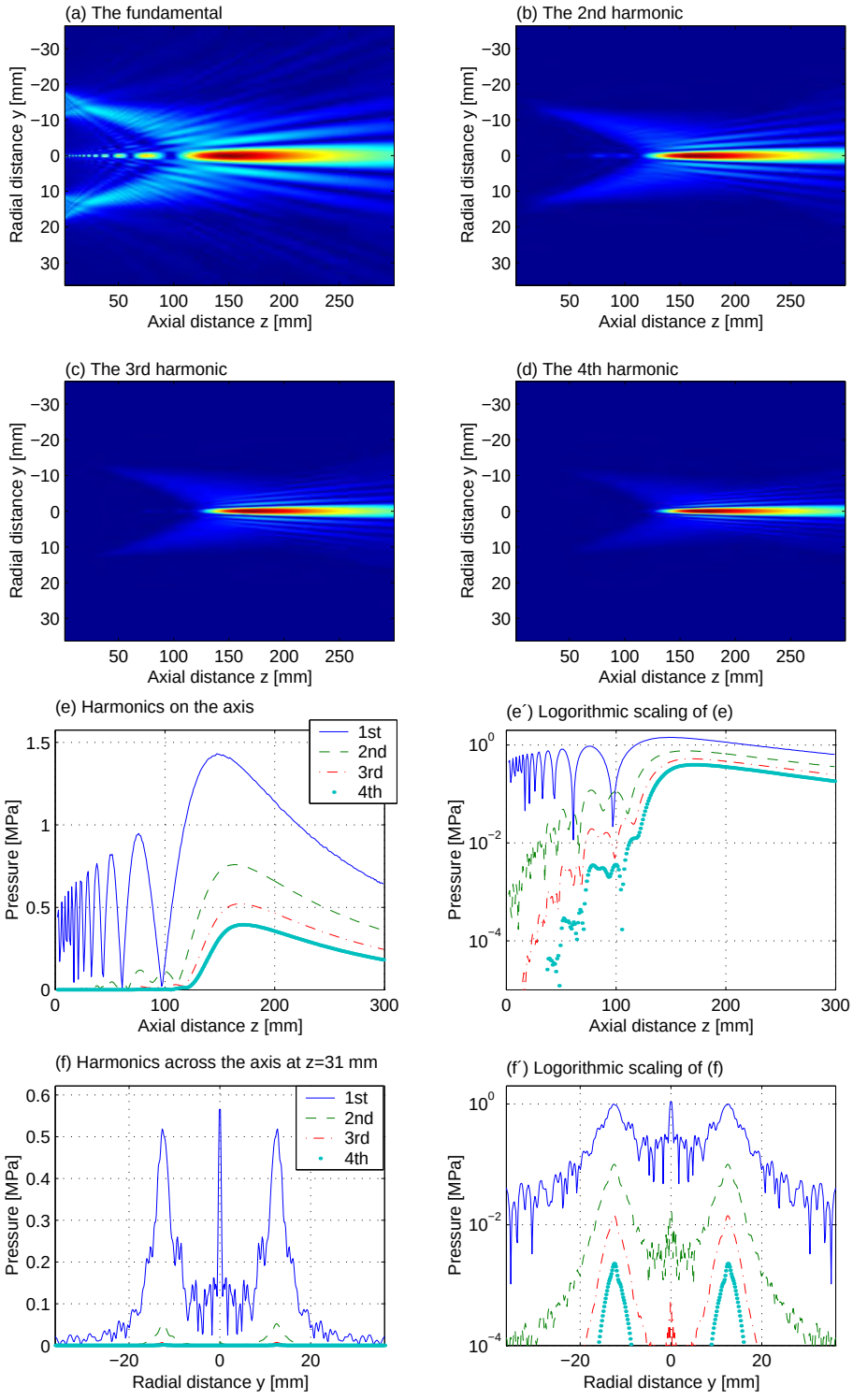

Figure 3.14: Simulated nonlinear acoustic fields in water with an initial acoustic intensity of I=4 W/cm^2. (a) the fundamental, (b) the 2nd, (c) the 3rd and (d) the 4th harmonic in the y-z plane.

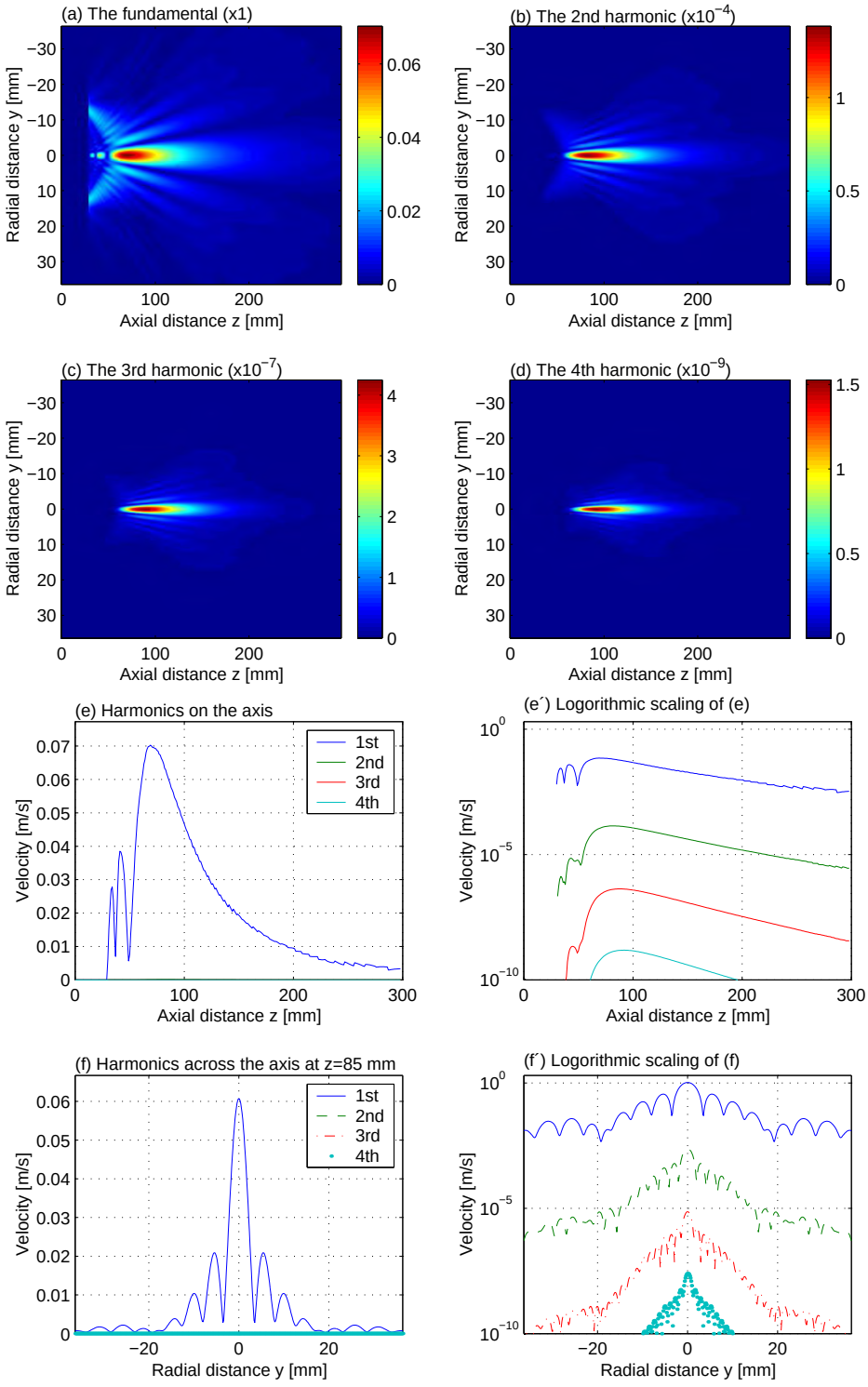

Figure 3.15: Simulated nonlinear elastic fields in an immersed copper block with an initial acoustic intensity of I=1.5 W/cm^2. (a) the fundamental, (b) the 2nd, (c) the 3rd and (d) the 4th harmonic in the y-z plane.

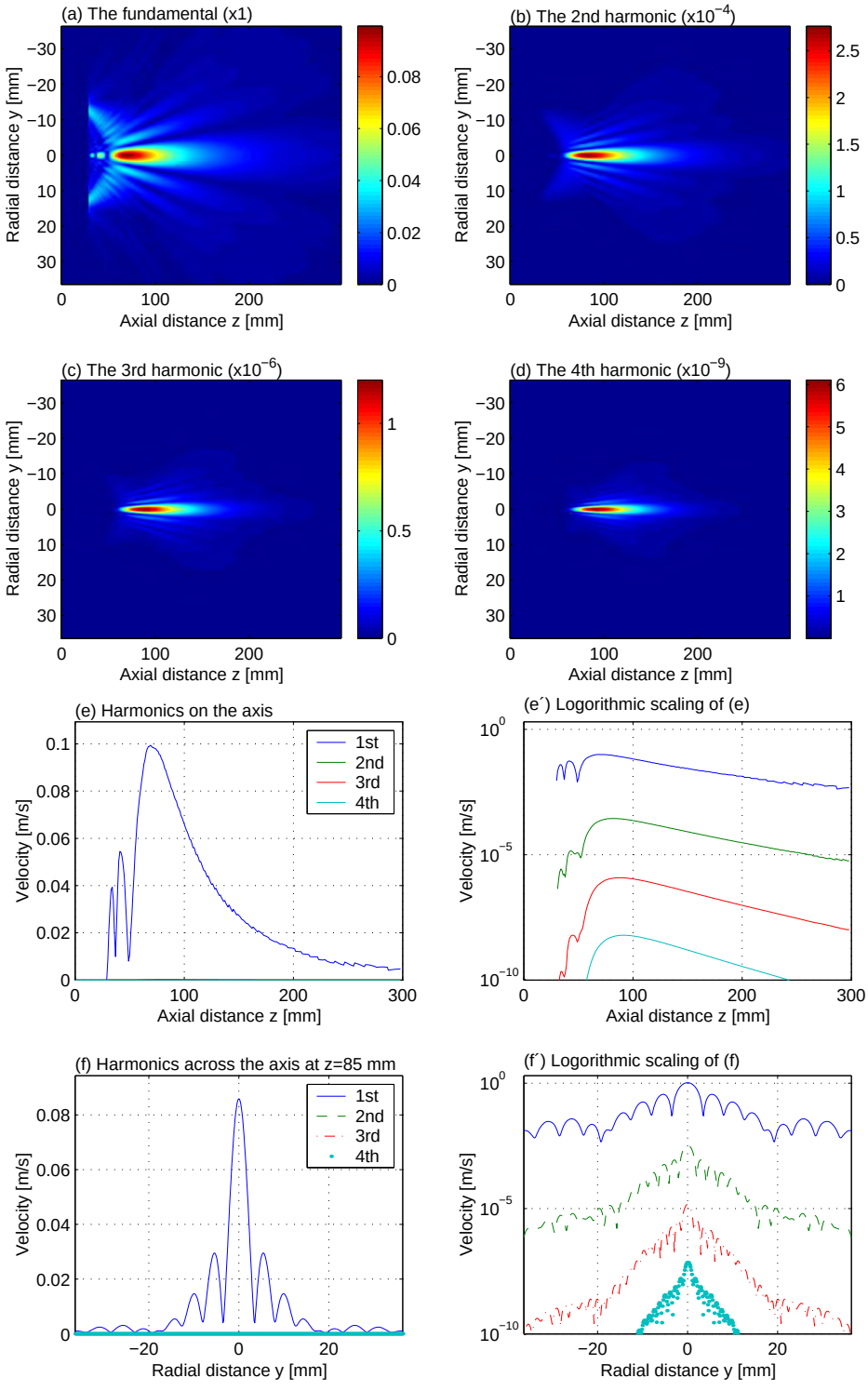

Figure 3.16: Simulated nonlinear elastic fields in an immersed copper block with an initial acoustic intensity of I=4 W/cm^2. (a) the fundamental, (b) the 2nd, (c) the 3rd and (d) the 4th harmonic in the y-z plane.

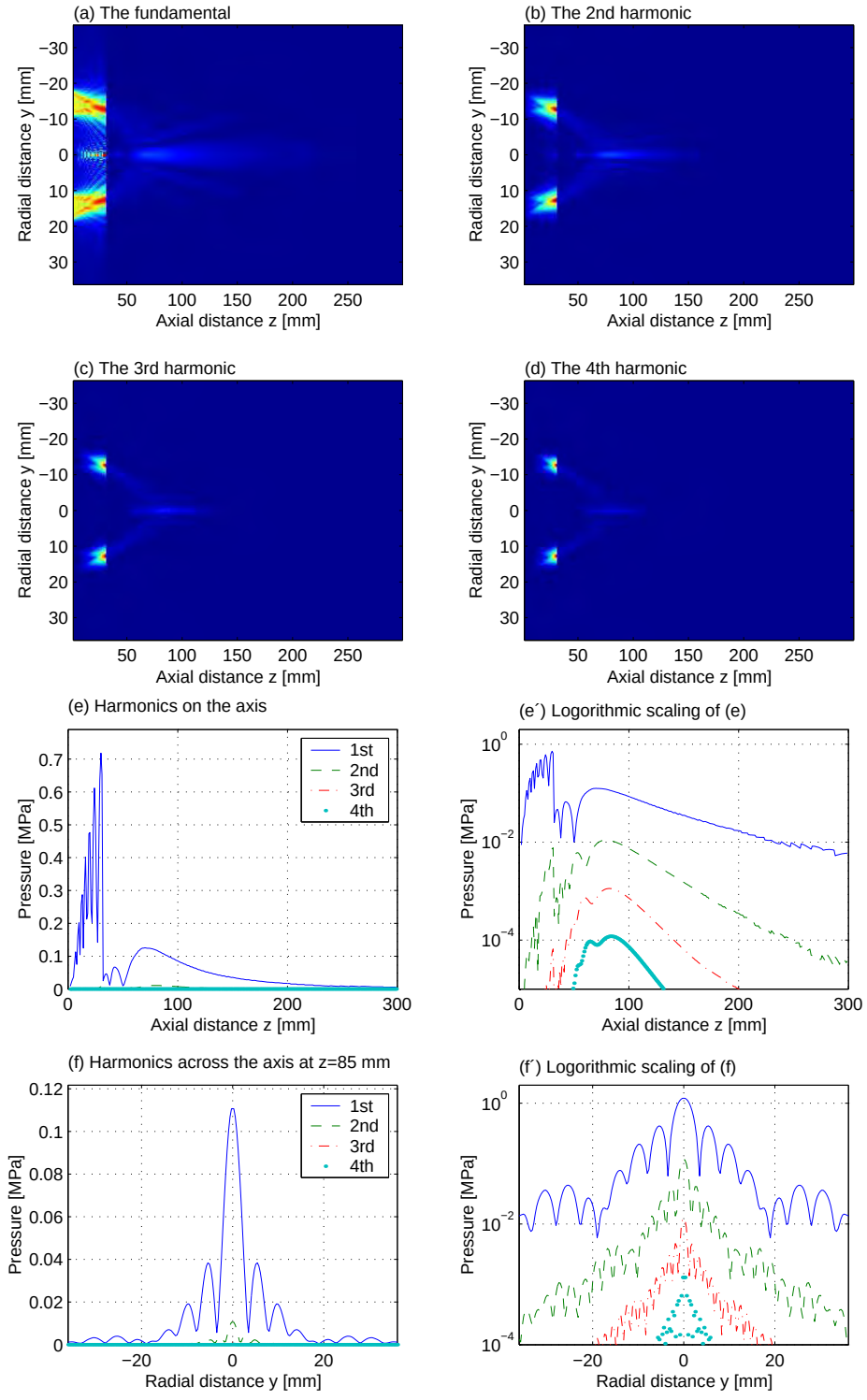

Figure 3.17: Simulated nonlinear fields in water and in immersed copper block with an initial acoustic intensity of I=4 W/cm^2. The water/copper interface is at z= 31 mm. (a) The fundamental, (b) the 2nd, (c) the 3rd and (d) the 4th harmonic in the y-z plane.

3.4 Nonlinear ultrasonic detection of contacts and interfaces

This experimental work was performed to investigate how nonlinear ultrasonics can be exploited to detect contact cracks that are possible defects in friction stir welds. The theory on contact acoustic nonlinearity (CAN) that is behind this nonlinear effect has been studied based on the recently published work [31–33, 41], as well as [27–30].

It should be pointed out that, although high power ultrasound is used in both material harmonic imaging (based on nonlinear propagation) and nonlinear ultrasonic detection of cracks (using crack's nonlinear vibrations), the ultrasonic transducers used in these two cases are different in characteristics. For example, in the former case a high frequency (several MHz) is used for a faster growth of harmonics; whereas in the latter a low frequency (several hundred kHz) is used since a large vibration displacement is desired to excite contact cracks.

As shown in Section 3.2.1, the magnitude of particle displacement in a metal material is often so small as one or two millionth of the wavelength. If a gap between the two surfaces that form an interface is larger than this magnitude value, the nonlinear vibration of the interface can not occur. In this case the interface is often detectable using linear ultrasound.

To investigate the CAN of interfaces, contacts and cracks, we have inspected three different sets of copper samples that contain interfaces.

The copper samples of the first set were W117, W92 No8, W143A and W143B, made by TWI for the assessment of radiographic sensitivity, all had a sandwich structure, and their interfaces could be clearly seen from linear ultrasonic inspection (pulse-echo mode) [42]. Nonlinear ultrasonic inspection of the blocks was made in an immersion configuration as used in the previous research on material harmonic imaging [34, 35]. Then, the contact, through-transmission configuration was used for the inspection. In all the inspections no signs of contact acoustic nonlinearity were observed. The reason for this could be that the gaps (forming the interfaces) between two layers' surfaces were so large that the surfaces were not well in contact.

After the inspections, special copper samples were designed for CAN investigation. To make such samples, the SKB produced copper block parts (including a block used as a reference sample CUCAN 0) and Institutet för Metallforskning (IM) bonded some of them, which are the second set of copper samples. The samples were first inspected using linear ultrasound, and the bonds in the samples could be clearly seen. Obviously the bonded surfaces were not in contact. Then they were re-bonded by IM and inspected again. The inspected results have not shown any traces of CAN in those interfaces.

Other two pairs of the copper blocks produced by SKB were bonded by MABU Consulting AB, Lulea, using hot isostatic pressing (HIP) technique. These are the third set of copper samples (CUCAN 1 and CUCAN 2) inspected. A detailed report on the measurements made on these copper samples (CUCAN 1 and CUCAN 2) and the reference sample (CUCAN 0) together with the experimental setup (including evaluating the transducers) is given in section 3.4.1.

3.4.1 Copper samples and linear ultrasonic inspection

The geometry of the copper samples (CUCAN 0, CUCAN 1 and CUCAN 2) in the report are shown in Figure 3.18. Since H_1 and H_2 are different, we can inspect the interfaces at four different depths, namely 30, 40, 50 and 60 mm, if we inspect them from bottom and from top. These different depths gave us a flexibility to select transducers and a possibility to observe the variation of the CAN with interface depth. For example, for a high-power ultrasonic transmitter with a 38-mm diameter and a 0.5-MHz frequency, attached to a copper sample with a sound velocity of 4600 m/s, the last maximum of the on-axis field (i.e., the starting point of the far-field) is at about 39 mm. For such a transducer the copper sample with an interface at 40 mm

should be the best choice.

Samples CUCAN 1 and CUCAN 2 were inspected using the ALLIN system in immersion pulse-echo configuration. The C- and B-scans from the inspection are shown in Figure 3.19. From the figure we can see a few strong indications of defects in CUCAN 1, and one indication in the middle of CUCAN 2.

Copper blocks for CAN measurements

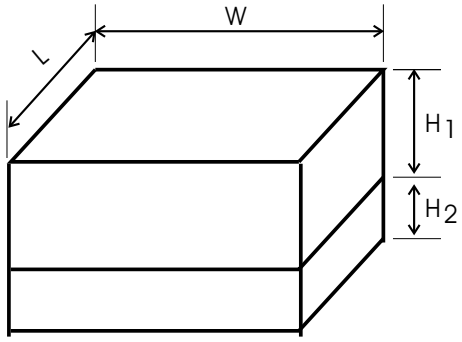

Sample	L (mm)	W (mm)	H_1 (mm)	H_2 (mm)
CUCAN 0	80	80	90	0
CUCAN 1	80	80	50	30
CUCAN 2	80	80	60	40

Figure 3.18: Copper samples CUCAN 0, CUCAN 1 and CUCAN 2 for investigating contact acoustic nonlinearity (CAN).

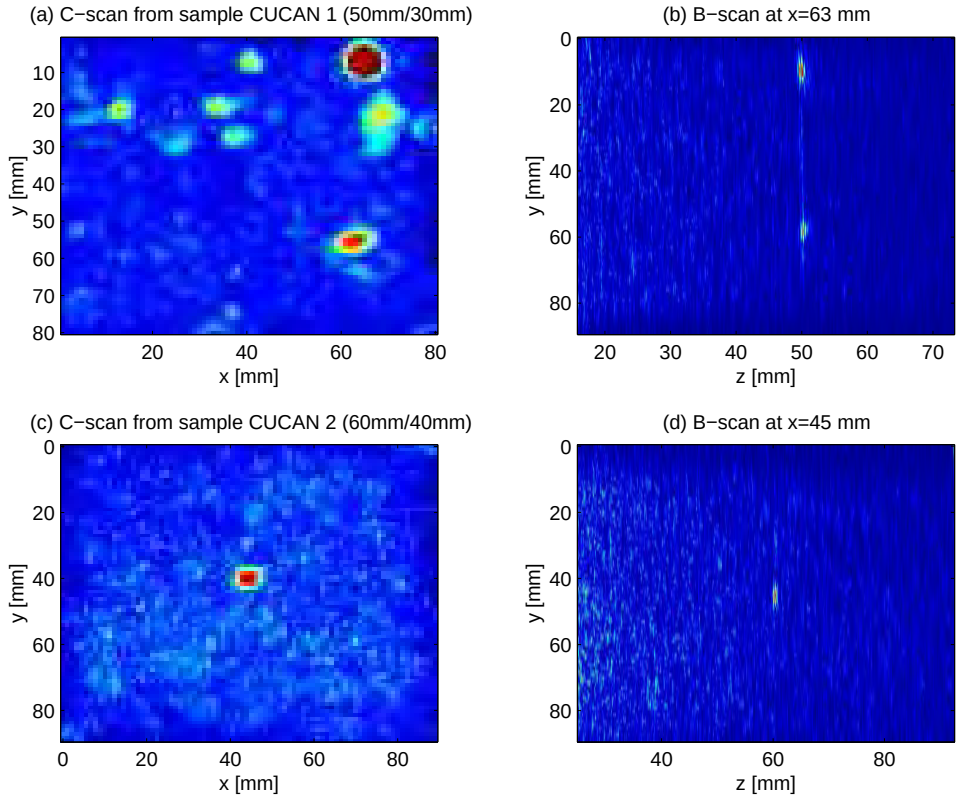

Figure 3.19: Inspection of samples CUCAN 1 and 2 using linear ultrasound. (a) C-scan and (b) B-scan of the interface in sample CUCAN 1 (50mm/30mm); and (c) C-scan and (d) B-scan of the interface in sample CUCAN 2 (60mm/40mm).

3.4.2 Experimental setups for nonlinear ultrasonic inspection

The experimental setup for the nonlinear ultrasonic inspection is shown in Figure 3.20. It consists of a 0.5-MHz transmitter and a 1-MHz receiver (both made by Valpey Fishers Co., USA), RITEC RAM-5000 Ultrasonic System, attenuator and a digital oscilloscope (Inifiniium Oscilloscope 54810AR made by Agilent Technology).

The RITEC System provides us with a high-power narrow band excitation to the transmitter. The oscilloscope with a sampling frequency up to 1 GHz and a FFT function (enabling spectral analysis in real time) is used to record the signals from the receiver.

Before we perform nonlinear ultrasonic inspection of copper samples CUCAN 0-2, we examine the transmitter and receiver, and the RITEC output.

A. Broad band excitation response of the transmitter and receiver

An ultrasonic transducer may have fundamental and higher resonant modes. Although the fundamental mode is desired, both the fundamental and higher resonant modes may also be excited when the transducer is driven by a broadband signal. In this case the effects of the higher harmonics on measurements should be taken into account. To evaluate such effects we looked into the broadband (pulse) excitation responses of the transmitter and the receiver, respectively, using the ALLIN system. The transmitter (or the receiver) was attached to copper block CUCAN 0, and the echo from the block's back surface was measured. The measured echoes for the transmitter and receiver, and their spectra are shown in Figure 3.21. From the spectrum of the transmitter's response (Figure 3.21 (b)), we can see three resonant peaks at the frequencies, 0.52, 1.61 and 2.71 MHz, which correspond to the first, third and fifth resonant modes, respectively. Note that the first resonant peak is a little lower than the second peak because the best available bandwidth of the amplifier was 1 to 30 MHz so that the first peak was much suppressed. But this has a little effect on evaluating the resonant frequencies. The first resonance has a 31% -6 dB bandwidth. The second resonance also looks sharp and narrow. The third peaks is much lower, but still clear seen.

Since the toneburst is not a single frequency signal, instead a narrow band signal, then the high-order resonant modes of the transmitter may also be excited, and their influence may be significant and thus should be considered in analyzing the measured results.

The spectrum of the receiver's response in Figure 3.21 (d) illustrates that the receiver is a broad band transducer with two resonant peaks at the frequencies, 1.14 and 3.14 MHz, which are from the first and third resonant modes, respectively. The first resonance has a 103% -6 dB bandwidth. The second resonance is still quite strong, about 38% of the first one.

B. RITEC output

The RITEC output used in the experiments was a 14-cycle toneburst with a frequency of 0.5 MHz, but with a varied amplitude (in order to observe how the nonlinearity varied with the amplitude). The output amplitude can be changed in 100 levels by changing the gated-amplifier (GA) output control. The peak-to-peak amplitude as a function of the GA output control levels was measured using the oscilloscope with a 20-dB attenuator and the transmitter connected (Figure 3.20), and the measured results in terms of peak-to-peak amplitude are shown in Figure 3.22. The lowest output voltage at 0.5 MHz is 60 V_{pp} at the minimal level of the GA output control, and the highest is 2285 V_{pp} at the maximum level (GA output control 100). It should be pointed out that the output voltage at 2.3 MHz (the frequency used for the annular array transducer) was very different, e.g., the lowest one was 26 V_{pp} [37]. The waveforms (tonebursts) of the outputs with four different amplitudes and their spectra are shown in Figure 3.23. Note that the Hamming window has been applied to all the data to find their spectra.

From the spectra it can bs seen that no pronounced harmonics are seen in the outputs at lower amplitude levels (60 and 1408 V_{pp}), but in the higher output (1888-V_{pp} in Figure (c')) a third-order harmonic at 1.5 MHz is visible and in the 2260-V_{pp} output it becomes bigger (see Figure (d')). This third harmonic is from the third-order resonant mode of the transmitter and its influence on the measurements should be account for. It should be pointed out that the second resonance is not excited and only the third one is seen.

3.4.3 Results

Samples CUCAN 0-2 were inspected using the setup in Figure 3.20. Samples CUCAN 1 and 2 (refer to Figure 3.18) were inspected from bottom and top, respectively. The results for CUCAN 0 (without interface) are presented in Figure 3.24, and the results for CUCAN 1 and 2 (for the interfaces at 30, 40, 50, and 60 mm) are shown in Figures 3.25, 3.27, 3.26 and 3.28.

A common feature that can be easily found from the results in these figures is that the second and third harmonics (at 1 and 1.5 MHz, respectively) increases with peak-to-peak amplitude of the toneburst excitation. A close look at the changes of the second and third harmonics with toneburst amplitude may lead to the conclusion that the second harmonic increases faster than the third one. Since there was no second harmonic from the transmitter (which follows from Figure 3.23), the second harmonic in the received signals should originate from ultrasonic nonlinear propagation. The third harmonic can be partly contributed by the nonlinear propagation and partly by the third resonance of the transmitter, especially when the excitations are large 3.23.

No contact nonlinearity effects from the interfaces can be seen. The reason would be that the interfaces are 'welded' together, instead of kissing bonds (or non-bonded).

(a)

(b)

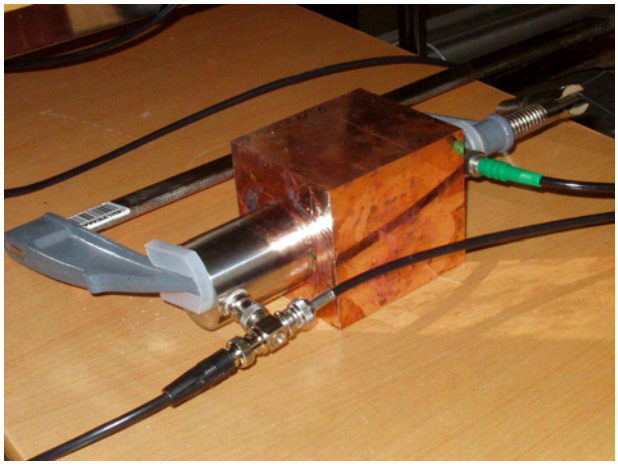

(c)

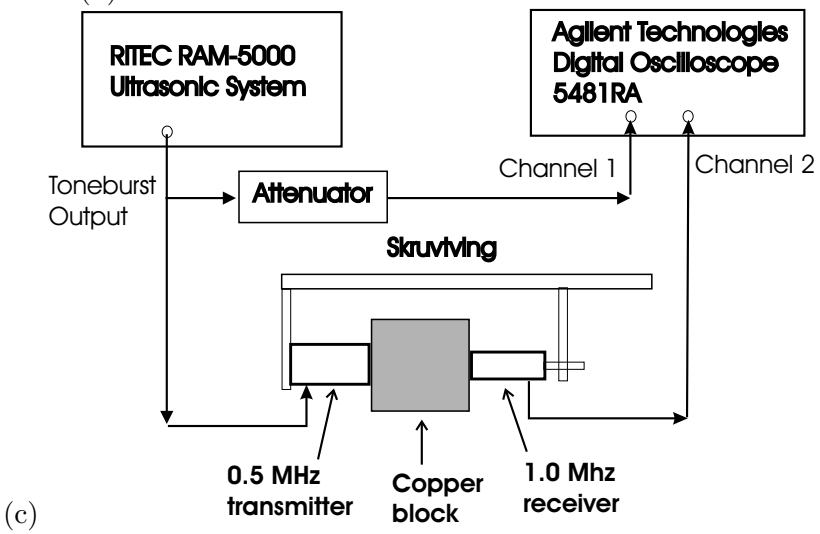

Figure 3.20: Experimental setup for investigating contact acoustic nonlinearity (CAN) in copper samples CUCAN 0, CUCAN 1 and CUCAN 2.

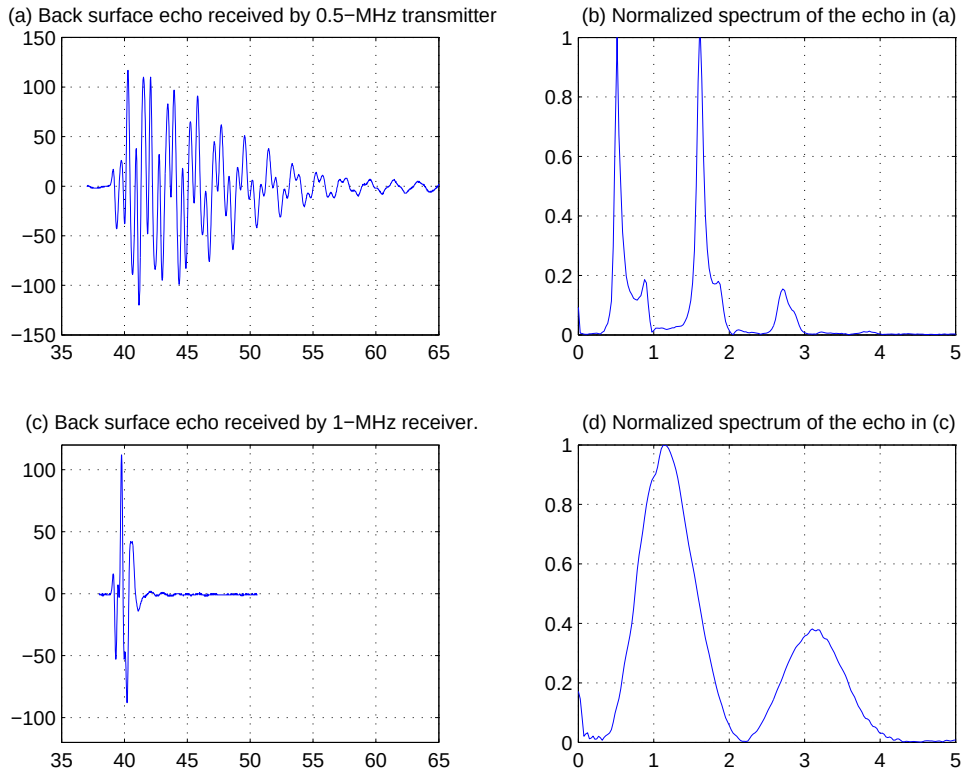

Figure 3.21: Broad band excitation responses of the 0.5-MHz transmitter (narrow band) and the 1-MHz receiver (broadband). (a) CUCAN 0's back surface echo received by the 0.5-MHz transmitter and (b) its spectrum; (c) CUCAN 0's back surface echo from the 1-MHz receiver and (d) its spectrum.

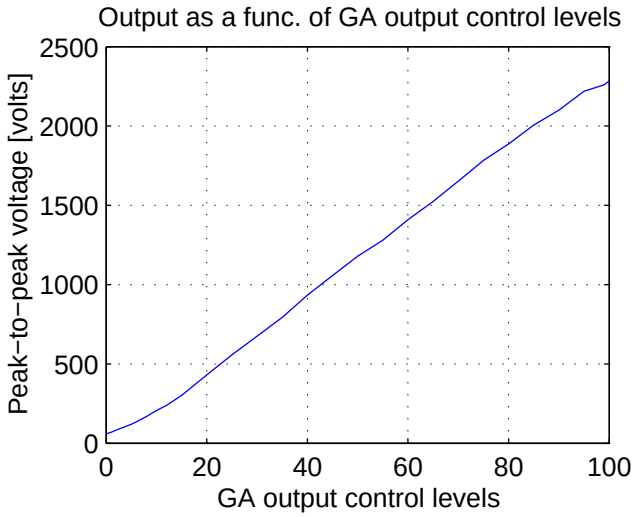

Figure 3.22: RITEC output as a function of GA output control.

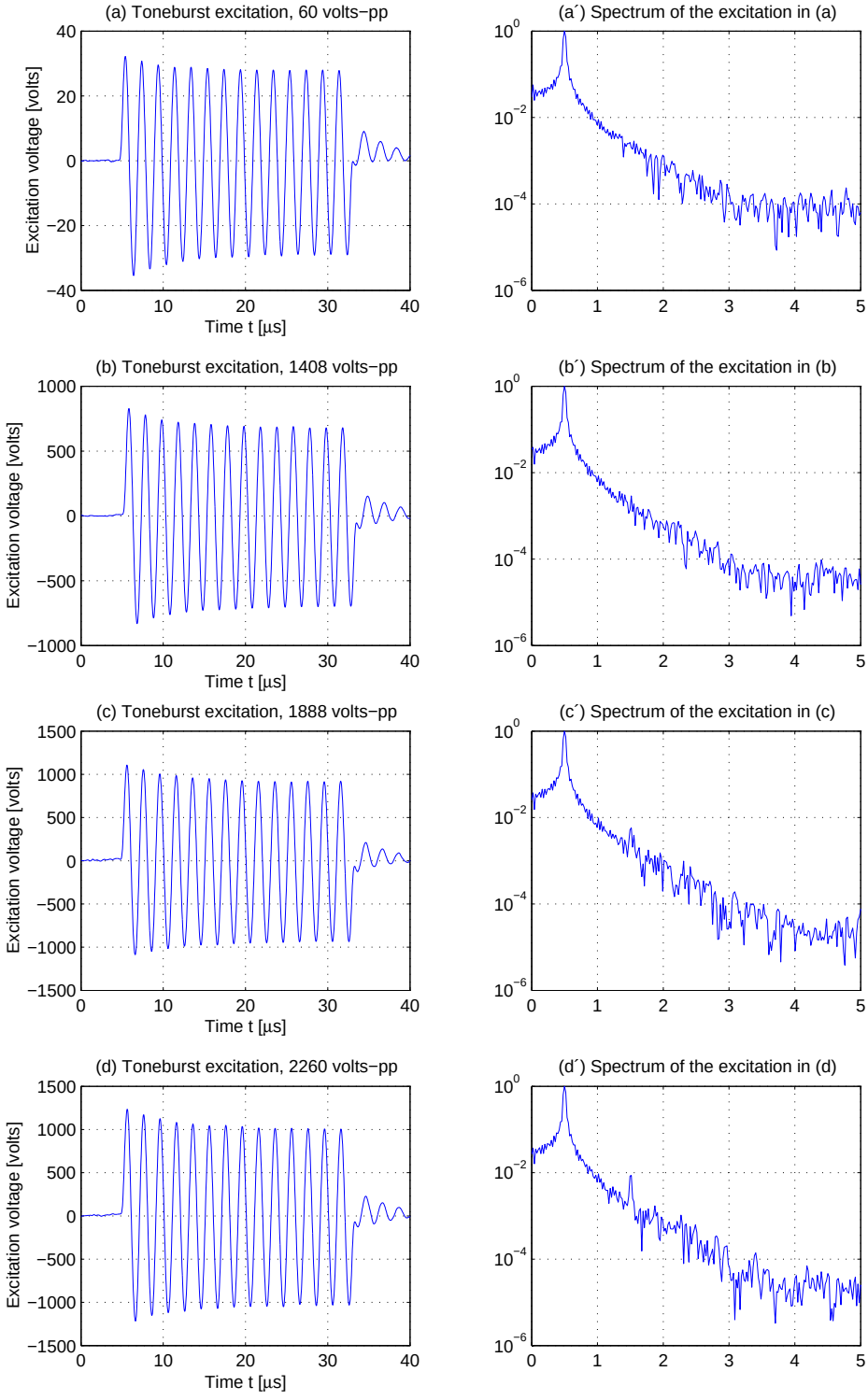

Figure 3.23: Toneburst excitations and their spectra at different voltage levels.

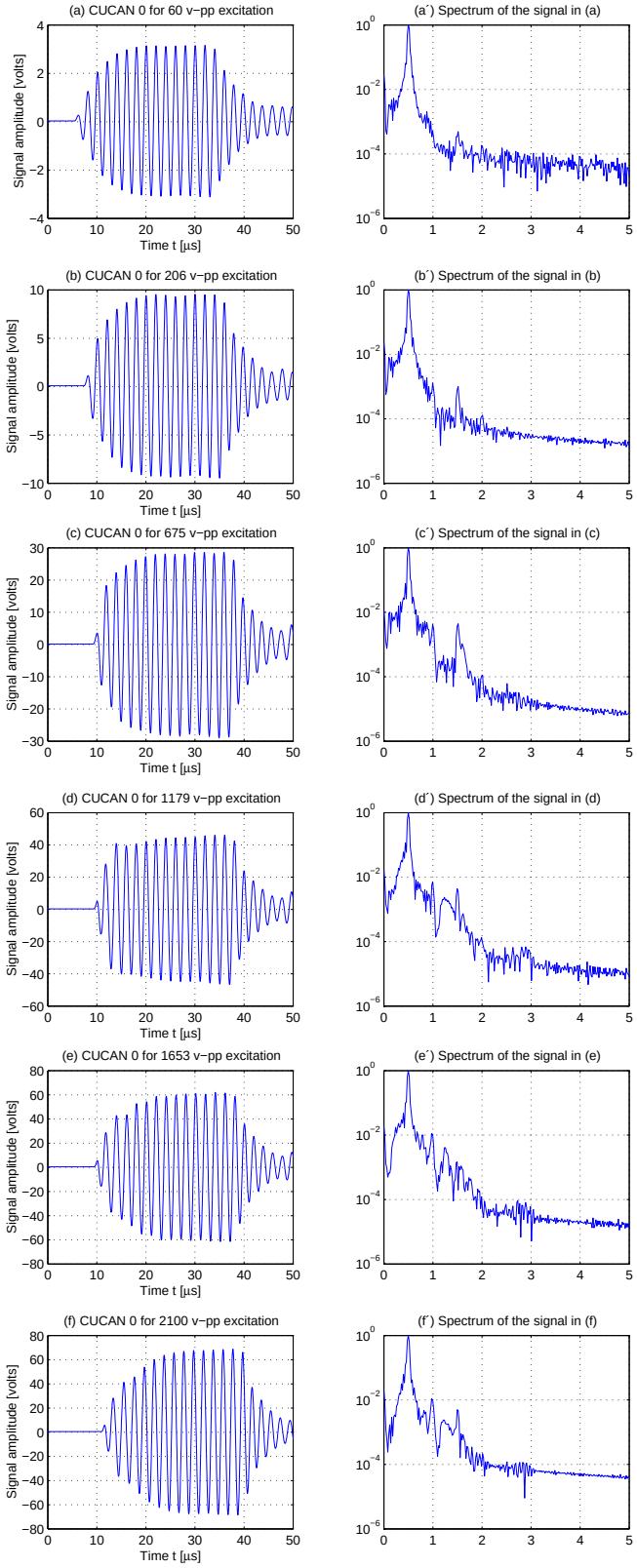

Figure 3.24: Sample CUCAN 0. (a), (b) its spectrum; (c) and (d) its spectrum; (e) and (f) its spectrum.

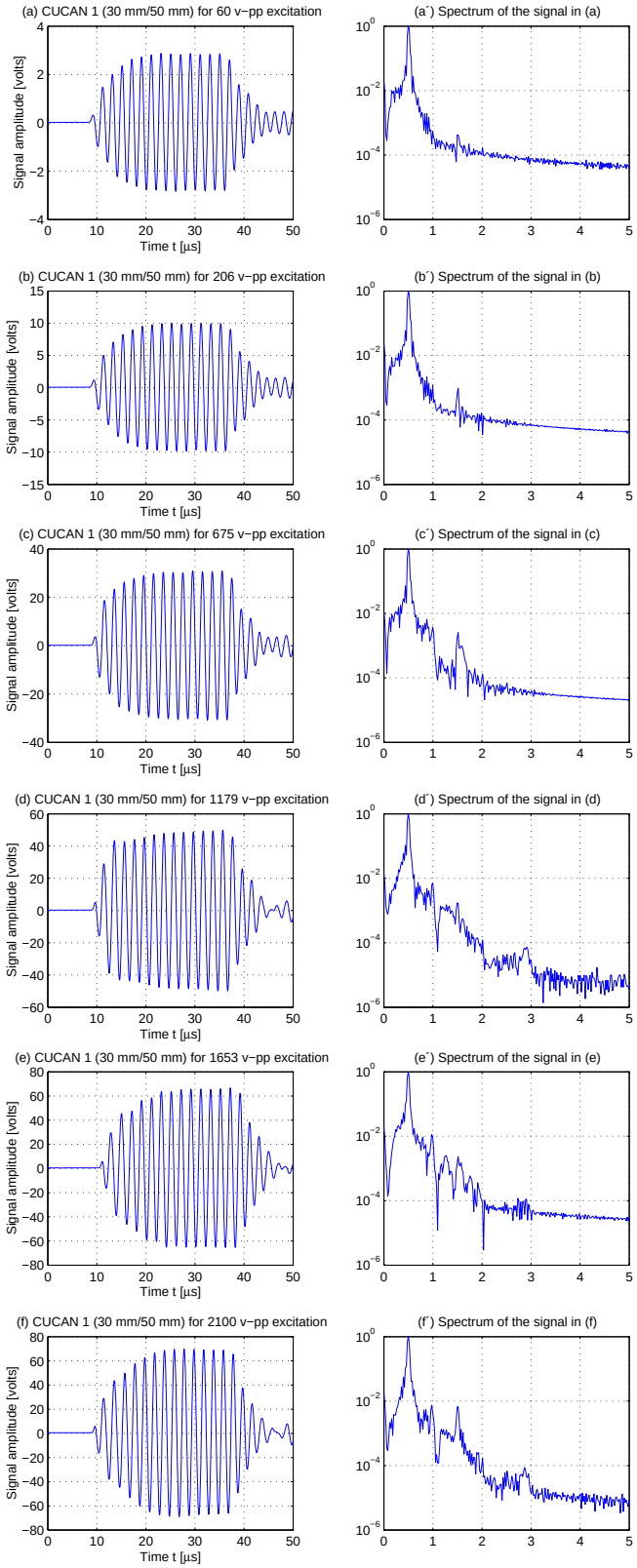

Figure 3.25: CUCAN 1 (30 mm/50 mm). (a), (b) its spectrum; (c) and (d) its spectrum; (e) and (f) its spectrum.

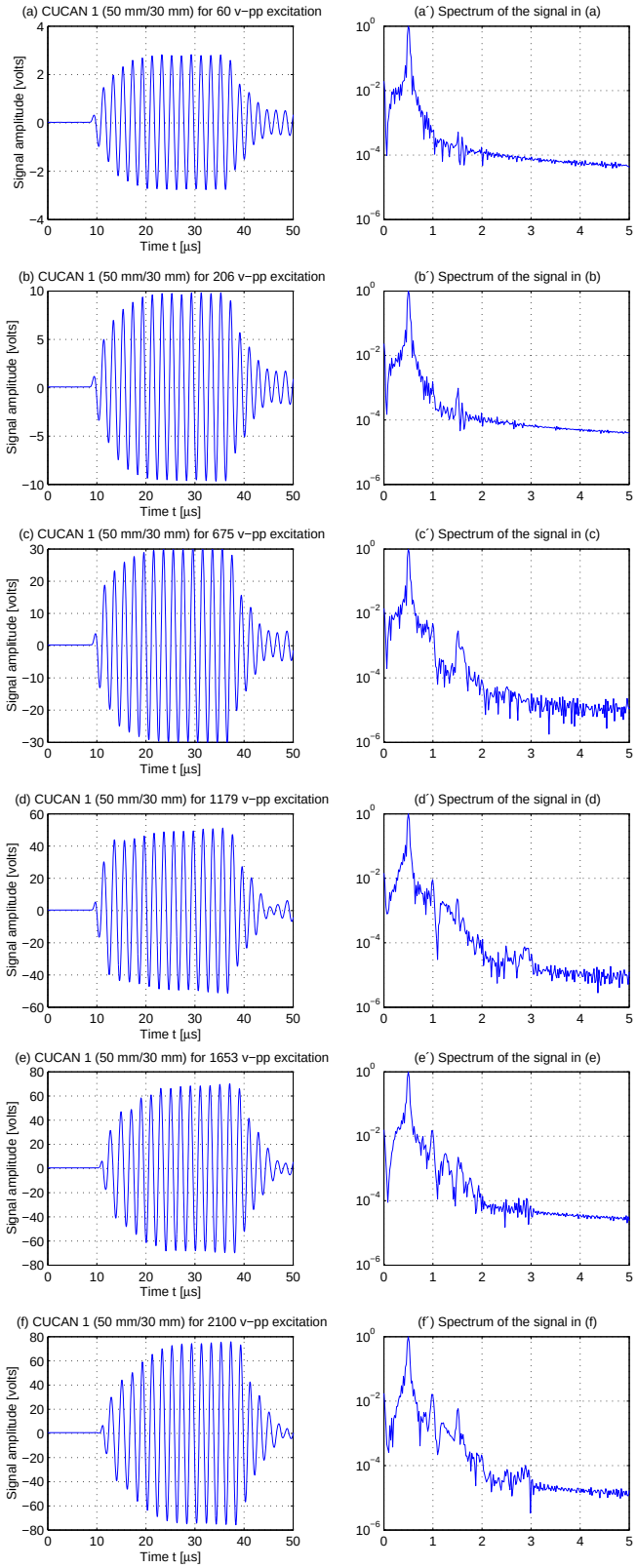

Figure 3.26: CUCAN 1 (50 mm/30 mm). (a), (b) its spectrum; (c) and (d) its spectrum; (e) and (f) its spectrum.

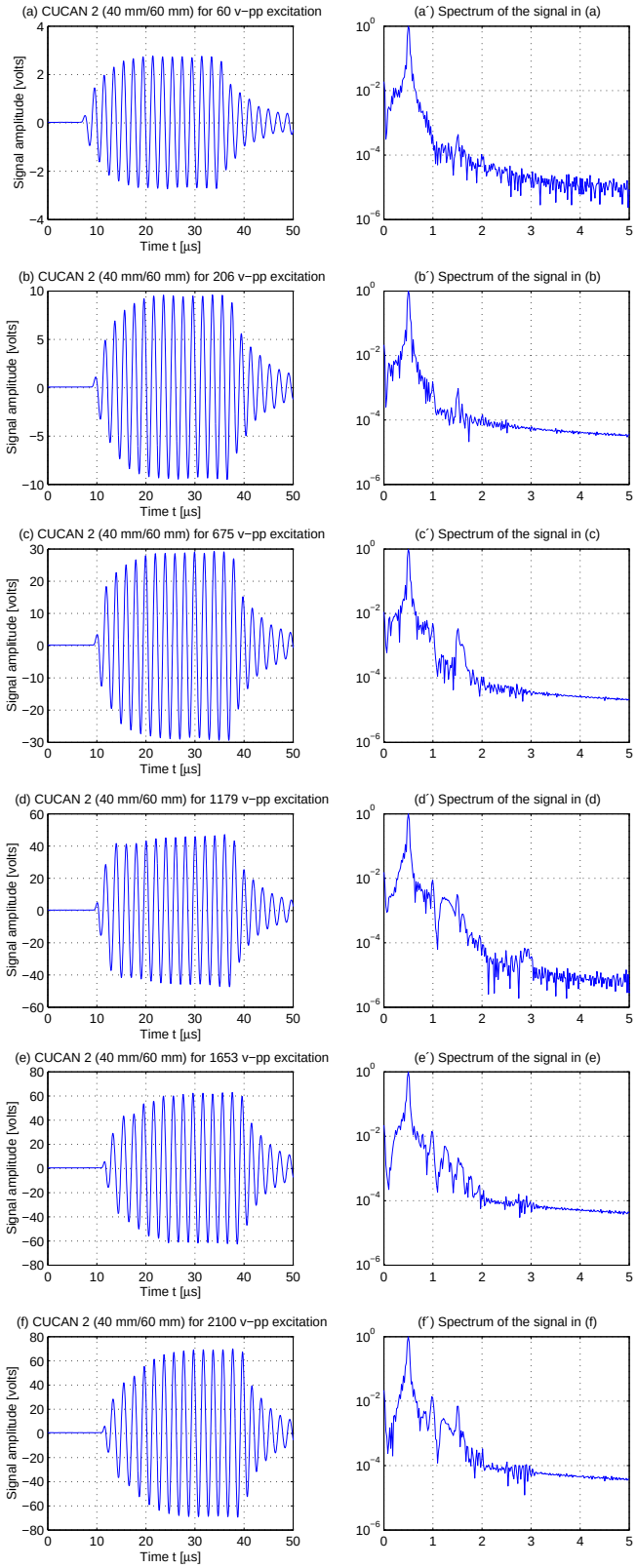

Figure 3.27: CUCAN 2 (40 mm/60 mm). (a), (b) its spectrum; (c) and (d) its spectrum; (e) and (f) its spectrum.

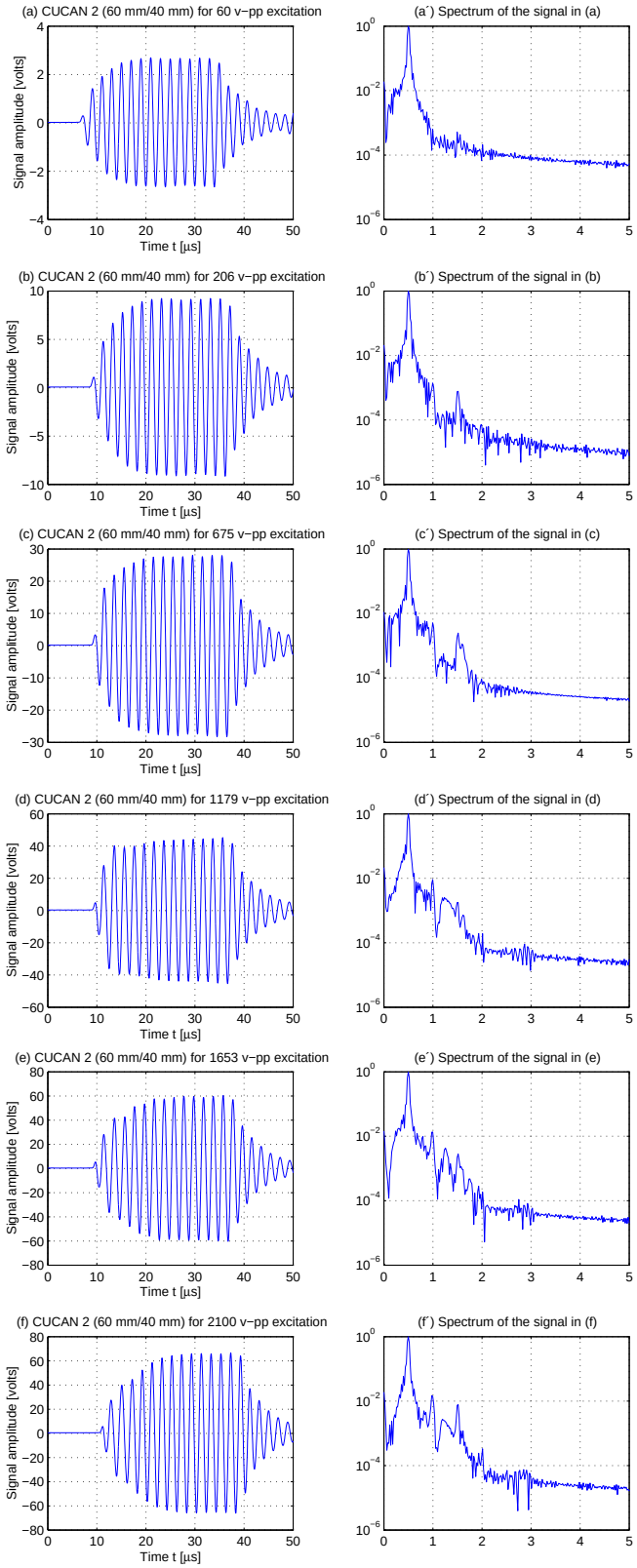

Figure 3.28: CUCAN 1 (60 mm/40 mm). (a), (b) its spectrum; (c) and (d) its spectrum; (e) and (f) its spectrum.

3.5 Discussions and conclusions

Nonlinear ultrasonics and its application for NDE of metals have been presented in the framework of both classical and non-classical nonlinearities. Fundamentals to both types of nonlinearities were discussed in some detail. Those included the influence of acoustic radiation and initial acoustic intensity from high-power transducers as well as the impact of relevant physical and acoustic parameters.

The discussion revealed that:

- for the detection of contact cracks a large particle displacement is needed able to excite the nonlinear vibrations of contact cracks and therefore a low frequency transducer (e.g., 500 kHz or lower) for a given acoustic radiation should be used for that purpose;
- for material harmonic imaging faster nonlinear distortion (harmonics growth) is desired, and in this case high frequency transducers (e.g., 5 MHz or higher for moderate attenuation) should be used; and
- the nonlinearity due to wave propagation encountered in copper materials (or those characterized by large sound velocity and density) will be much weaker that in water.

Nonlinear propagation of ultrasonic beams from an annular focused transducer has been investigated both experimentally and theoretically. The results have shown that:

- when performing harmonic imaging of solids in immersion, the effect from the water layer can be significant if the water layer is not thin enough;
- when using harmonics for the evaluation of nonlinear elastic properties (e.g., third-order elastic constants, nonlinearity parameter) of a solid in immersion setup, the influence of the harmonics generated in an immersing fluid must be taken into account;
- the best way to avoid the effect from water seems to be contact test configuration.

The stability of the simulation algorithm has also been investigated. It was found that such factors as, the step size Δz, the number of retained harmonics, attenuation, influence the algorithm convergence. The convergence can be improved by using a small propagation step Δz, at the price of a largely increased computation time. Thus, the development of the efficient simulation algorithms with fast convergence can still be an interesting topic in the future work.

A preliminary study concerning nonlinear ultrasonic detection of contact cracks has been conducted. The experimental setup has been built, and three different sets of copper samples bonded in three different ways have been inspected using nonlinear ultrasonics as well linear ultrasonics for comparison. A series of measurements have been made using the available copper samples but unfortunately, no CAN phenomena could be observed. This could be possibly explained by the fact that the available copper samples were inappropriate, that is, the samples inspected had either poor bonding (no contact between the parts) or a very good bonding ('welded'). Finding (or designing) copper samples that contain kissing bonds and contact cracks, and quantitative studying the CAN of kissing bonds will be of interest in the future work.

Bibliography

[1] Ultrasonics International'03. *http://www.ccmr.cornell.edu/˜ui03/ui03_schedule.html*. Granada, Spain, June 30 - July 3, 2003.

[2] The 5th World Congress on Ultrasonics. *http://www.sfa.asso.fr/wcu2003*. Paris, France, September 7-10, 2003.

[3] P P Delsanto. On the universality on nonclassical nonlinear phenomena and their classification. *Ultrasonics International'03*, Granada, Spain, June 30-July 3, 2003.

[4] D. Donskoy. Nonlinear vibro-ultrasonic technique for detection and characterization of cracks and other contact-type interfaces. *Ultrasonics International'03*, Granada, Spain, June 30-July 3, 2003.

[5] J. A. TenCate. Dynamic nonlinear ultrasonics at small strains. *Ultrasonics International'03*, Granada, Spain, June 30-July 3, 2003.

[6] Y. S. Wang. Non-linear acoustic interaction on a frictional contact interface between two anisotropic solids. *Ultrasonics International'03*, Granada, Spain, June 30-July 3, 2003.

[7] I. Yu. Solodov. Ultrasonics of nonlinear interfaces in solids: new physical aspects and nde applications. *Fifth World Congress on Ultrasonics*, Paris, France, September 7-10, 2003.

[8] V. Yu. Zaitsev. Acoustic wave-crack interaction: mechanisms of nonlinear elastic and inelastic dynamics at different time-scale. *Fifth World Congress on Ultrasonics*, Paris, France, September 7-10, 2003.

[9] A. Sutin, P. Johnson, and J. Tencate. Development of nonlinear time reverse acoustics (nltra) method for crack detection in solids. *Fifth World Congress on Ultrasonics*, Paris, France, September 7-10, 2003.

[10] C. Pecorari. Experimental investigation into nonlinear interaction of ultrasonic waves with surfaces in contact. *Fifth World Congress on Ultrasonics*, Paris, France, September 7-10, 2003.

[11] B. Castagnde, A. Moussatov, and V. Gusev. Challenge of ultrasonic self-induced hysteresis phenomenon in damaged materials. *Fifth World Congress on Ultrasonics*, Paris, France, September 7-10, 2003.

[12] C. Barrière. An alternative method for nonlinearity parameter measurments in solids. *Ultrasonics International'03*, Granada, Spain, June 30-July 3, 2003.

[13] A. M. Sutin. Application of nonlinear time reverse acoustics to isolate cracks in solids. *Ultrasonics International'03*, Granada, Spain, June 30-July 3, 2003.

[14] J. A. Turner. Measurements of third-order elastic constants of pmn electrostrictive ceramics. *Ultrasonics International'03*, Granada, Spain, June 30-July 3, 2003.

[15] M. Vila. Contact phase modulation method for acoustic nonlinear parameter measurement in solid. *Ultrasonics International'03*, Granada, Spain, June 30-July 3, 2003.

[16] N. Wang. Experimental investigations of elastic-plastic waves in copper. *Ultrasonics International'03*, Granada, Spain, June 30-July 3, 2003.

[17] T. Bateman, W. P. Mason, and H. J. McSkimin. Third-order elastic moduli of germanium. *J. Appl. Phys.*, 32(5):928–936, 1961.

[18] M. A. Breazeale and J. Ford. Ultrasonic studies of the nonlinear behavior of solids. *J. Appl. Phys.*, 36:3486–3490, 1965.

[19] W. B. Gauster and M. A. Breazeale. Ultrasonic measurement of the nonlinear parameters of copper single crystals. *Phys. Rev.*, 168(3):655–661, 1968.

[20] R. D. Peters, M. A. Breazeale, and J. Ford. Third harmonic of an initial sinusoidal ultrasonic wave in copper. *Appl. Phys. Letters*, 12(3):106–109, 1968.

[21] M. A. Breazeale and J. Ford. Ultrasonic studies of the nonlinear properties of solids. *Int J. Nondestr. Test.*, 4:149–166, 1972.

[22] M. A. Breazeale and J. Philip. Determination of third-order elastic constants from ultrasonic harmonic generation measurements. *Phys. Acoust.*, 17:1–60, 1984.

[23] P. B. Nagy. Excess nonlinearity in material containing microcracks. *Rev. Progr. QNDE*, 13:1987–1994, 1994.

[24] P. B. Nagy. Fatigue damage assessment by nonlinear ultrasonic material characterization. *Ultrasonics*, 36:375–381, 1998.

[25] K.-Y. Jhang and K.-C. Kim. Evaluation of material degradation using nonlinear acoustic effect. *Ultrasonics*, 37:39–44, 1999.

[26] K.-Y. Jhang. Application of nonlinear ultrasonics to the nde of material degradation. *IEEE Trans. Ultrason. Ferroelectr.Freq. Contr.*, 47(3):540–548, 2000.

[27] H. Hirose and J. D. Achenbach. Higher harmonics in the far field due to dynamic crack-face contacting. *J. Acoust. Soc. Am.*, 93(1):142–147, 1993.

[28] I. Yu. Solodov. Nonlinear nde using contact acoustic nonlinearity. *1994 IEEE Ultrason Symp.*, pages 1279–1283, 1994.

[29] I. Yu. Solodov. Ultrasonics of non-linear contacts: propagation, reflection and nde-applications. *Ultrasonics*, 36:383–390, 1998.

[30] R. G. Maev and I. Yu. Solodov. Acoustic reflectivity enhancement using higher-order nonlinear reflection mode. *1998 IEEE Ultrason Symp.*, pages 707–710, 1998.

[31] I. Yu. Solodov, N. Krone, and G. Busse. Can: an example of nonlclassical acoustic nonlinearity in solids. *Ultrasonics*, 40:621–625, 2002.

[32] V. Yu. Zaitsev, V. Gusev, and B. Castagnde. Observation of the "luxemburg-gorky effect" for elastic waves. *Ultrasonics*, 40:627–631, 2002.

[33] N. Krohn, R. Stoessel, and G. Busse. Acoustic non-linearity for defect selective imaging. *Ultrasonics*, 40:633–637, 2002.

[34] P. Wu, F. Lingvall, and T. Stepinski. Inspection of copper canisters for spent nuclear fuel by means of ultrasound - electron beam evaluation, harmonic imaging, materials characterization and ultrasonic modelling. Technical Report TR-00-23, SKB, 2000.

[35] P. Wu and T. Stepinski. Ultrasonic harmonic imaging in nondestructive evaluation: preliminary experimental study. *2000 IEEE Ultrason Symp.*, pages 801–804, 2000.

[36] T. Stepinski, F. Lingvall, and Ping Wu. Inspection of copper canisters for spent nuclear fuel by means of ultrasound - ultrasonic imaging of eb weld, theory of harmonic imaging of welds, and nde of cast iron. Technical Report TR-01-36, SKB, 2001.

[37] F. Lingvall, P. Wu, and T. Stepinski. Inspection of copper canisters for spent nuclear fuel by means of ultrasound - nonlinear acoustics, synthetic aperture imaging. Technical Report TR-03-05, SKB, 2003.

[38] P. T. Christopher and K. J. Parker. New approaches to nonlinear diffractive field propagation. *J. Acoust. Soc. Am.*, 90(1):488–499, 1991.

[39] D. H. Trivett and A. L. Van Buren. Propagation of plane, cylindrical, and spherical finite amplitude waves. *J. Acoust. Soc. Am.*, 69(4):943–949, 1981.

[40] M. F. Hamilton and D. T. Blackstock. *Nonlinear Acoustics*. Academic Press, San Diego, 1998.

[41] B. A. Korshak, I. Yu. Solodov, and E. M. Ballad. Dc-efects, sub-harmonics, stochasticity and memory for contact acoustic non-linearity. *Ultrasonics*, 40:707–713, 2002.

[42] T. Stepinski and Ping Wu. Inspection of copper canisters for spent nuclear fuel by means of ultrasonic array system. Technical Report Inkapsling Projektrapport 97-06, SKB, 1997.

Chapter 4

Synthetic Aperture Imaging

by Erik Wennerström

4.1 Introduction

4.1.1 SAI techniques

Synthetic aperture imaging (SAI) is an approach to restoration of ultrasonic B-scan images applied with the aim to remove the distortion introduced by the transducer used in the acquisition. There are several methods available to improve quality of ultrasonic images. All of these methods are based on different assumptions about the system concerning shape of the transducer and target, and distance between them.

One of the most widely used SAI techniques is the synthetic aperture focusing technique, SAFT, which represents a geometric approach to focusing. A point scatterer will give rise to a hyperbola in the B-scan [1] (cf. Figure 4.1(a)). The acquired image is processed with a spatial matched filter, shaped like the expected hyperbola obtained for a point transducer using for imaging a point reflector. SAFT, which is essentially a postprocessing technique, performs focusing in the reception but not in the transmission. As discussed further in Section 4.2 this approach is built on an idealized model of the transducer and scatterers in the measurement setup. For a more detailed description of the SAFT method, see [2, 3].

The phased array (PA) approach, which is applied in real-time affects the way the ultrasonic data is acquired. By delaying gathered signals from individual elements close to the center of the array more than signals from the edges, and then summing them up, the array is synthetically shaped to give a geometric focus at a specific distance from the transducer. Focusing is performed both in the transmission and reception.

4.1.2 Objectives

In earlier technical reports we have only considered point targets located at transducer's field. The purpose of this chapter is to evaluate the behavior of our SAI methods in the non-ideal conditions. The measurements presented here were made at several different distances from the transducer using both thin, flat targets of finite size as well as point targets.

The classical SAFT and phased array (PA) techniques are compared with the new method, presented in [4, 5]. The basic idea used in the new method is compensating the distortion introduced by the real not idealized measurement system. This includes smearing due to the transducer size and distances to targets, etc. Focusing is achieved by filtering the raw B-scan using a 2D Wiener filter, minimizing the mean squared error (MMSE) for the entire image to at least partly remove the distortion (see [2, 6] for details). As this method is built on less restrictive assumptions about the measurement system than SAFT, it is expected to perform better under the conditions investigated here.

In Section 4.2 some issues affecting the performance of the SAI-MMSE algorithms, such as, target size and its distance to transducer will be introduced. Their expected impact on the results will be discussed. Simulated results verifying the compared methods and their differences in performance are presented in Section 4.3. Finally, the experimental results for comparing the methods and conclusions are presented in Section 4.4.

4.2 Limitations of SAI methods

4.2.1 Flat reflectors

One of the issues addressed in this report is the effect of other reflectors than the point-scatterer. In SAFT, all acoustic waves sensed by the transducer are assumed to have a spherical wavefront

originating from a point reflector. Therefore, the source can be positioned at any point along a half circle, centered at the point where the echo appeared, see Figure 4.1(b). A point source will appear as a hyperbola in a B-scan image. The response of a wide, flat target of finite size,

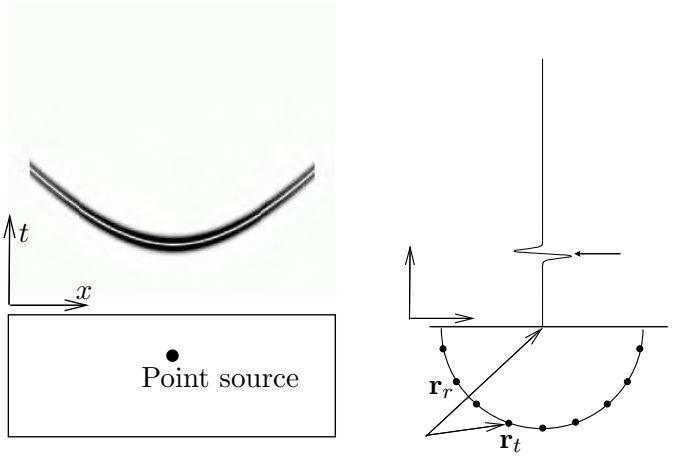

(a) B-scan from a point source

(b) Possible locations of source

Figure 4.1: Echoes from a point source.

such as a thin crack, will have different form in the B-scan. The echo amplitudes observed in individual A-scans in the B-scan acquired for a point target illuminated by a point source in the non-attenuating medium will decrease with the distance to the target R.

However, when the target is wider, the amount of reflected energy depends on its length and the angle relative to the transducer. Not all energy incident to the target will be reflected, some part will be transmitted into the material, converted to some other type of waves, for instance, surface waves, and reflected again at the edge of the target, see Figure 4.2. For a narrow target, this will happen instantly, but for a larger one this will result in several multiple echoes. Each of these echoes will give rise to a hyperbola in the B-scan.

For a very wide target, even wider than those used here, the response will be flat with hyperbolic sides.

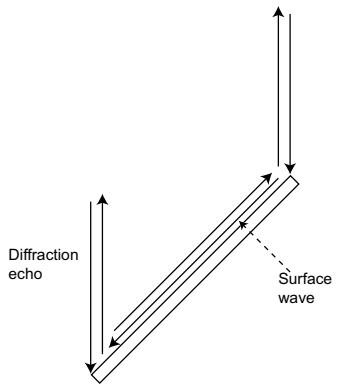

Figure 4.2: A non-point target results in several echoes.

For both SAFT and SAI-MMSE, the above mentioned changes in the collected B-scan will cause only minor problems. Recall that SAFT can be viewed as matching the idealized hyperbola

to the collected B-scan, see [2]. Even though the most energy is located at the center of the hyperbola, the most accurate match will be when the entire filter's hyperbola overlays the acquired one. When the filter's hyperbola only intersects the acquired hyperbola in few points, the output signal from the filter becomes quite low and forms artifacts in the processed image.

4.2.2 Transducer size and spatial impulse response

A more serious deviation from the assumed model occurs when the transducer is relatively large compared to the wavelength of the ultrasound. Then it will no longer emit spherical waves, and it will introduce spatial and temporal smearing in the reception.

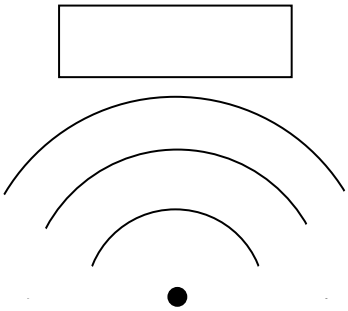

Figure 4.3: A spherical wave will be registered at different time instants at different points on a large transducer.

This can be easily understood if we note that a point-like transducer will sense all incoming acoustic energy from any wavefront at a single moment in time. Thus, its spatial impulse response (SIR) takes the form of Dirac pulse. A larger receiving transducer in its near field will register the wavefront's energy for a period of time, as the incoming wave arrives at the transducers surface over a period of time, see Figure 4.3. Its SIR will have a limited width, longer than the Dirac pulse, that will also depend on the location of the source at the plain in front of the transducer. In consequence the transducer will act as a low-pass filter on the gathered data, causing smearing. Transducer SIRs can be computed using various techniques, see [2] for more details.

The SAFT algorithm does not take real spatial impulse responses into account, and is therefore expected to yield severely reduced resolution for the finite sized transducers in the near field. The SAI-MMSE method is a solution to this problem; it takes the form of a linear spatial filter that uses the realistic SIRs to compensate for the transducer diffraction effects both in transmission and reception.

The other problem encountered for a large transducer is that it will radiate a narrow beam instead of a spherical wave. This means that its responses observed in the B-scan will also become narrower, since less angular information is available. The narrowed *shape* of the B-scan hyperbola will naturally result in a lower output from the matched filter in the SAFT algorithm.

4.2.3 Distance to the target

The distance from the transducer to the target will affect the shape of the received echo. Considering the shape of hyperbola in certain angle range for various distances between the target and the transducer, it can be easily seen that far away from the transducer the B-scan will be wider, but shorter in depth. Near to the transducer the B-scan will be narrower, and more convex, see Figure 4.4.

(a) B-scan shape close to transducer.

(b) B-scan shape far from transducer.

Figure 4.4: Shape of B-scans at different depth.

This change in the B-scan shape is easy to calculate and the matched filters in SAFT take different forms at different depths to account for that. Thus SAFT is capable of compensating for this effect at certain depth range. The SIR calculation in the SAI-MMSE also takes depth into account, resulting in the improved focus at all depths in the acquired image. The phased array approach (referred to as delay and sum processing (DAS)in 5), however, is focused at *one single depth*. The result is that the DAS method looses focus for all targets located outside its focal depth.

4.3 Simulated results

To illustrate the performance of synthetic aperture imaging, the following simulation was made. Two B-scans are simulated, one using a small transducer and another using a finite sized transducer. Both simulations are performed for a point target in water, at a distance of 190 mm from the transducer. The simulated B-scans are presented in Figure 4.5.

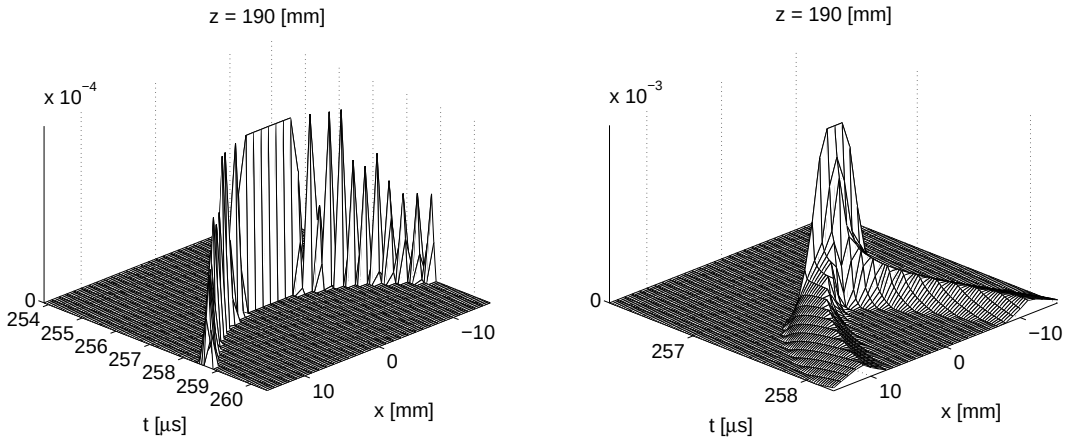

(a) B-scan, 1 mm transducer.

(b) B-scan, 8 mm transducer.

Figure 4.5: Simulated B-scans.

Both SAFT and MMSE were applied to the simulated measurement data. The results are presented in Figures 4.6 and 4.7.

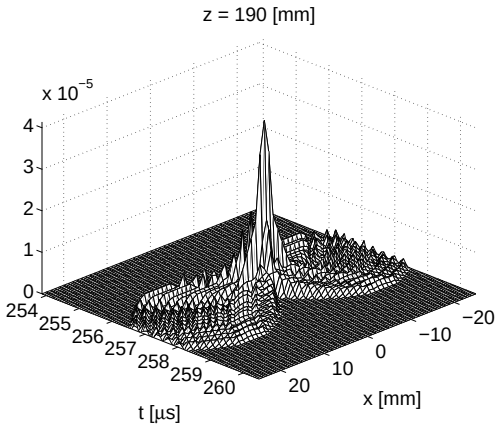

(a) B-scan after SAFT processing.

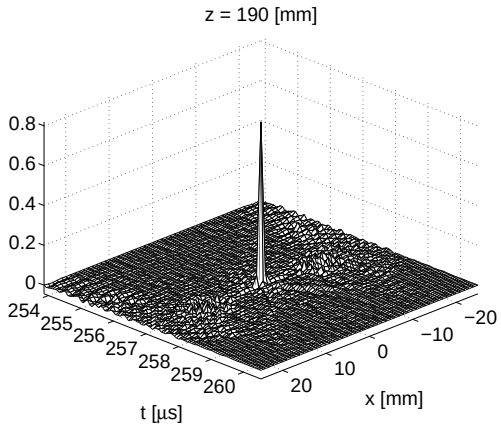

(b) B-scan after SAI-MMSE processing.

Figure 4.6: Processed simulated B-scans, 1 mm transducer.

After processing the B-scan data from the small transducer, the position of the scatterer can readily be found both for SAFT and SAI-MMSE algorithms. The artifacts at both sides of the peak in the SAFT image appear when the hyperbola in the measured data intersects with the matching hyperbola in the SAFT filter. As the hyperbolas do not overlap for more than a few elements at the intersection, the output from the matching filter will be small.

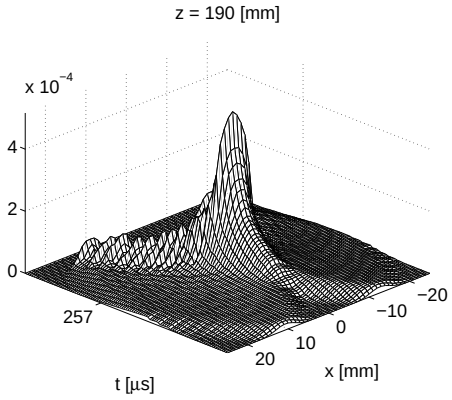

(a) B-scan after SAFT processing.

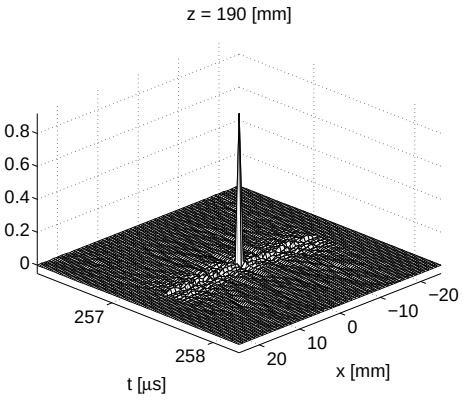

(b) B-scan after SAI-MMSE processing.

Figure 4.7: Processed simulated B-scans, 8 mm transducer.

The result obtained for the B-scan acquired from the large transducer is quite different, see Figure 4.7. In Figure 4.7(a) "walls" in front of the peak are present. They appear when the matching hyperbola of the SAFT method intersects with the *center* of the B-scan data. As most of the acquired energy is gathered in that region, the output form the matching filter will be significant. The SAI-MMSE method however, still produces a single, distinct peak. Only small artifacts in the form of thin line parallel to the x-axis at the base of the peak can be observed. Note however that these simulations are made in a noise-free environment, and for real data

better resolution of the SAI-MMSE will be obtained at the expense of an decreased signal to noise ratio (SNR). See section 4.4 for more details on measured data.

4.4 Measurements

4.4.1 Flat targets

The objective of the measurements presented here was to investigate the resolution of the SAFT and the SAI-MMSE methods for flat targets. The following standard assumptions are normally made concerning the system: first, it is assumed that the targets are point sources, and that there is no secondary scattering. In addition, the SAFT algorithm makes the assumption that the transducer is a point source, emitting spherical waves.

In these experiments the performance of the the two algorithms were evaluated in circumstances that deviated from the ideal assumptions. The targets were flat and some were large compared to a point source. The size of the transducer was varied from close to point source, to as large as our equipment allows. See below for details.

To investigate the impact of the size of the transducer the ALLIN array system was used. A variable number of 1 mm wide array elements was used. All elements were fired simultaneously, to simulate a planar (non focused) transducer. The number of elements used was 1,2,4,8,16 and 32.

The targets used in this experiment were flat sheets of 0.3 mm thick steel. Three different targets were used, with widths $L =$, 3, 5 and 7 mm, respectively. In addition the targets were rotated to be at an angle φ of 0°, 45° and 90° to the transducer plane. All measurements were performed with the targets submersed in water, at a distance of 190mm from the array as shown in Figure 4.8.

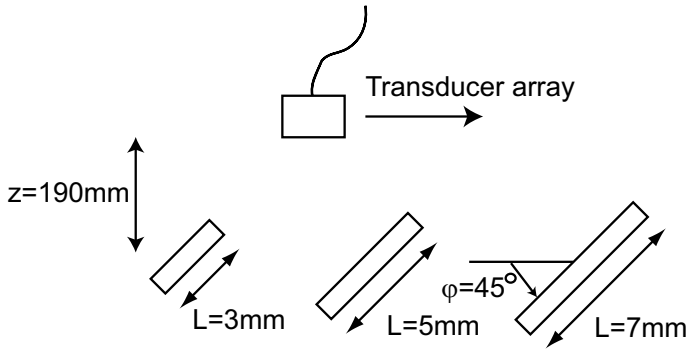

Figure 4.8: Measurement setup. Three flat targets in water, rotated in three different position. Note that the array is not to scale, it is in reality much larger.

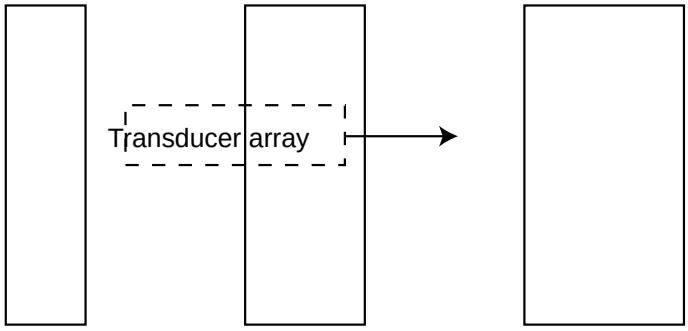

Figure 4.9: Measurement setup. Top view. Note that the array is not to scale, it is in reality much larger.

The B-scan data was acquired using ALLIN's mechanical scanner, with a spatial sampling distance of 1 mm between individual A-scans as shown in Figure 4.9.

4.4.2 Distance to target

These measurements were done to investigate the effect the distance to the target has on the DAS, SAFT and SAI-MMSE methods. A target in the form of two thin wires, 0.3 mm in diameter, spaced 2 mm apart was used. A B-scan was acquired by moving the transducer in a path perpendicular to the wires, that were held horizontally and submersed in water.

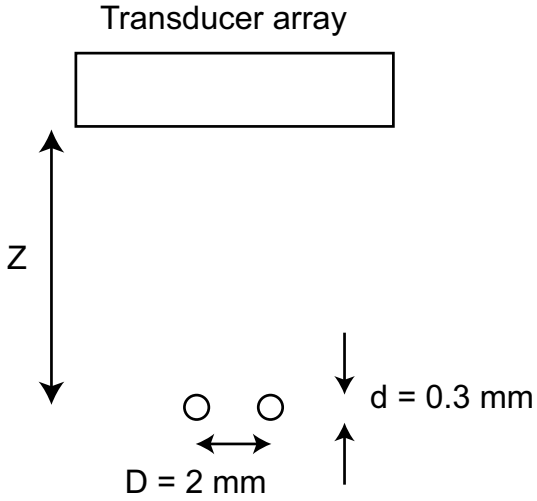

Figure 4.10: Measurement setup. Two closely spaced wires in water. The depths used were 60, 90 and 120 mm

The measurements were performed using a 32 mm array, focused at 90 mm for DAS imaging, and using one array element only for SAFT and SAI-MMSE processing. The measurements were repeated at three different depths: 60, 90 and 120 mm. Thus, the center distance agreed with the focal depth of the focused array, while the others differed with 30 mm from it. For all these experiments the spatial sampling step was 0.5 mm.

4.5 Results

4.5.1 Flat targets

A summary of the results is presented in Figures 4.11 and 4.12. Figure 4.11 shows the results obtained for the smallest of the targets, $L = 3mm$ positioned at the angle of $\varphi = 90°$. This target represents a small target to the transducer, and as all the assumptions listed in Section 4.4 are fulfilled; it provides a good comparison of the effect of different transducer sizes. The next Figure (Figure 4.12) shows selected results obtained for the largest of the targets, $L = 7mm$ at $\varphi = 0°$. It provides an insight to how the size of the target impacts on the performance of the methods. For a full presentation of all the data acquired in the measurements, see Appendix 4.6. Each row of the figures is composed of four subfigures. The first column shows the original, unprocessed image, the next two show the same image processed with SAFT and SAI-MMSE, respectively. The last column is a "profile" plot, showing the maximum value of each A-scan, fully rectified and normalized to have a maximum of unity. The profile of the original B-scan is shown in green, the profile after SAFT processing in blue and after SAI-MMSE processing in red. From the profile plots the width of the resulting echo obtained for each defect can easily be seen. It is also interesting to see where the noise floor of the data is located.

From the results in Figure 4.11 it can be seen that the SAI-MMSE method, compared to SAFT, provides equally sharp or sharper, focused images. With smaller transducer sizes, the difference is not very clear, as the SAFT method is also capable of resolving the image properly. With larger transducer size, 16 and 32 mm, the SAFT algorithm looses focus, and fails to improve the image at all.

The results in Figure 4.12 show that the size of the target has quite a small effect on either of the algorithms. For the transducer sizes where SAFT manages to sharpen the image of the small target, it also handles the larger targets.

Note that even though the SAI-MMSE filter uses the information about spatial impulse responses for different elements of the transducer the resolution drops somewhat with increasing transducer size. This is not surprising, as the data that contains most information are the A-scans close to the edges of the defect. With a larger surface of the transducer, its beam will be narrower and there will be fewer such A-scans.

The increased resolution in the SAI-MMSE method, however, comes at the cost of a lower signal to noise ratio than SAFT. This can be seen in the profile plots in Figure 4.11. (Note how the data outside the main peak contains more high frequent noise in the SAI-MMSE plot, the SAFT plot is lower and smoother.)

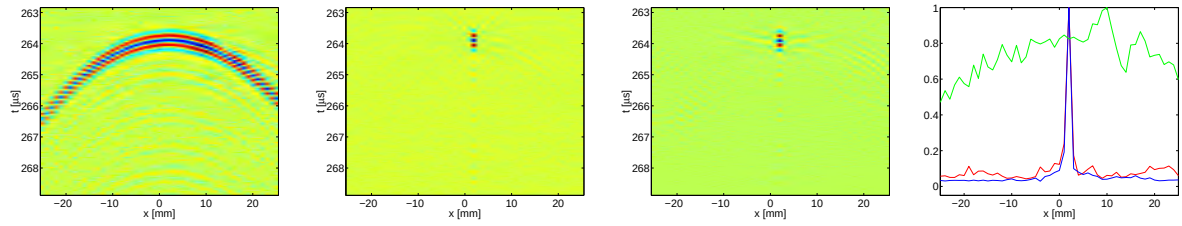

(a) Original B-scan (b) B-scan, SAFT (c) B-scan, MMSE (d) Profiles

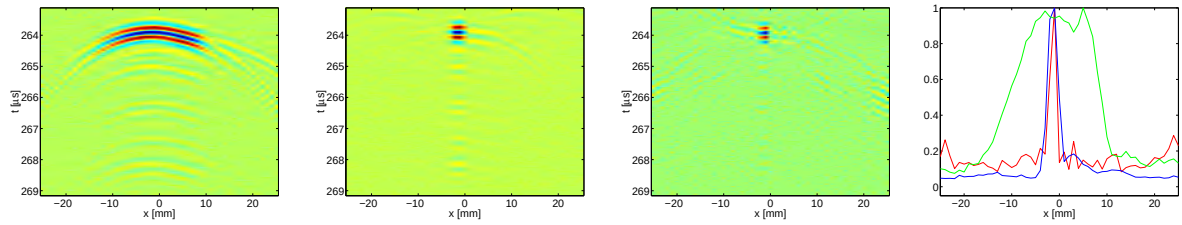

(e) Original B-scan (f) B-scan, SAFT (g) B-scan, MMSE (h) Profiles

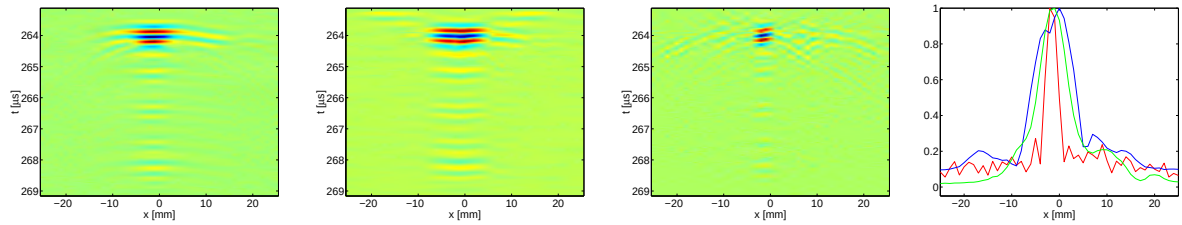

(i) Original B-scan (j) B-scan, SAFT (k) B-scan, MMSE (l) Profiles

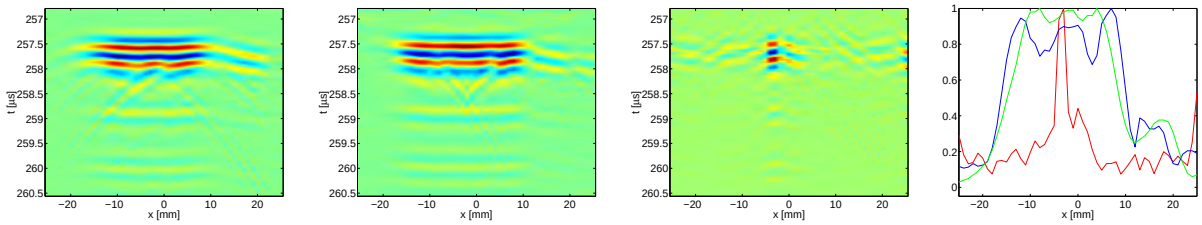

(m) Original B-scan (n) B-scan, SAFT (o) B-scan, MMSE (p) Profiles

Figure 4.11: Summary of results. Target width: 3mm, target angle: 90°. Top row: 1 mm wide transducer. Second row: 4 mm transducer. Third row: 16 mm transducer. Fourth row: 32 mm transducer. Green profile: Original data. Blue profile: SAFT processed data. Red profile: SAI-MMSE processed data.

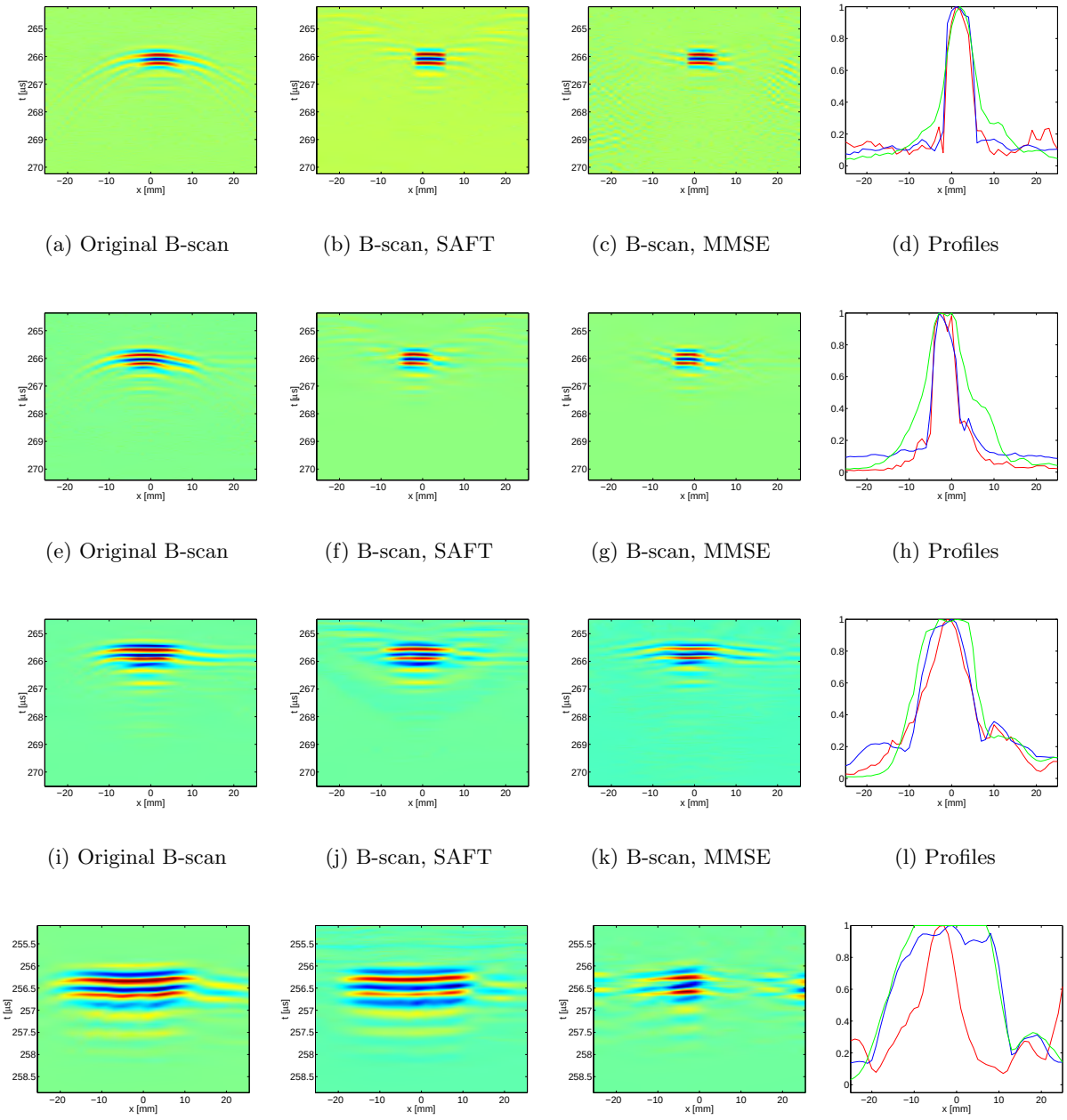

(a) Original B-scan (b) B-scan, SAFT (c) B-scan, MMSE (d) Profiles

(e) Original B-scan (f) B-scan, SAFT (g) B-scan, MMSE (h) Profiles

(i) Original B-scan (j) B-scan, SAFT (k) B-scan, MMSE (l) Profiles

(m) Original B-scan (n) B-scan, SAFT (o) B-scan, MMSE (p) Profiles

Figure 4.12: Summary of results. Target width: 7mm, target angle: 0°. Top row: 1 mm wide transducer. Second row: 4 mm transducer. Third row: 16 mm transducer. Fourth row: 32 mm transducer. Green profile: Original data. Blue profile: SAFT processed data. Red profile: SAI-MMSE processed data.

4.5.2 Distance to the target

The results for these measurements are presented in Figures 4.13 through 4.15. It can be seen that the B-scan from the phased array shows two distinctly separated targets for $z = 90\ mm$ (center row). When the targets are out of focus at $z = 60\ mm$ (top row) and $z = 120\ mm$ (bottom row) DAS is no longer capable of separating the wires. This illustrates clearly the

limitation of the DAS approach, a very narrow focal zone can be obtained using a single focus depth. Both SAFT and SAI-MMSE are capable of compensating for this. Also, with the targets closer to the transducer, the 2 mm between them results in a larger angular difference. Therefore it should be easier to separate the targets when they are closer to the transducer. As seen in Figure 4.13, SAFT and SAI-MMSE yield similar performance for this small 1 mm transducer. The change in distance creates no particular problem, and each of the algorithms can resolve the targets at all three depths.

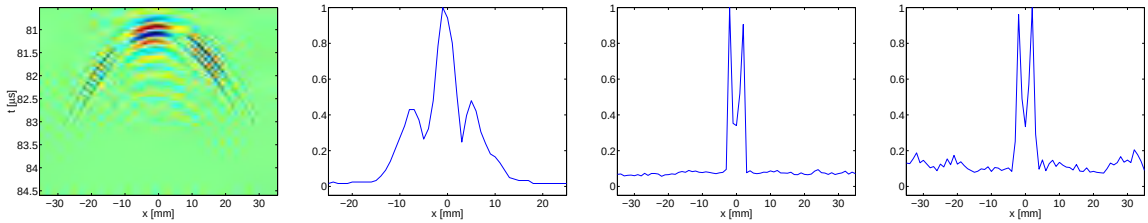

(a) Original B-scan (b) PA (c) SAFT (d) MMSE

Figure 4.13: Targets 2mm apart, $z = 60mm$. The data in the PA method were acquired using 32 elements focused at 90mm. The data used for SAFT and MMSE processing were acquired using 1 element.

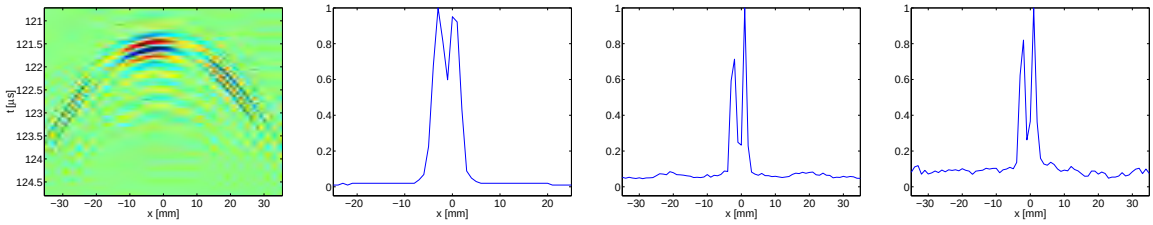

(a) Original B-scan (b) PA (c) SAFT (d) MMSE

Figure 4.14: Targets 2mm apart, $z = 90mm$. The data in the PA method were acquired using 32 elements focused at 90mm. The data used for SAFT and MMSE processing were acquired using 1 element.

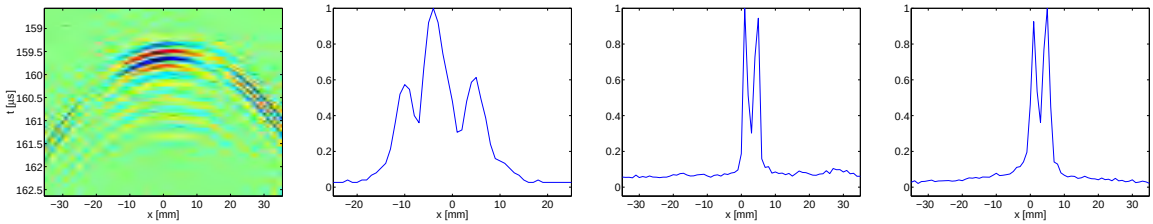

(a) Original B-scan (b) PA (c) SAFT (d) MMSE

Figure 4.15: Targets 2mm apart, $z = 120mm$. The data in the PA method were acquired using 32 elements focused at 90mm. The data used for SAFT and MMSE processing were acquired using 1 element.

4.6 Discussion

We have evaluated the resolution and ability to adapt to different environments of our recently proposed algorithm for synthetic aperture imaging (SAI-MMSE) in comparison with classical phased array imaging (DAS) and SAFT. The evaluation was done in non-ideal conditions where the system setup, such as transducer and target size, differs from what is assumed in the algorithms.

We have shown that the new SAI-MMSE algorithm is superior compared to SAFT and DAS imaging for small targets immersed in water. It is more resilient to changes in the equipment used and targets measured, and maintains a high resolution despite changes in the test setup. The approach in the SAI-MMSE algorithm differs from the other methods mentioned here, as it takes the diffraction introduced into the measured data by all parts of the system into account, and applies a 2D filter based on a minimum mean square error approach to compensate for this diffraction. As long as the spatial impulse response (SIR) of the transducer used can be calculated or measured this maximizes the resolution of the recreated image for any given noise level.

Bibliography

[1] J. Krautkramer and H. Krautkramer. *Ultrasonic Testing of Materials*. Springer Verlag, Berlin and New York, 1983.

[2] T. Stepinski, F. Lingvall, and P. Wu. Inspection of copper canisters for spent nuclear fuel by means of ultrasound. Technical report, SKB, 2002.

[3] J.A. Seydel. *Ultrasonic Synthetic-aperture Focusing Techniques in NDT*. Research Techniques for Nondestructive Testing. Academic Press, 1982.

[4] T. Stepinski, F. Lingvall, and P. Wu. Inspection of copper canisters for spent nuclear fuel by means of ultrasound — ultrasonic imaging of eb weld, theory of harmonic imaging of welds, and nde of cast iron. Technical Report TR-01-36, SKB, 2001.

[5] F. Lingvall, T. Olofsson, and T. Stepinski. Synthetic aperture imaging using sources with finite aperture: Deconvolution of the spatial impulse response. *Accepted to J. Acoust. Soc. Am.*, 2003.

[6] F. Lingvall, T. Olofsson, and T. Stepinski. Synthetic aperture imaging using sources with finite aperture: Deconvolution of the spatial impulse response. *J. Acoust. Soc. Am.*, 114(1):225–234, July 2003.

4.A Results of SAI

4.A.1 Results: 1 mm transducer

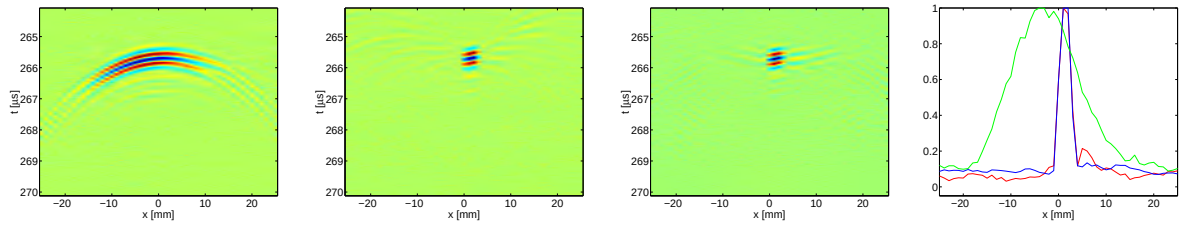

(a) Original B-scan (b) B-scan, SAFT (c) B-scan, MMSE (d) Profiles

Figure 4.16: Target width= $3mm$, target angle= $0°$.

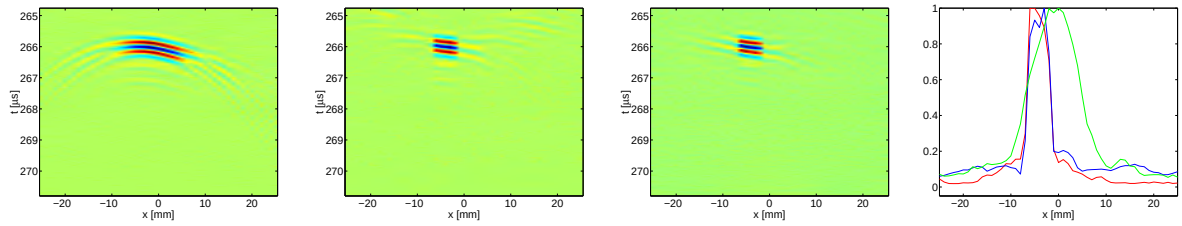

(a) Original B-scan (b) B-scan, SAFT (c) B-scan, MMSE (d) Profiles

Figure 4.17: Target width= $5mm$, target angle= $0°$.

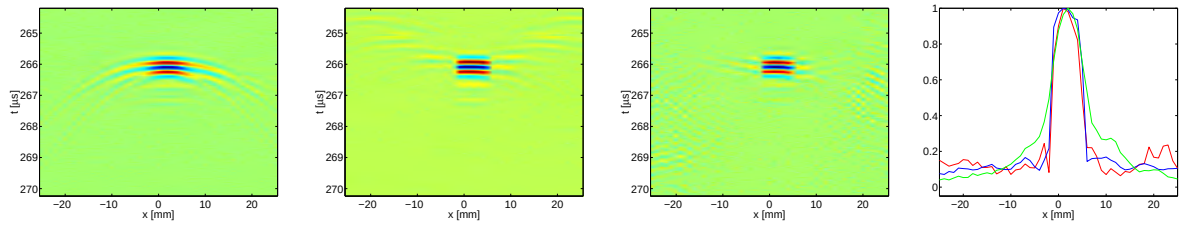

(a) Original B-scan (b) B-scan, SAFT (c) B-scan, MMSE (d) Profiles

Figure 4.18: Target width= $7mm$, target angle= $0°$.

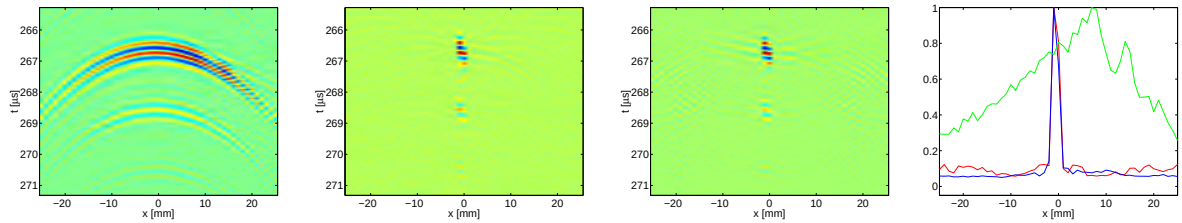

(a) Original B-scan (b) B-scan, SAFT (c) B-scan, MMSE (d) Profiles

Figure 4.19: Target width= $3mm$, target angle= $45°$.

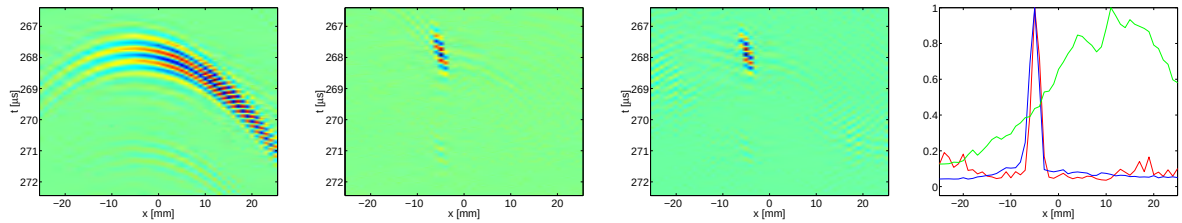

(a) Original B-scan (b) B-scan, SAFT (c) B-scan, MMSE (d) Profiles

Figure 4.20: Target width= $5mm$, target angle= $45°$.

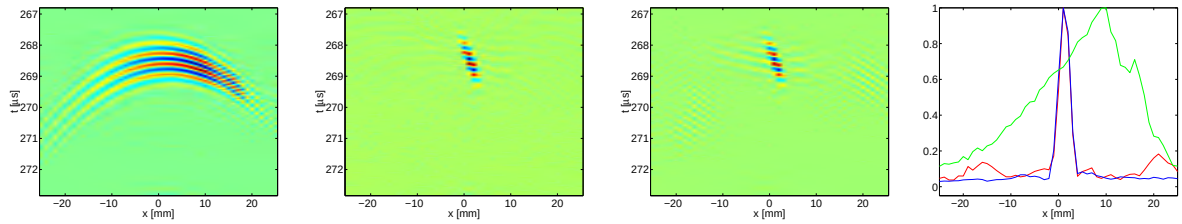

(a) Original B-scan (b) B-scan, SAFT (c) B-scan, MMSE (d) Profiles

Figure 4.21: Target width= $7mm$, target angle= $45°$.

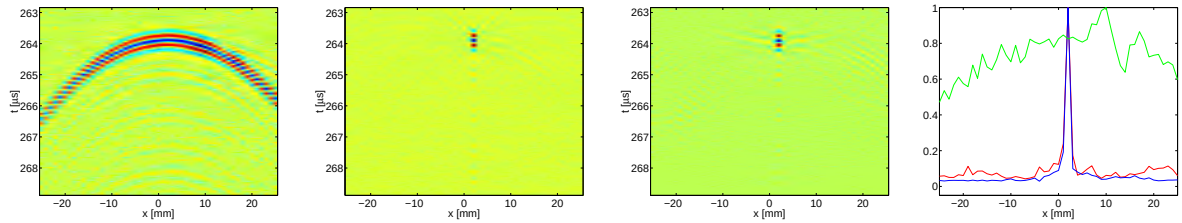

(a) Original B-scan (b) B-scan, SAFT (c) B-scan, MMSE (d) Profiles

Figure 4.22: Target width= $3mm$, target angle= $90°$.

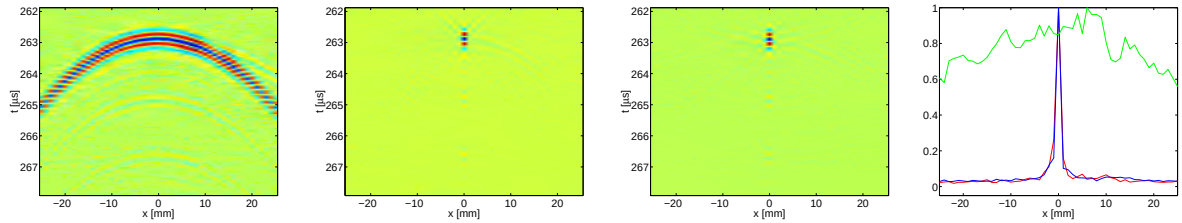

(a) Original B-scan (b) B-scan, SAFT (c) B-scan, MMSE (d) Profiles

Figure 4.23: Target width= $5mm$, target angle= $90°$.

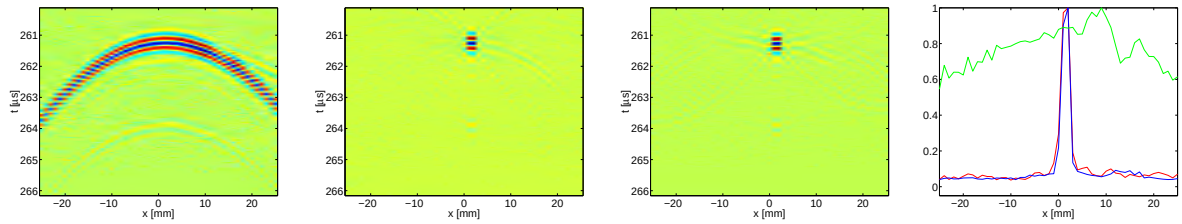

(a) Original B-scan (b) B-scan, SAFT (c) B-scan, MMSE (d) Profiles

Figure 4.24: Target width= $7mm$, target angle= $90°$.

4.A.2 Results: 2 mm transducer

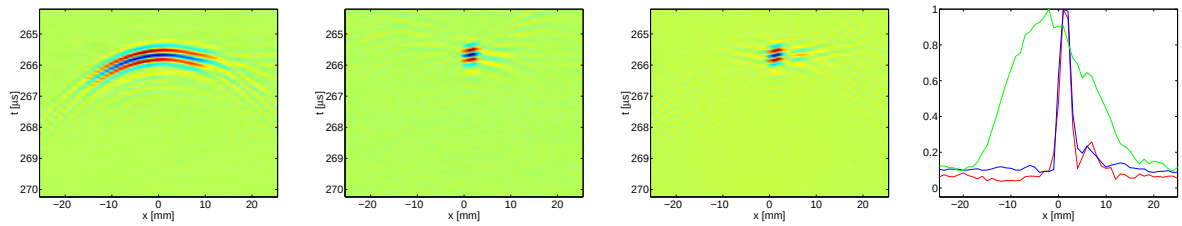

(a) Original B-scan (b) B-scan, SAFT (c) B-scan, MMSE (d) Profiles

Figure 4.25: Target width= $3mm$, target angle= $0°$.

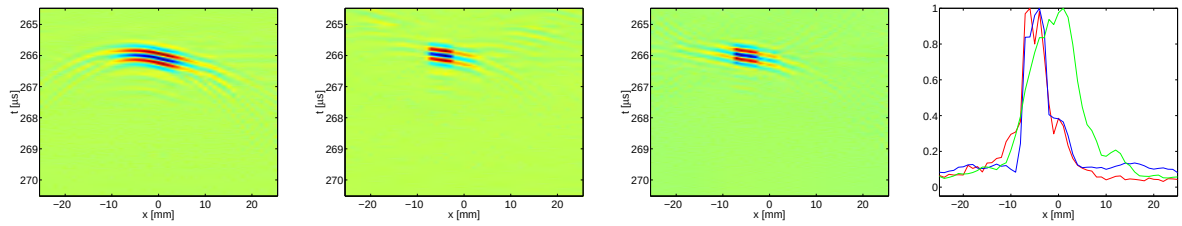

(a) Original B-scan (b) B-scan, SAFT (c) B-scan, MMSE (d) Profiles

Figure 4.26: Target width= $5mm$, target angle= $0°$.

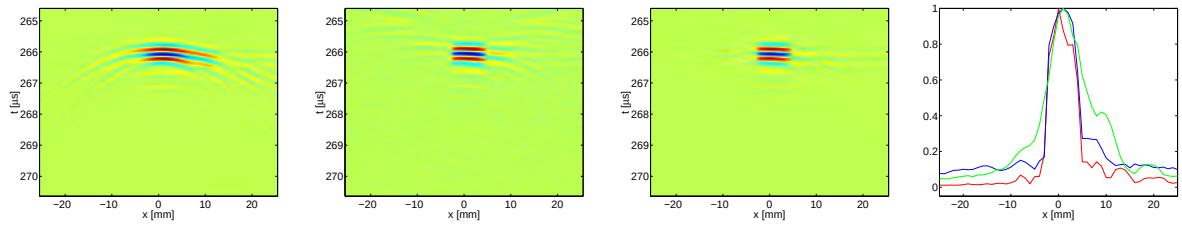

(a) Original B-scan (b) B-scan, SAFT (c) B-scan, MMSE (d) Profiles

Figure 4.27: Target width= $7mm$, target angle= $0°$.

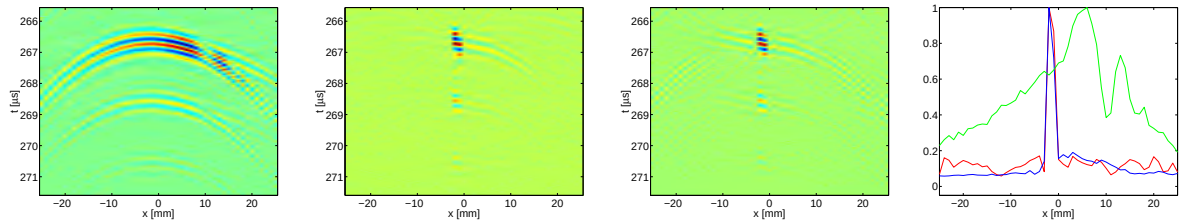

(a) Original B-scan (b) B-scan, SAFT (c) B-scan, MMSE (d) Profiles

Figure 4.28: Target width= $3mm$, target angle= $45°$.

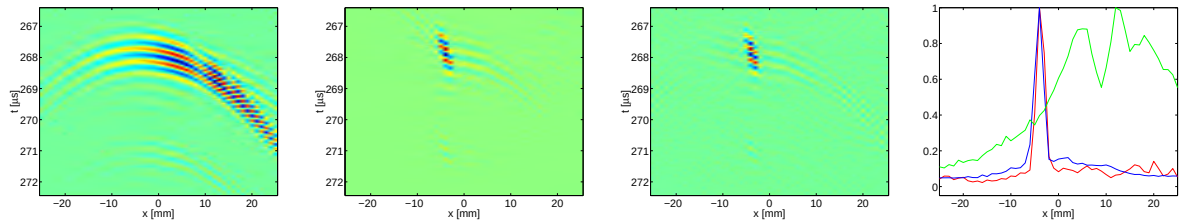

(a) Original B-scan (b) B-scan, SAFT (c) B-scan, MMSE (d) Profiles

Figure 4.29: Target width= $5mm$, target angle= $45°$.

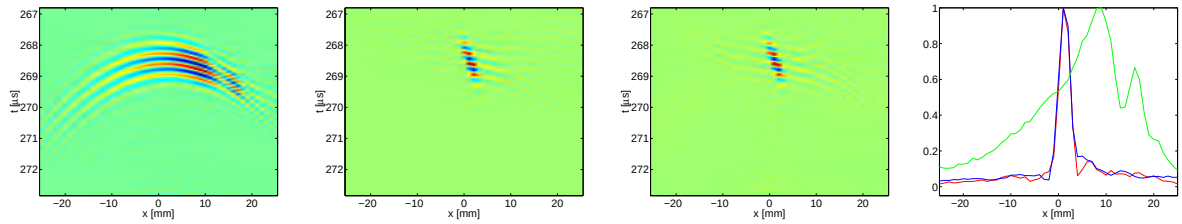

(a) Original B-scan (b) B-scan, SAFT (c) B-scan, MMSE (d) Profiles

Figure 4.30: Target width= $7mm$, target angle= $45°$.

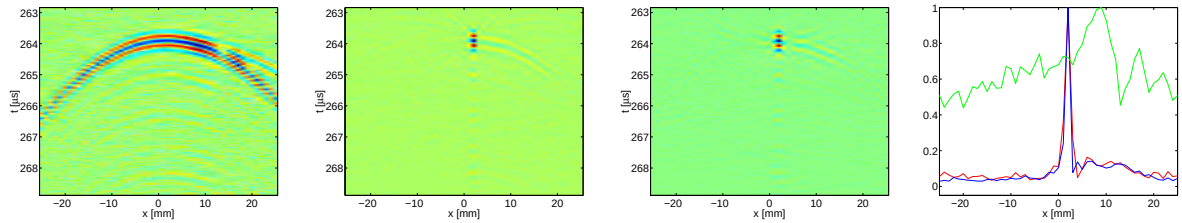

(a) Original B-scan (b) B-scan, SAFT (c) B-scan, MMSE (d) Profiles

Figure 4.31: Target width= $3mm$, target angle= $90°$.

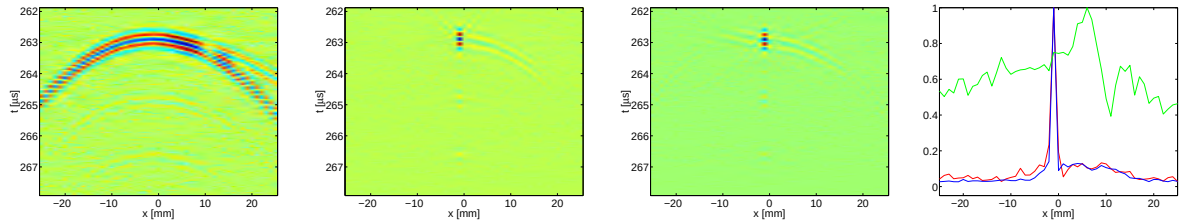

(a) Original B-scan (b) B-scan, SAFT (c) B-scan, MMSE (d) Profiles

Figure 4.32: Target width= $5mm$, target angle= $90°$.

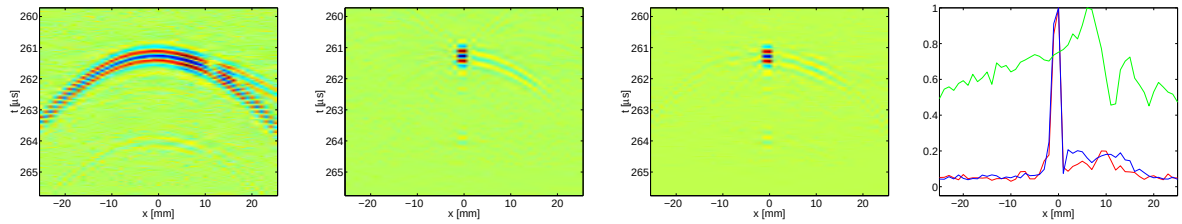

(a) Original B-scan (b) B-scan, SAFT (c) B-scan, MMSE (d) Profiles

Figure 4.33: Target width= $7mm$, target angle= $90°$.

4.A.3 Results: 4 mm transducer

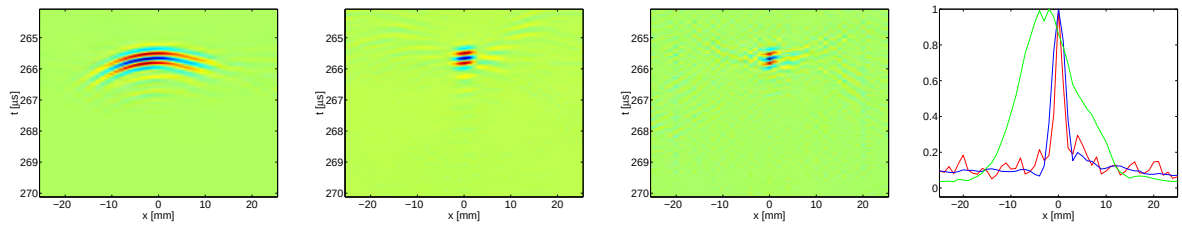

(a) Original B-scan (b) B-scan, SAFT (c) B-scan, MMSE (d) Profiles

Figure 4.34: Target width= $3mm$, target angle= $0°$.

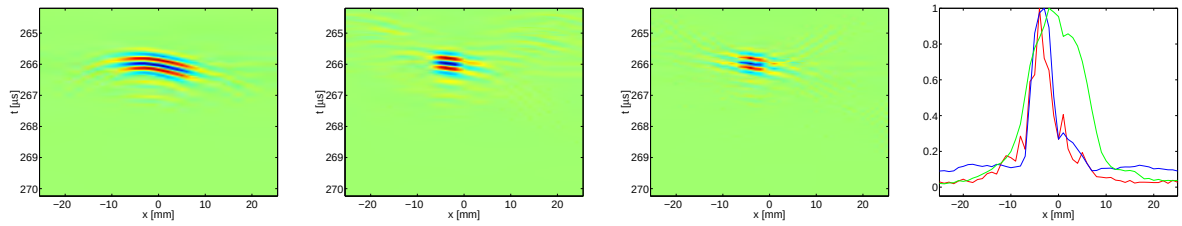

(a) Original B-scan (b) B-scan, SAFT (c) B-scan, MMSE (d) Profiles

Figure 4.35: Target width= $5mm$, target angle= $0°$.

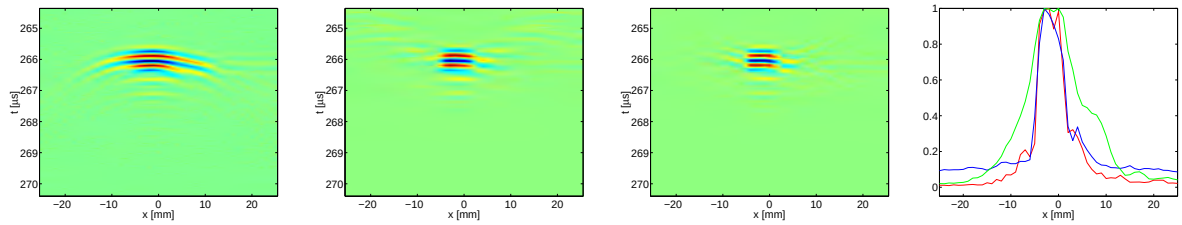

(a) Original B-scan (b) B-scan, SAFT (c) B-scan, MMSE (d) Profiles

Figure 4.36: Target width= $7mm$, target angle= $0°$.

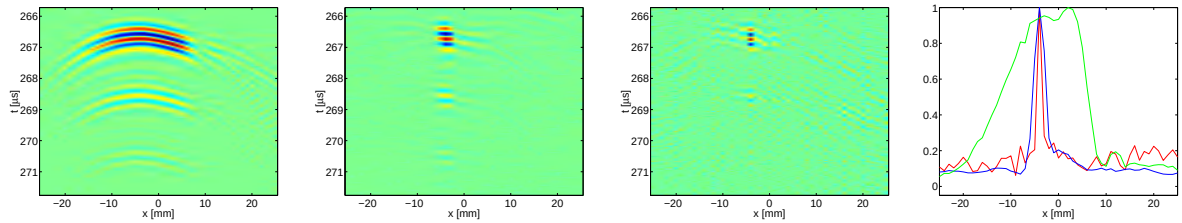

(a) Original B-scan (b) B-scan, SAFT (c) B-scan, MMSE (d) Profiles

Figure 4.37: Target width= $3mm$, target angle= $45°$.

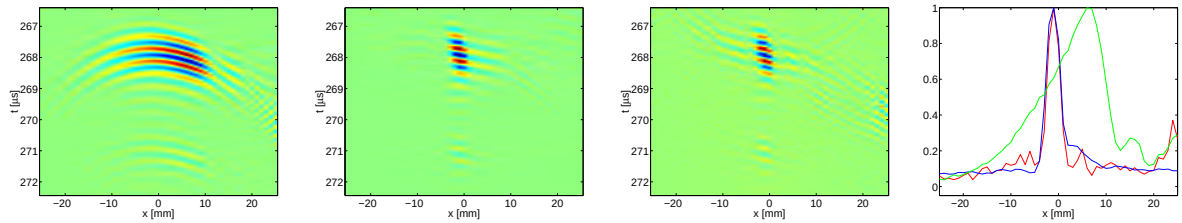

(a) Original B-scan (b) B-scan, SAFT (c) B-scan, MMSE (d) Profiles

Figure 4.38: Target width= $5mm$, target angle= $45°$.

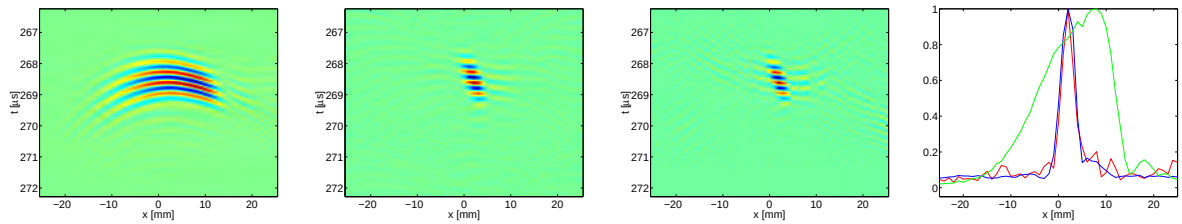

(a) Original B-scan (b) B-scan, SAFT (c) B-scan, MMSE (d) Profiles

Figure 4.39: Target width= $7mm$, target angle= $45°$.

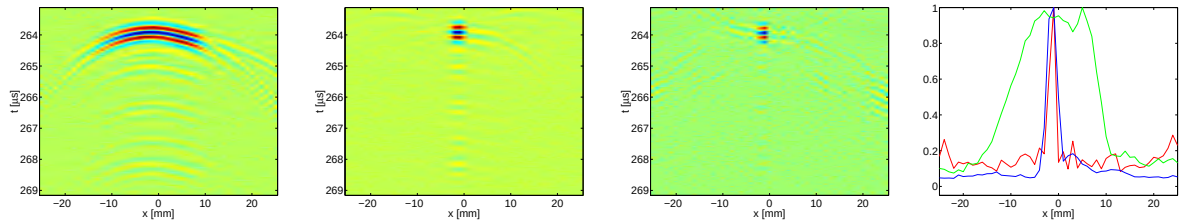

(a) Original B-scan (b) B-scan, SAFT (c) B-scan, MMSE (d) Profiles

Figure 4.40: Target width= $3mm$, target angle= $90°$.

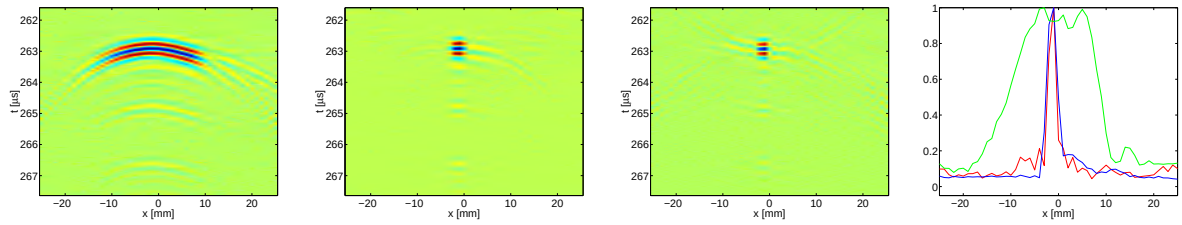

(a) Original B-scan (b) B-scan, SAFT (c) B-scan, MMSE (d) Profiles

Figure 4.41: Target width= $5mm$, target angle= $90°$.

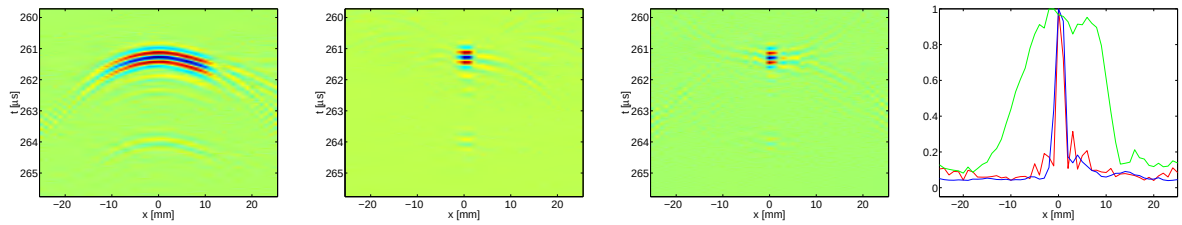

(a) Original B-scan (b) B-scan, SAFT (c) B-scan, MMSE (d) Profiles

Figure 4.42: Target width= $7mm$, target angle= $90°$.

4.A.4 Results: 8 mm transducer

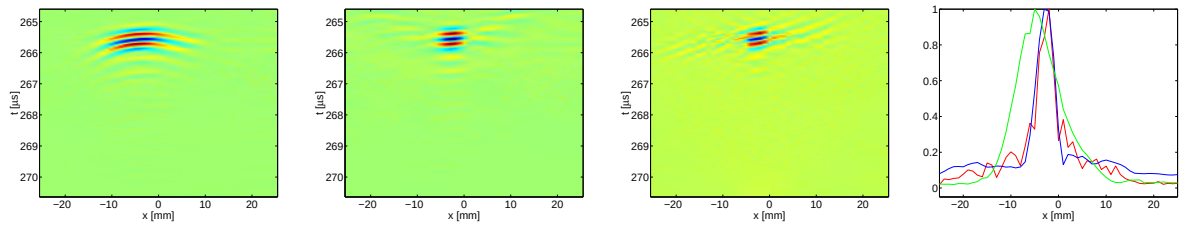

(a) Original B-scan (b) B-scan, SAFT (c) B-scan, MMSE (d) Profiles

Figure 4.43: Target width= $3mm$, target angle= $0°$.

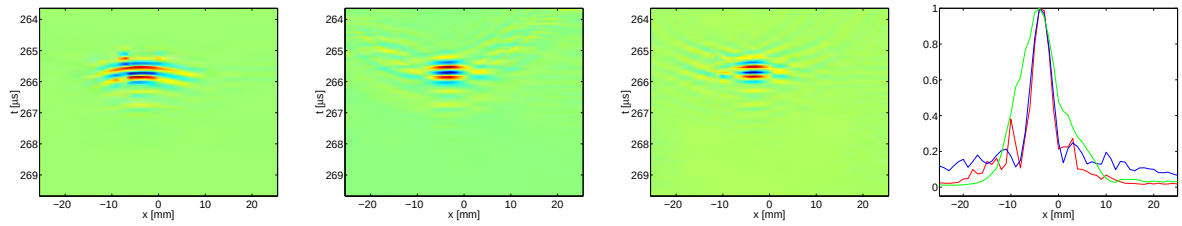

(a) Original B-scan (b) B-scan, SAFT (c) B-scan, MMSE (d) Profiles

Figure 4.44: Target width= $5mm$, target angle= $0°$.

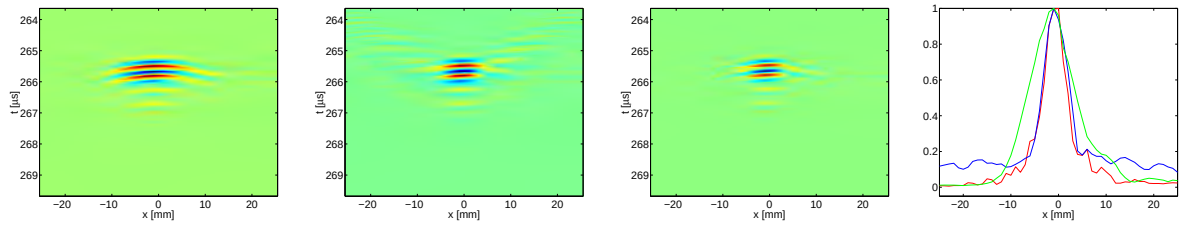

(a) Original B-scan (b) B-scan, SAFT (c) B-scan, MMSE (d) Profiles

Figure 4.45: Target width= $7mm$, target angle= $0°$.

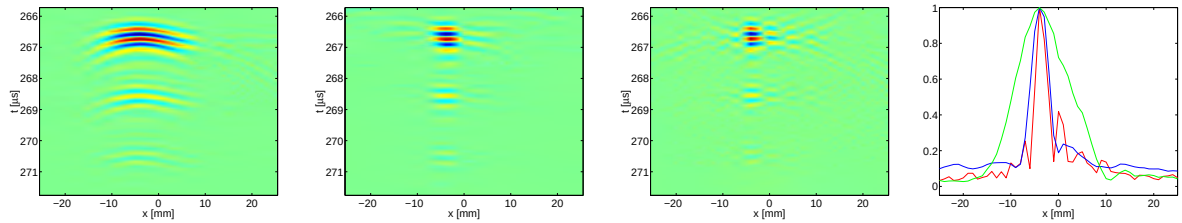

(a) Original B-scan (b) B-scan, SAFT (c) B-scan, MMSE (d) Profiles

Figure 4.46: Target width= $3mm$, target angle= $45°$.

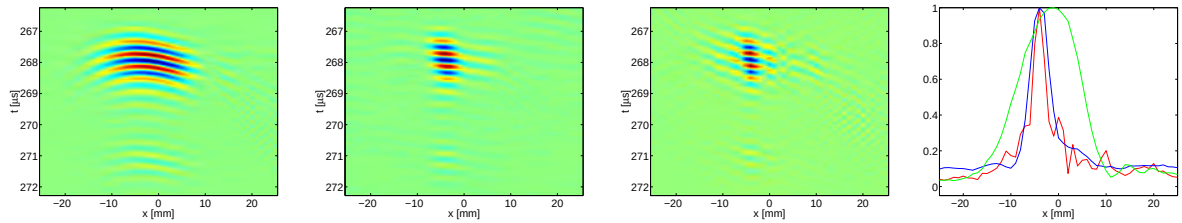

(a) Original B-scan (b) B-scan, SAFT (c) B-scan, MMSE (d) Profiles

Figure 4.47: Target width= $5mm$, target angle= $45°$.

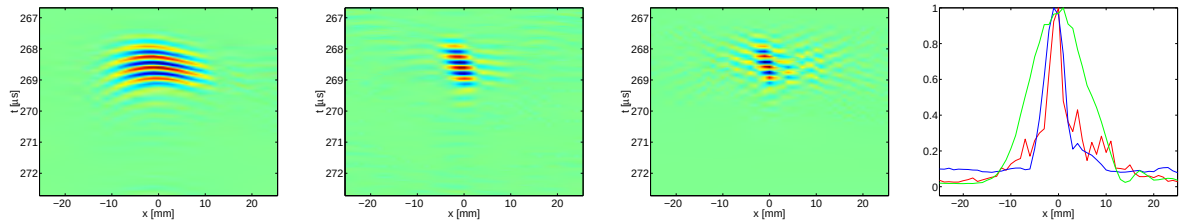

(a) Original B-scan (b) B-scan, SAFT (c) B-scan, MMSE (d) Profiles

Figure 4.48: Target width= $7mm$, target angle= $45°$.

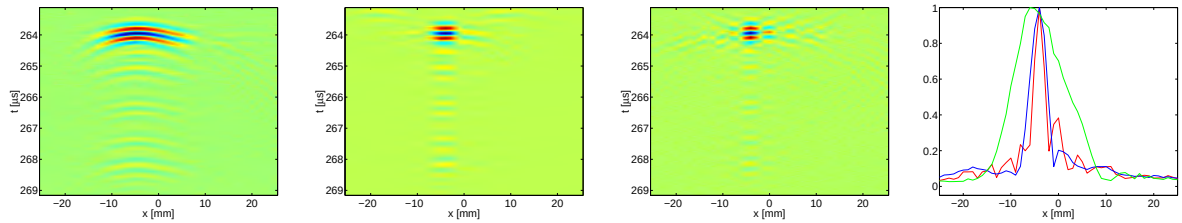

(a) Original B-scan (b) B-scan, SAFT (c) B-scan, MMSE (d) Profiles

Figure 4.49: Target width= $3mm$, target angle= $90°$.

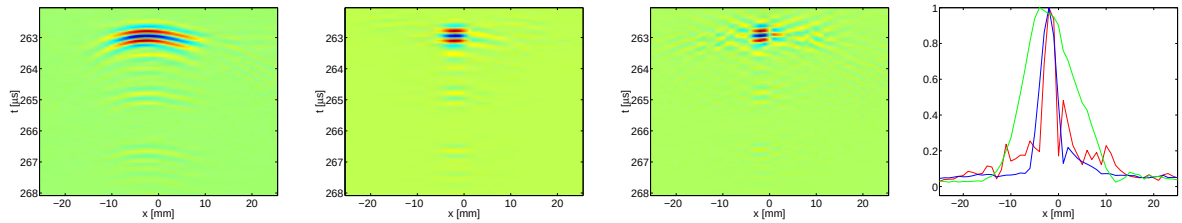

(a) Original B-scan (b) B-scan, SAFT (c) B-scan, MMSE (d) Profiles

Figure 4.50: Target width= $5mm$, target angle= $90°$.

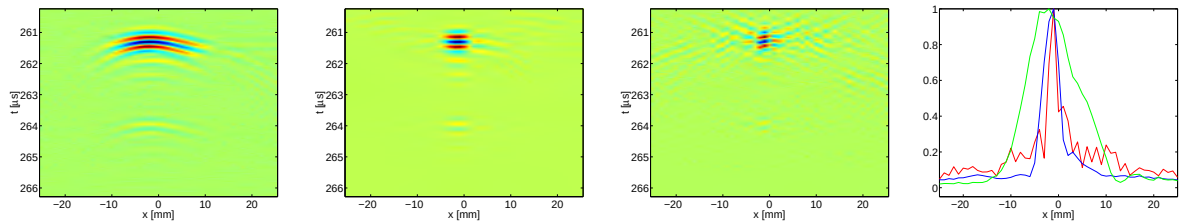

(a) Original B-scan (b) B-scan, SAFT (c) B-scan, MMSE (d) Profiles

Figure 4.51: Target width= $7mm$, target angle= $90°$.

4.A.5 Results: 16 mm transducer

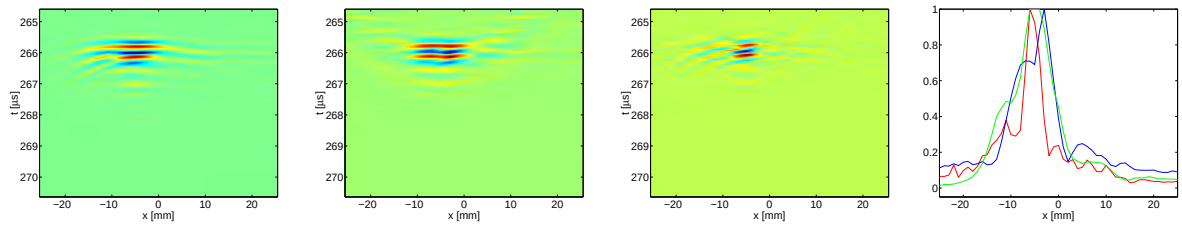

(a) Original B-scan (b) B-scan, SAFT (c) B-scan, MMSE (d) Profiles

Figure 4.52: Target width= $3mm$, target angle= $0°$.

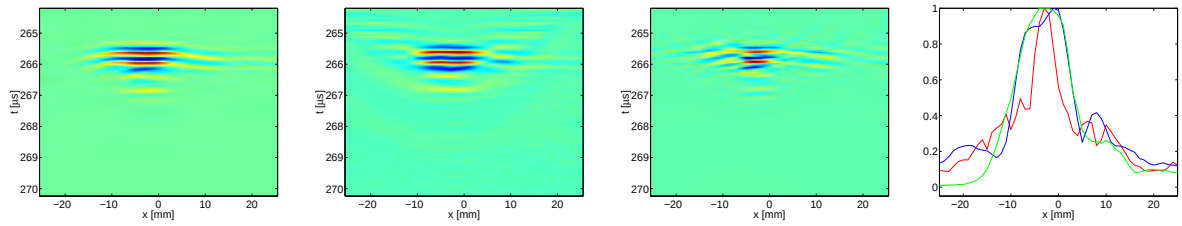

(a) Original B-scan (b) B-scan, SAFT (c) B-scan, MMSE (d) Profiles

Figure 4.53: Target width= $5mm$, target angle= $0°$.

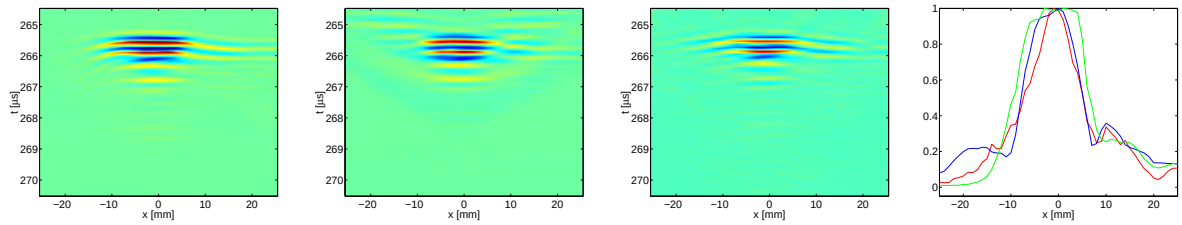

(a) Original B-scan (b) B-scan, SAFT (c) B-scan, MMSE (d) Profiles

Figure 4.54: Target width= $7mm$, target angle= $0°$.

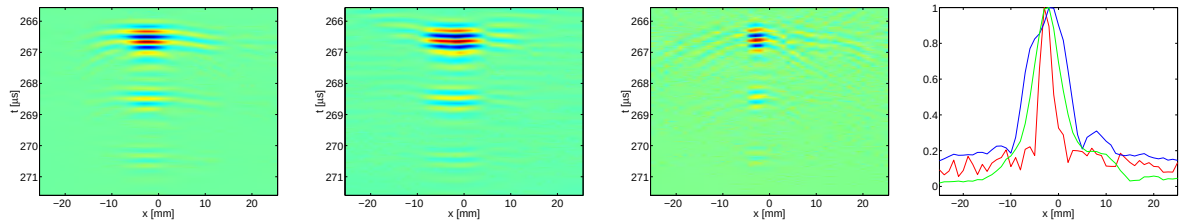

(a) Original B-scan (b) B-scan, SAFT (c) B-scan, MMSE (d) Profiles

Figure 4.55: Target width= $3mm$, target angle= $45°$.

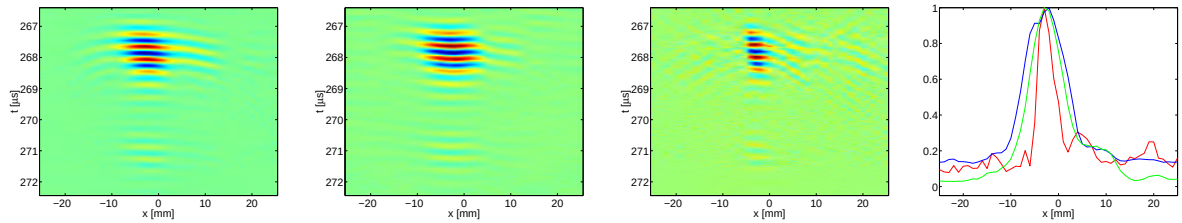

(a) Original B-scan (b) B-scan, SAFT (c) B-scan, MMSE (d) Profiles

Figure 4.56: Target width= $5mm$, target angle= $45°$.

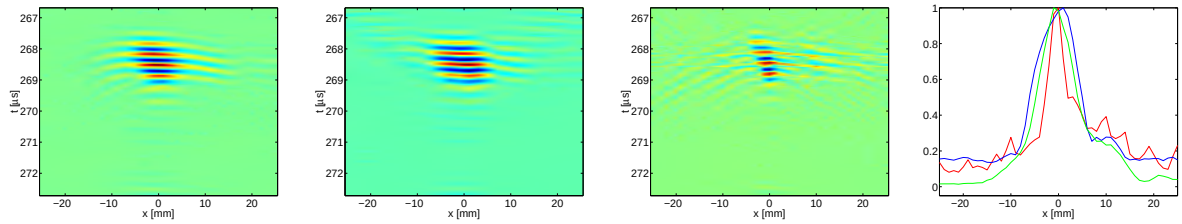

(a) Original B-scan (b) B-scan, SAFT (c) B-scan, MMSE (d) Profiles

Figure 4.57: Target width= $7mm$, target angle= $45°$.

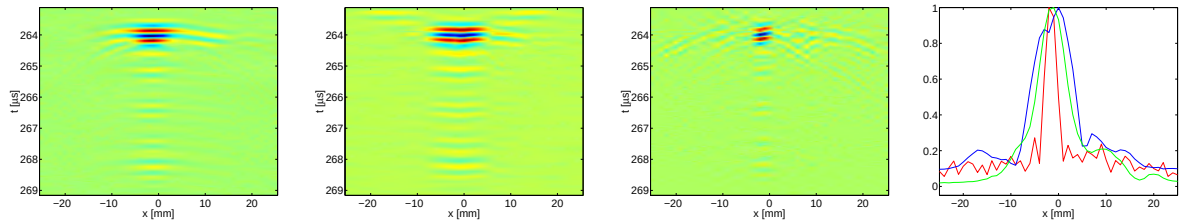

(a) Original B-scan (b) B-scan, SAFT (c) B-scan, MMSE (d) Profiles

Figure 4.58: Target width= $3mm$, target angle= $90°$.

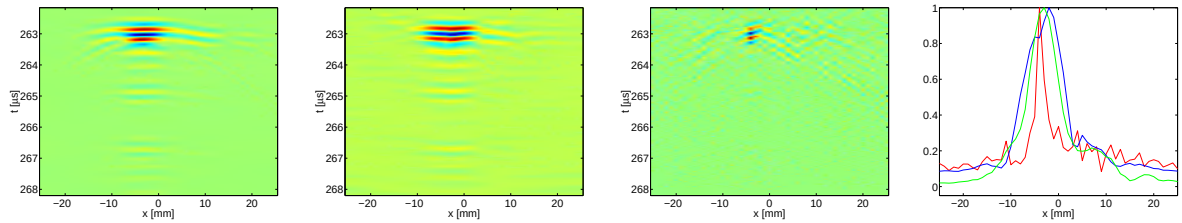

(a) Original B-scan (b) B-scan, SAFT (c) B-scan, MMSE (d) Profiles

Figure 4.59: Target width= $5mm$, target angle= $90°$.

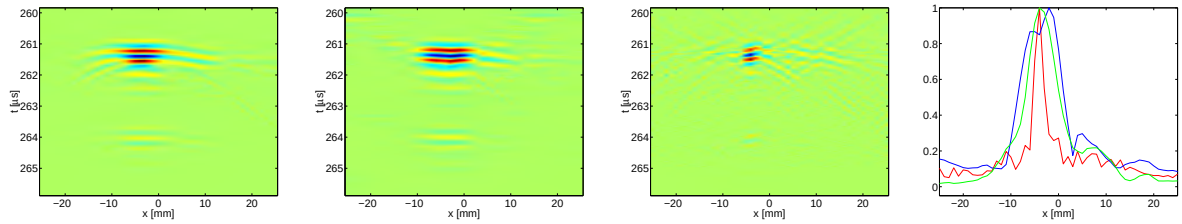

(a) Original B-scan (b) B-scan, SAFT (c) B-scan, MMSE (d) Profiles

Figure 4.60: Target width= $7mm$, target angle= $90°$.

4.A.6 Results: 32 mm transducer

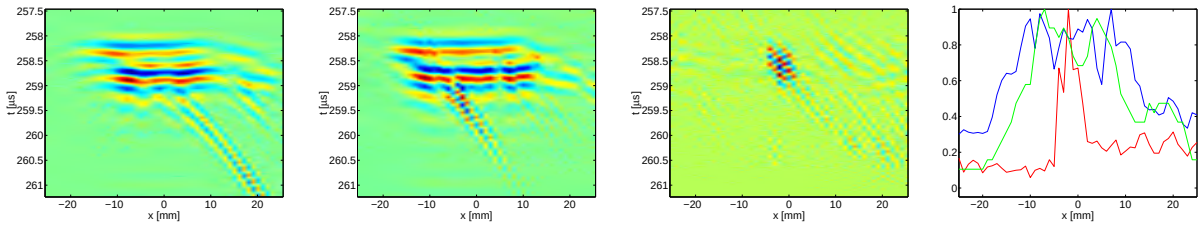

(a) Original B-scan (b) B-scan, SAFT (c) B-scan, MMSE (d) Profiles

Figure 4.61: Target width= $3mm$, target angle= $0°$.

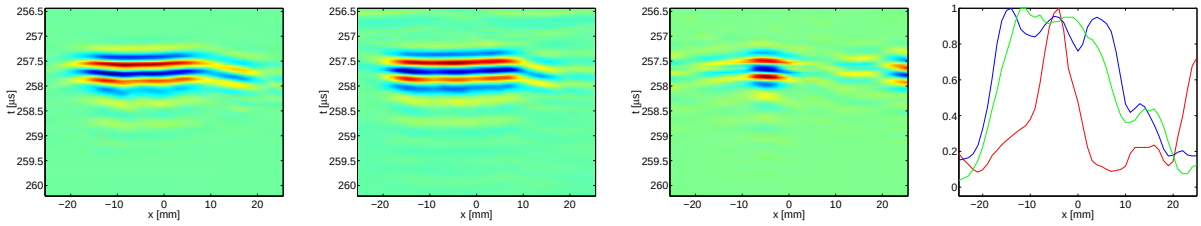

(a) Original B-scan (b) B-scan, SAFT (c) B-scan, MMSE (d) Profiles

Figure 4.62: Target width= $5mm$, target angle= $0°$.

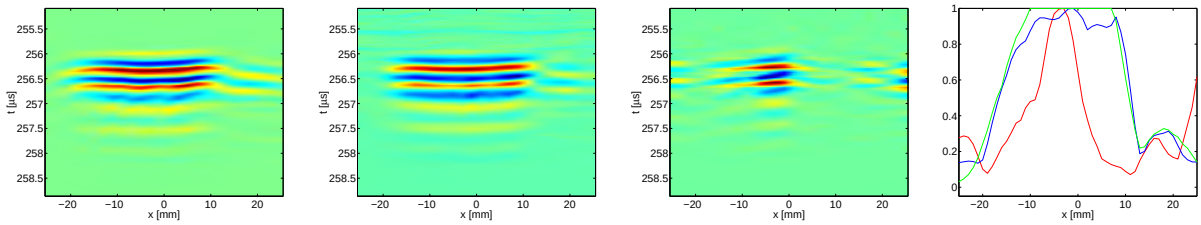

(a) Original B-scan (b) B-scan, SAFT (c) B-scan, MMSE (d) Profiles

Figure 4.63: Target width= $7mm$, target angle= $0°$.

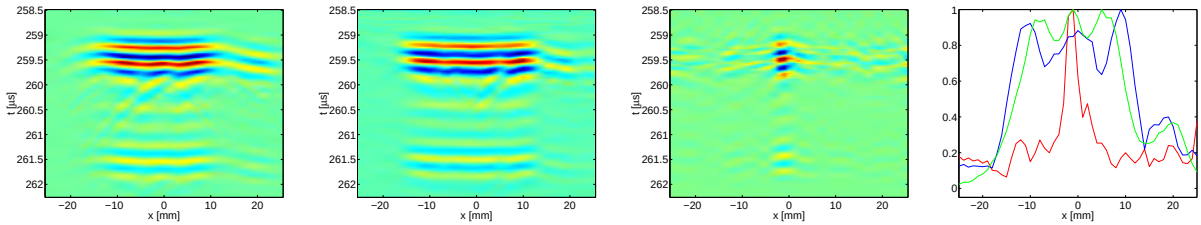

(a) Original B-scan (b) B-scan, SAFT (c) B-scan, MMSE (d) Profiles

Figure 4.64: Target width= $3mm$, target angle= $45°$.

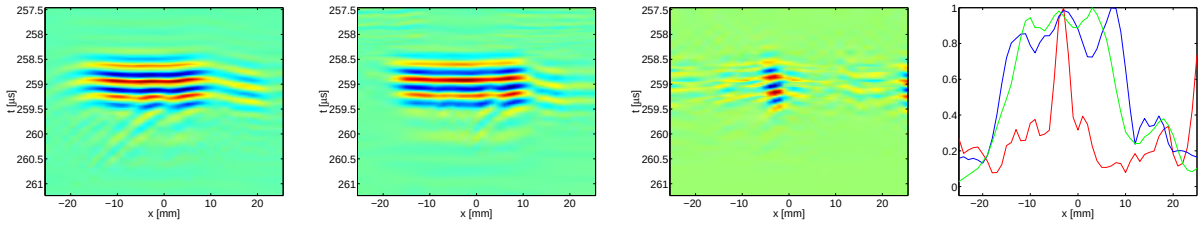

(a) Original B-scan (b) B-scan, SAFT (c) B-scan, MMSE (d) Profiles

Figure 4.65: Target width= $5mm$, target angle= $45°$.

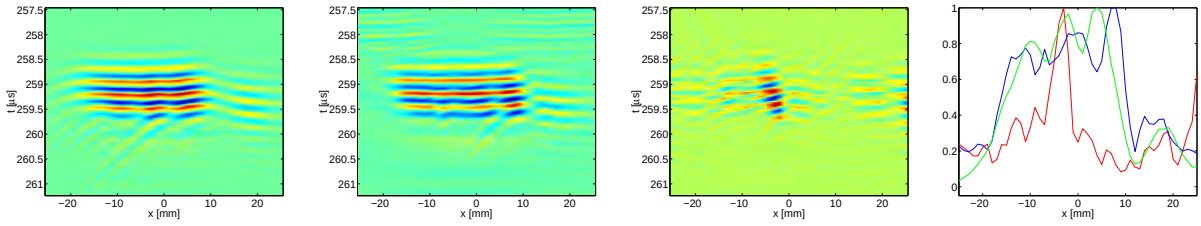

(a) Original B-scan (b) B-scan, SAFT (c) B-scan, MMSE (d) Profiles

Figure 4.66: Target width= $7mm$, target angle= $45°$.

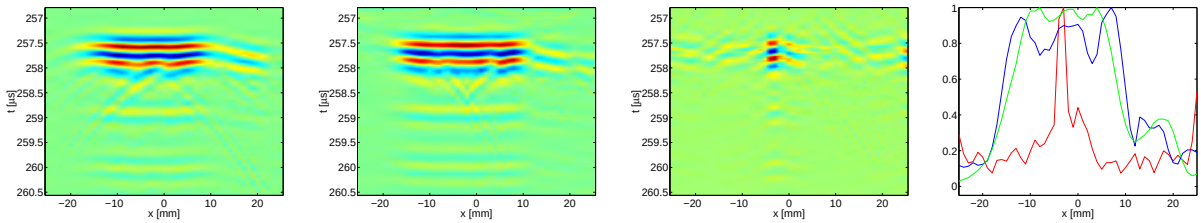

(a) Original B-scan (b) B-scan, SAFT (c) B-scan, MMSE (d) Profiles

Figure 4.67: Target width= $3mm$, target angle= $90°$.

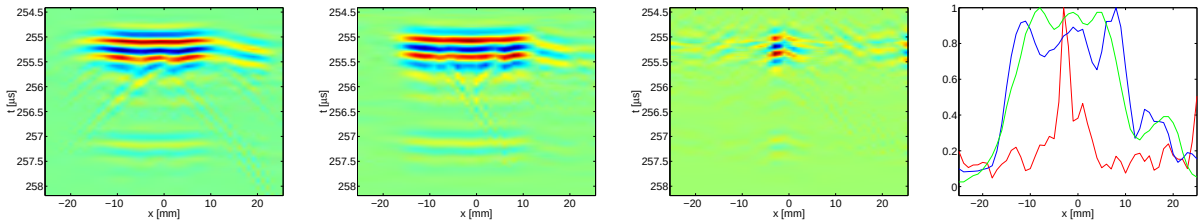

(a) Original B-scan (b) B-scan, SAFT (c) B-scan, MMSE (d) Profiles

Figure 4.68: Target width= $5mm$, target angle= $90°$.

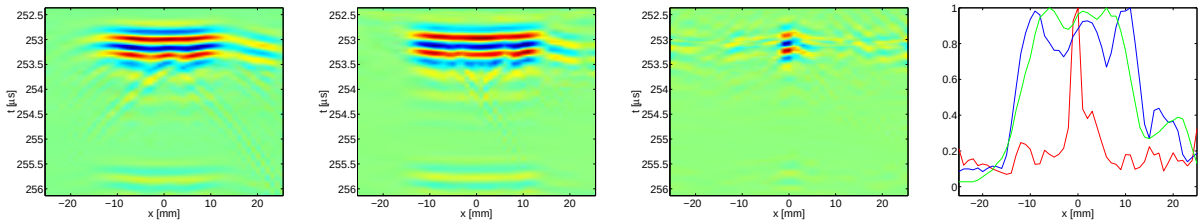

(a) Original B-scan (b) B-scan, SAFT (c) B-scan, MMSE (d) Profiles

Figure 4.69: Target width= $7mm$, target angle= $90°$.

Chapter 5

Ultrasonic Array Imaging

by Fredrik Lingvall

5.1 Introduction

The minimum mean squared error (MMSE) technique used in synthetic aperture imaging (SAI) has recently been shown to yield superior performance in terms of temporal and lateral resolution compared to the classical synthetic aperture focusing technique (SAFT) [1, 2]. In [1, 2] it was also shown that a number of requirements concerning the imaging system must be fulfilled to achieve a satisfactory performance of SAFT.

Since traditional ultrasonic array imaging uses the same delay-and-sum (DAS) methodology as that used in SAFT to perform focusing, the above mentioned conditions also apply to DAS focusing in ultrasonic array imaging. First, the transducer must be small compared to the wavelength, otherwise, the diffraction effects will degrade the processed images [3], and second, the distance between the consecutive elements must be smaller than half wavelength, $\lambda/2$, to avoid grating lobes. However, the transducer must be large enough to generate a sufficient amount of acoustic energy to obtain a satisfactory signal-to-noise ratio (SNR), and thus a trade off between element size and SNR is encountered.

In SAI the same transducer is normally used both in transmit and receive modes and the ytransducer is then scanned to obtain a larger synthetic aperture [4]. A focused image is then obtained by processing the measured B-scan image. In array imaging several elements are normally used simultaneously both in the transmission and reception and the aperture is defined by the number of used elements.

Here, we present an MMSE method that is a generalization of the previously proposed MMSE-SAI method [1, 2] that can be used in a general array imaging case. That is, instead of using the same transmitter and receiver an arbitrary transmit and receive aperture can be used. This allows for treating both focused, unfocused, as well as steered transmit beams. Moreover, as was the case for the previously proposed SAI imaging, the MMSE beamforming method employs a model of finite sized transducer apertures used for imaging as well as their electrical impulse response. The MMSE method is, therefore, expected to be free of the limitations reducing the performance of the DAS technique.

A short introduction to delay-and-sum beamforming is presented first in Section 5.2 and is followed by the presentation of the linear model and the optimal MMSE solution to the linear filtering problem. The description of the experiments using both simulated and measured data can be found in Section 5.3, and finally, the discussion and conclusions are presented in Section 5.4.

5.2 Theory

5.2.1 Delay-and-sum Focusing

The classical phased array beamformer performs focusing in the reception by compensating for different time-of-flights from each array element to the focusing point and then coherent summation of the delayed signals as shown schematically in Figure 5.1. This operation implicitly treats the transducer as a point source for which all SIRs are Dirac functions [1]. The resulting procedure is equivalent to a two-dimensional spatio-temporal matched filter consisting of delta functions in all temporal directions located usually along a hyperbola (for a linear array). If two targets are closely spaced the matched filters for these image points will overlap resulting in a degraded performance (side lobes). Moreover, if the distance between the array elements is larger than $\lambda/2$ grating lobes will be present and there will be more than one point (the focusing point) where the signals are summed in phase.

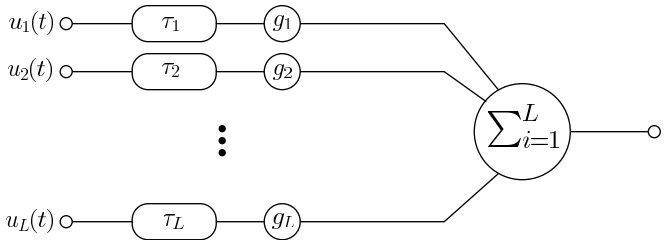

Figure 5.1: Delay-and-sum beamformer.

5.2.2 MMSE Focusing

A Discrete Linear Model for Ultrasonic Imaging

The MMSE receive focusing is, similarly to the previously presented MMSE-SAI method [5, 6], based on a linear model of the imaging system. The difference between the proposed MMSE beamformer and oridinary DAS beamforming is that the transmit and receive apertures do not need be the same in MMSE. The transmit aperture in DAS is, for example, often focused using several transducer elements. To model this, the SIRs for each image point in the region-of-interest (ROI) for the transmit aperture are computed and then convolved with the corresponding SIRs of the receiving elements to get the double-path response.

As for the SAI case [1] the model of the imaging system is based on two assumptions:

- the transducer is regarded as a rigid piston with an infinite baffle, and
- the ultrasonic response from a target is modeled as a sum of contributions from point targets

The output signal from a transducer can then be described as a sum of convolutions of the input signal, $u_{\mathrm{i}}(t)$, the transducer's electrical impulse response, $h_{\mathrm{e}}(t)$, and the spatial impulse response $h^{\mathrm{SIR}}(\mathbf{r}, t)$ to the corresponding point target (with an elementary surface s_{e}) located at position $\mathbf{r}$ [1, 2, 7]

$$u_{\mathrm{o}}(t) = s_{\mathrm{e}} \sum_{\mathbf{r} \in \mathcal{T}} h^{\mathrm{SIR}}(\mathbf{r}, t) * h_{\mathrm{e}}(t) * u_{\mathrm{i}}(t), \tag{5.1}$$

where $\mathcal{T}$ is the set of points where the targets are located and $*$ denotes temporal convolution.

A discrete form of Eq. (5.1) is then obtained by discretizing the SIRs, the electrical impulse response, and the input signal. The L output signals of length K is then put in a $K \times L$ (B-scan) matrix $\mathbf{Y}$ where L is the number of elements in the array.

The discrete convolutions for the lth transducer position are computed, for each image-point in $\mathbf{O}$, and then inserted into the so called *propagation matrix* $\mathbf{P}^{(l)}$ [1]. By vectorizing (in lexicographic order) the object matrix $\mathbf{O}$ to a vector $\mathbf{o}$ the A-scan output for the lth transducer can be expressed

$$\mathbf{y}^{(l)} = \mathbf{P}^{(l)}\mathbf{o},$$

where $\mathbf{y}^{(l)}$ denotes the lth column in $\mathbf{Y}$.

If also the B-scan image $\mathbf{Y}$ is vectorized (and denoted $\mathbf{y}$), a linear model for all L measure-

ments can finally be expressed as

$$\begin{aligned}\mathbf{y} =& \begin{bmatrix} \mathbf{P}^{(0)} \\ \mathbf{P}^{(1)} \\ \\ \vdots \\ \mathbf{P}^{(L-1)} \end{bmatrix} \begin{bmatrix} \mathbf{o}_0 \\ \mathbf{o}_1 \\ \\ \vdots \\ \\ \mathbf{o}_{N-1} \end{bmatrix} + \begin{bmatrix} \mathbf{e}_0 \\ \mathbf{e}_1 \\ \\ \vdots \\ \mathbf{e}_{L-1} \end{bmatrix} \\ =& \mathbf{P}\mathbf{o} + \mathbf{e},\end{aligned} \tag{5.2}$$

where $\mathbf{e}$ is the measurement noise vector.

5.2.3 The MMSE Beamformer

The MMSE beamforming approach consists in designing a linear spatio-temporal filter that minimizes the reconstruction error measured with the mean squared error (MSE) criterion

$$\begin{aligned} J_{\text{MSE}} &= E\{\|\mathbf{o} - \mathbf{K}\mathbf{y}\|^2\} \\ &= \text{tr}\{\mathbf{C}_{oo}\} - 2\text{tr}\{\mathbf{K}\mathbf{P}\mathbf{C}_{oo}\} + \text{tr}\{\mathbf{K}(\mathbf{P}\mathbf{C}_{oo}\mathbf{P}^T + \mathbf{C}_{ee})\mathbf{K}^T\} \end{aligned} \tag{5.3}$$

where $\text{tr}\{\cdot\}$ is the trace operator and $E\{\cdot\}$ is the expectation operator.

The filter matrix, $\mathbf{K}$ which minimizes (5.3), is the minimum mean square error estimator (MMSE) for the linear model (5.2)

$$\begin{aligned} \mathbf{K}_{\text{MMSE}} &= \arg\min_{\mathbf{K}} J_{\text{MSE}} = \mathbf{C}_{oo}\mathbf{P}^T(\mathbf{P}\mathbf{C}_{oo}\mathbf{P}^T + \mathbf{C}_{ee})^{-1} \\ &= (C_{oo}^{-1} + \mathbf{P}^T\mathbf{C}_{ee}^{-1}\mathbf{P})^{-1}\mathbf{P}^T\mathbf{C}_{ee}^{-1}. \end{aligned} \tag{5.4}$$

The MMSE filter (5.4) is the optimal filter for *all* image positions, that is, each row in the filter matrix $\mathbf{K}_{\text{MMSE}}$ holds the optimal filter for the corresponding image point in $\mathbf{O}$. Note that this is a feature that a DAS beamformer does not have. Thus, The MMSE beamformer beamforms all image points from one emission and the array does not need to be refocused or repositioned.[1]

The MMSE filter for one image point can be viewed as shown in Figure 5.2 where the delays

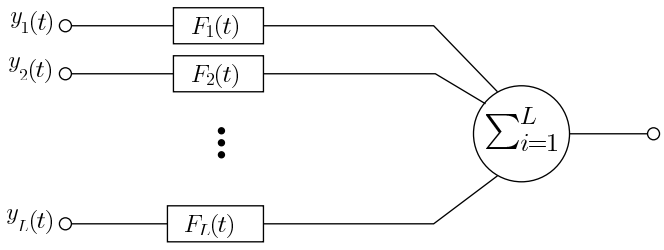

Figure 5.2: MMSE beamformer.

in Figure 5.1 used in DAS focusing now have been replaced with filters. If $\mathbf{O}$ is $M \times N$ then the MMSE filter matrix $\mathbf{K}_{\text{MMSE}}$ contains MN such "filter-and-sum" blocks. Eqs. (5.2) and (5.4) have a similar form the previously proposed MMSE algorithm, with the difference that the SIRs in the propagation matrix have been changed for handling multiple elements.

[1]The whole region-of-interest must (of course) have been insonified with a sufficient amount of acoustic energy, otherwise, the reconstruction performance will be poor.

Note that the DAS and the MMSE approaches are conceptually different since the DAS approach is aimed at maximizing the energy at the focusing point while the MMSE approach minimizes the *over all* reconstruction error. Thus, a DAS processed image will in general have a higher SNR at the focusing point compared to the MMSE. However, an MMSE filter processed image will always have a better (or equal) temporal and lateral resolution than a DAS processed image. In particular, the MMSE beamformer can handle finite sized transducers as well as undersampled arrays.

5.3 Experiments

The MMSE and DAS approaches have been compared using both simulated data generated with the model (5.2) and measured data that was acquired using a phased linear array. All measurements were performed in water using 0.3 mm wire targets. An ALLIN system with 64 element array was used. The array was cylindrically focused at 190 mm in water where each element is 0.9×33 mm. The center frequency of the elements is approximately 3 MHz and the distance between the elements is 1 mm. The wavelength, λ, in water at 3 MHz is about 0.5 mm, hence the width of the array elements and the element spacing is approximately 2λ. Thus, the array is undersampled and grating lobes will therefore appear.

The SIRs needed for the MMSE beamformer were computed using the DREAM method [8] and the electrical impulse response were measured with a wideband hydrophone. In all computations the image points in $\mathbf{O}$ were assumed to be uncorrelated with equal prior variance, $\mathbf{C}_{oo} = \sigma_o \mathbf{I}$, and the measurement noise $\mathbf{e}$ was assumed to be zero mean white Gaussian ($\mathbf{C}_{ee} = \sigma_e \mathbf{I}$). For this case Eq. (5.4) reduces to

$$\begin{aligned} \mathbf{K}_{\text{MMSE}} &= \mathbf{P}^T(\mathbf{P}\mathbf{P}^T + \mu\mathbf{I})^{-1} \\ &= (\mathbf{P}^T\mathbf{P} + \mu\mathbf{I})^{-1}\mathbf{P}^T, \end{aligned} \tag{5.5}$$

where $\mu = \sigma_e/\sigma_o$.

To illustrate the difference between the MMSE and DAS approaches for ultrasonic array imaging a 16 element array was used both in transmit and receive modes. The beam was focused at 50 mm and steered at -20 degrees. This will give a focus point at (z=50 mm, $x \approx$ -18 mm) but also a grating lobe at approximately 10 degrees angle due to the fact that the element spacing is larger than $\lambda/2$. The signals from the receiving elements were then individually recorded and processed with both methods.

Figure 5.3 shows the beampattern for the 16 element steered array in water computed using the DREAM method for a continuous wave with frequency equal the center frequency of the array (3 MHz). Note that pressure amplitude in the grating lobe actually is higher (brighter in the figure) than that in the main lobe. This is due to the fact that the transducer elements is approximately 2λ and have, therefore, a non negligible beam directivity (see Figure 5.4). However, the amplitude in the main beam will increase compared to the grating lobe if a wideband excitation is used. For the wideband excitation (pulse) the signals from different elements will be summed coherently at the focal point while they arrive with an individual shift of approximately λ in the grating lobe [3]. Since the excitation pulse usually is longer than λ parts of the signals from each element will be summed coherently but the amplitude will be lower compared to harmonic excitation.[2]

Figure 5.5 shows maximum amplitudes of DAS and MMSE beamformed wideband data (at x = -18 mm) as a function of target position both for simulated and measured data. White Gaussian noise was added to the simulated data to show how the value of μ influences the

[2]This also results in a longer response from a target in the grating lobe compared to a target in the main lobe.

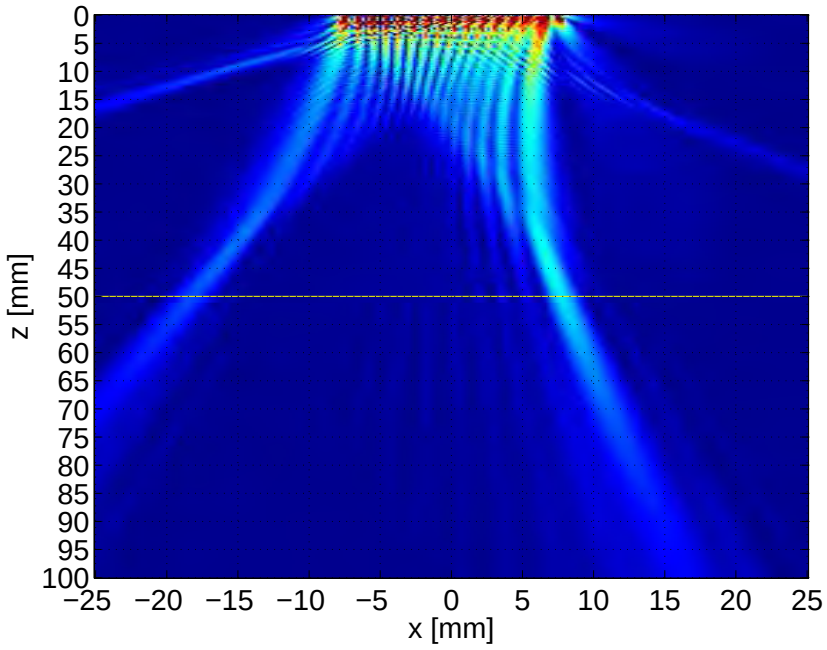

Figure 5.3: Beampattern of a 16 element array focused at 50mm and steered 20 degrees at f=3 MHz for a sound speed of 1482 m/s.

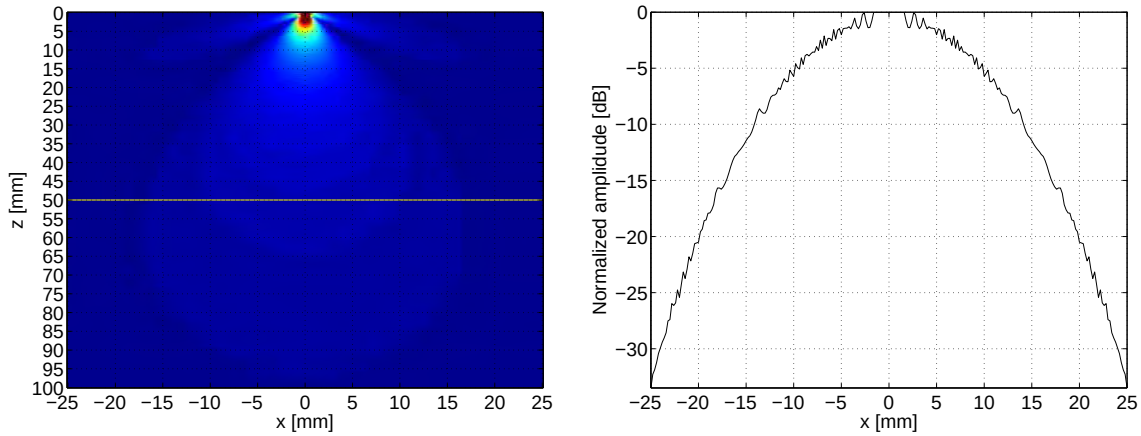

(a) Beampattern.

(b) Normalized amplitude at $z = 50$ mm.

Figure 5.4: Beampattern of a 0.9 mm transducer (one element) at f=3 MHz for a sound speed of 1482 m/s.

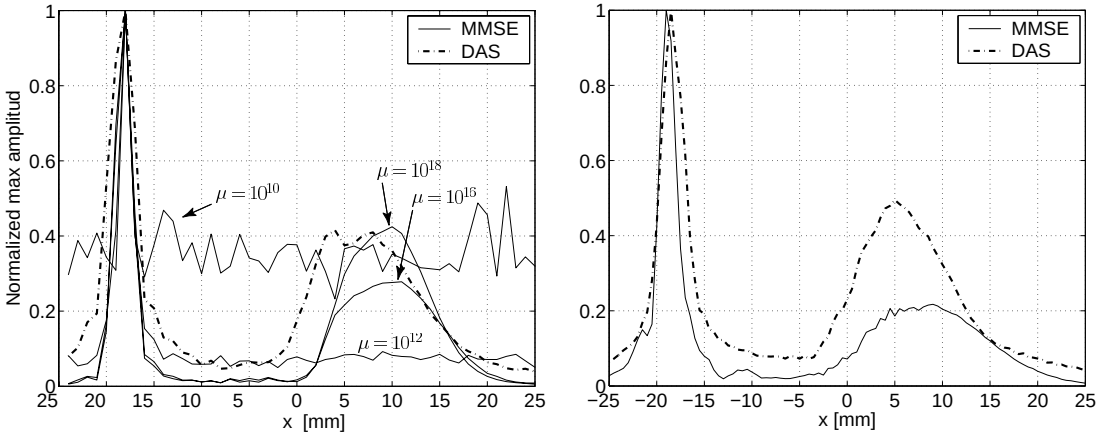

(a) Simulated data (with added white Gaussian noise).

(b) Measured data (0.3 mm wire target).

Figure 5.5: Maximum amplitude as a function of horizontal (point) target position for a 16 element linear array focused at 50 mm and steered at an angle of -20 degrees. Dash-dotted: DAS beamforming and solid: MMSE beamforming.

performance (Figure 5.5(a)). Four values of μ were used, 10^{10}, 10^{12}, 10^{16}, and 10^{18}. The lowest value, $\mu = 10^{10}$, results in the highest resolution but also strong noise amplification, $\mu = 10^{12}$ yields both good lateral resolution and noise amplification similar to DAS. The grating lobe has also been entirely suppressed for $\mu = 10^{12}$. If μ is increased further the MMSE method starts to show a higher amplitude for the target positions within the grating lobe. In fact, when $\mu\mathbf{I} \gg \mathbf{P}\mathbf{P}^T$ the MMSE method acts as a matched filter with a performance similar to the DAS beamformer. The lateral resolution was better for MMSE for all tested values of μ and the amplitude when the target is within the grating lobe is lower for MMSE compared to DAS when $\mu \lesssim 10^{17}$.[3]

It is important to note that it is not possible to distinguish whether the target is within the main or grating lobe when using the DAS beamformer. The MMSE beamformer on the other hand has not this limitation provided that the SNR is high enough. Another advantage of the MMSE beamformer is that, similar to a parallel DAS beamformer [9], the ability to reconstruct the whole ROI based on a single measurement. Thus, the target position can, therefore, be determined regardless if the target is in the main lobe or in the grating lobe from a single measurement using the MMSE beamformer.

The performance of the MMSE reconstructions will depend on the transmitted beam pattern. Of course, only the insonified targets can be reconstructed. This is illustrated in Figure 5.6 where reconstructions from three target positions (one emission per target position) are presented. As can be seen in Figure 5.6(a) and (c) the reconstructions of the point target have a high temporal and lateral resolution, both when the target is in the main and the grating lobe. The reconstruction when the target is located between the main and grating lobe (Figure 5.6(b)) is, however poor. This is due to the low acoustic energy in this area. Thus, the MMSE algorithm is able to use both the main and the grating lobe for beamforming, and and if, for example, a wider beam was used in our example even larger area could be processed with good results. It should be emphasized that similar images cannot be obtained using an ordinary DAS beamformer since the DAS beamformer cannot discriminate between grating and main lobe.

[3]All values of μ given above are specific for the considered case (not normalized).

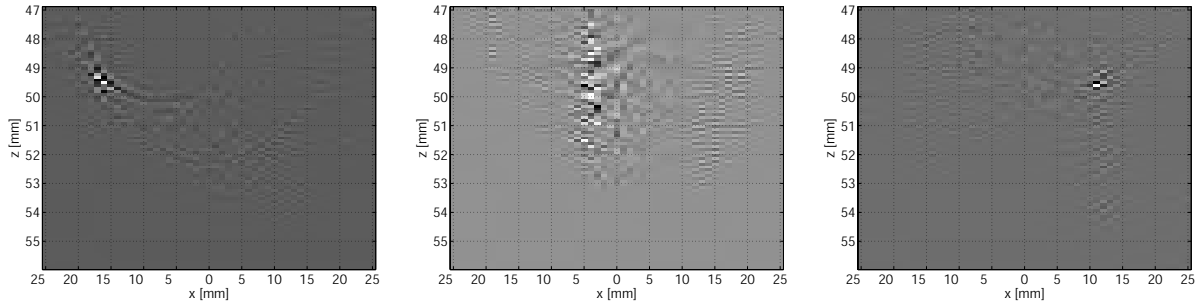

(a) Target position in the main lobe.

(b) Target position between main and grating lobe.

(c) Target position in the grating lobe.

Figure 5.6: Reconstructions from single emissions using a 16 element linear array focused at 50 mm and steered at an angle of -20 degrees.

5.4 Discussion

A new, model based MMSE receive beamformer has been presented and compared to the traditional DAS beamformer using both simulated and measured data. It was shown that both the temporal and lateral resolution was superior for the proposed MMSE beamformer compared to the DAS beamformer.

Moreover, the MMSE beamformer, due to its parallel structure has two other features that the DAS beamformer does not possess. Firstly, if the transmit aperture is focused and the measurement noise is reasonable low, one does not need to take care of the grating lobes. The array can be simply viewed as a transducer that emits energy in two directions and both of them can be used for the reconstruction. Secondly, if the SNR is satisfactory one does not need to send several pulses refocused at different positions to obtain the reconstruction of the whole region-of-interest, only one pulse can be sent instead and the reconstruction of the entire image can be obtained. Thus, is it possible to obtain a very high frame rate given that the computational hardware is sufficiently fast.

To conclude, the MMSE method applied to focusing of ultrasonic array in reception enables the use of undersampled arrays that have an element size and/or a distance between elements, larger than $\lambda/2$. The method also allows for a very high frame rate since the reconstruction of the entire image can be performed from one emission.

Bibliography

[1] F. Lingvall, T. Olofsson, and T. Stepinski. Synthetic aperture imaging using sources with finite aperture: Deconvolution of the spatial impulse response. *J. Acoust. Soc. Am.*, 114(1):225–234, July 2003.

[2] T. Stepinski, F. Lingvall, and P. Wu. Inspection of copper canisters for spent nuclear fuel by means of ultrasound. Technical report, SKB, 2002.

[3] G.S. Kino. *Acoustic Waves: Devices, Imaging and Analog Signal Processing*, volume 6 of *Prentice-Hall Signal Processing Series*. Prentice-Hall, 1987.

[4] J.A. Seydel. *Ultrasonic Synthetic-aperture Focusing Techniques in NDT*. Research Techniques for Nondestructive Testing. Academic Press, 1982.

[5] T. Stepinski, F. Lingvall, and P. Wu. Inspection of copper canisters for spent nuclear fuel by means of ultrasound — ultrasonic imaging of eb weld, theory of harmonic imaging of welds, and nde of cast iron. Technical Report TR-01-36, SKB, 2001.

[6] P. Wu, F. Lingvall, and T. Stepinski. Inspection of copper canisters for spent nuclear fuel by means of ultrasound — electron beam evaluation, harmonic imaging, materials characterization and ultrasonic modeling. Technical Report TR-00-23, SKB, 2000.

[7] A. Lhémery. Impulse-response method to predict echo-responses from targets of complex geometry. Part I: Theory. *J. Acoust. Soc. Am.*, pages 2799–2807, November 1991.

[8] B. Piwakowski and K. Sbai. A new approach to calculate the field radiated from arbitrarily structured transducer arrays. *IEEE Trans. on Ultrasonics, Ferroelectrics, and Frequency Control*, pages 422–440, 1999.

[9] D.P. Shattuck, M.D. Weinshenker, S.W. Smith, and O.T. von Ramm. Explososcan: a parallel processing technique for high speed ultrasound imaging with linear phased arrays. *J. Acoust. Soc. Am.*, 75(4):1273–1282, April 1984.

ISSN 1404-0344

CM Digitaltryck AB, Bromma, 2004